Charles University in Prague
Faculty of Mathematics and Physics
Institute of Physics of the Charles University

PhD Thesis

Optical excitations of metallic surfaces

Jiří Franta

Supervisor: Doc. Mgr. Miroslav Nývlt, Dr.
Advisors: Prof. Dr. Jürgen Kirschner
Prof. Ing. Štefan Višňovský, DrSc.

Study program: Physics
Study branch: F6 : Quantum optics and optoelectronics

Praha 2005

I declare that my PhD thesis has been elaborated personally and that I have used only the literature listed. I agree with loaning out my work.

Praha, 17. 10. 2005

To my parents

Acknowledgements

This thesis is a result of my PhD study proceeding from 2001 to 2005 at the Faculty of Mathematics and Physics of the Charles University in Prague. However, most of the experimental work was done during my stay (February 2002 – June 2004) in the Max Planck Institute of Microstructure Physics in Halle, Germany.

First, I would like to thank Miroslav Nývlt, my supervisor, for his continuous support during my studies. I am very grateful to him for introducing me into fields of magnetooptics, femtosecond lasers, photoemission and Second Harmonic Generation. His enthusiasm allowed us to achieve and explain lots of interesting experimental results.

My great thanks are addressed also to Francesco Bisio. His competence in fields of Second Harmonic Generation and photoemission was invaluable. Lots of stimulating scientific and non-scientific discussions we had together are unforgettable.

I also wish to thank to Prof. Hrvoje Petek for introducing me into the field of the characterization of ultrashort laser pulses. For many interesting discussions about the Second Harmonic Generation technique, I am very grateful to Prof. Oleg Aktsipetrov.

I am deeply grateful to Prof. Jürgen Kirschner for the opportunity of working at the Max Planck Institute of Microstructure Physics. Without his support, the experimental part of the work couldn't be done at all. Being a part of the exceptional scientific environment in the institute was an invaluable experience.

Also other colleagues from the Max Planck Institute of Microstructure Physics, namely Chunlei Gao and Jonas Will, were helping me a lot. I would like to thank them for their experimental assistance and friendly atmosphere in the laboratory.

The help and support from the people from the Prague laboratory should not be omitted. My greatest thanks are addressed to Prof. Štefan Višňovský for his continuous support of my work. The thanks should be transmitted also to the other colleagues from the laboratory. Martin Veis, Roman Antoš, Vratislav Kolinský, Jaroslav Hamrle and Jana Hamrlová were always open to scientific and non-scientific discussions and thus forming a very stimulating atmosphere in the laboratory.

Last but not least, I would like to thank to my parents, my sister and my Michalka for their continuous support during my studies and for their love.

Contents

Introduction

Investigations of properties of solid materials by optical methods are now considered as a classical part of the experimental physics. The use of an optical beam as a probe has some significant advantages with respect to other methods. In most cases, it is absolutely non-destructive. Its penetration depth ($\sim$10 nm in metals at visible radiation wavelengths) is allowing to probe bulk properties. But in particular cases the surface properties can be studied as well.

Magnetic materials are very interesting from an industrial application point of view. In many rewritable data storage devices, as hard disks, the information bit is stored in a form of a magnetization direction of a piece of material. The challenge is to make the bit as small as possible and thus increase the density of the stored information. The historical overview of the increasing capacity of hard drives is illustrated in Fig. 1. The important milestones of the data-recording industry are indicated there. Above all, the application of magneto-resistive read heads at the beginning of nineties was promoting very fast growth of the storage capacity. Recently, the storage of the information in elements magnetized perpendicularly to the media surface (so called *perpendicular recording*) is promising further increase of the hard drives capacity [1]. However, the magnetization-based electronic elements are recently spreading from the data-recording applications to other branches of the electronics industry. The spin-polarized field effect transistor is one example of such electronic elements. Incorporating the spin degree of freedom into the electronic devices is often called *spintronics* or *magnetoelectronics* [2–4].

For further progress in the industrial applications and in the basic research as well, it is necessary to have the time-resolved information about the electronic processes taking part in the respective materials. Optical methods are proved to be very useful in this case. They can probe not only the dynamics of the magnetization reversal process occurring at $\sim\mu$s time scale [5, 6], but the femtosecond range can be achieved as well. This is possible, as the resolution of the optical methods is related to the parameters of an optical pulse (i.e. its wavelength and width) used as a probe. The processes accessible

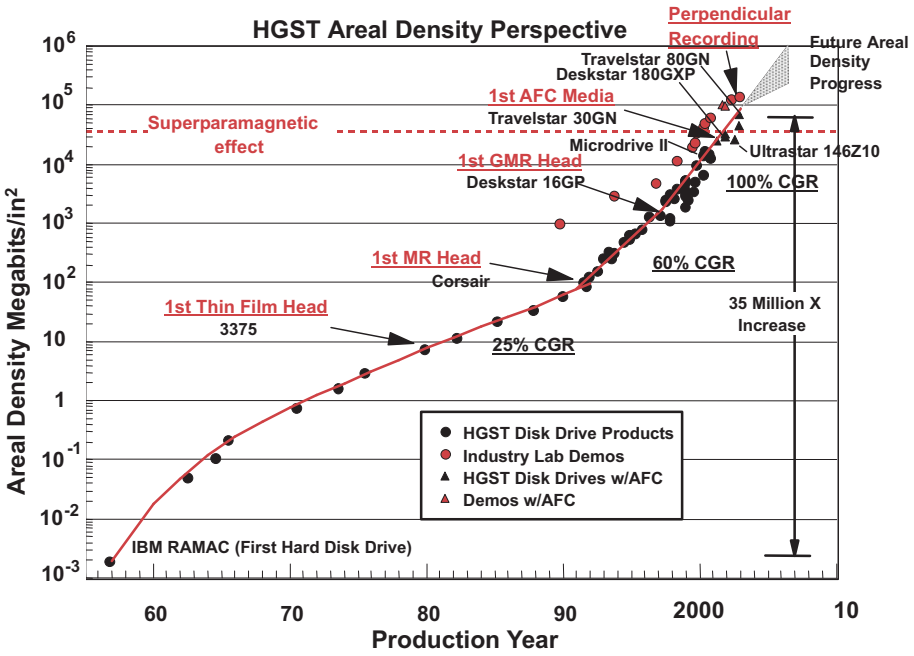

Figure 1: The capacity of hard drives as a function of time, published by the Hitachi company [7].

by recent pulsed laser technology are indicated in Fig. 2. It should be noted that also a spin-resolution can be achieved very conveniently by optical methods, because the excitation by circularly polarized light is spin-selective.

In this thesis, an experimental setup which employs the ultrashort light pulses for the sample excitation will be used. Two principal experimental methods will be coupled to this excitation source. One of them is the Surface Second Harmonic Generation method while the other one is the Two-Photon Photoemission technique. As the photoemission and the second-harmonic generation parts of the apparatus are partly independent, different chapters of the thesis will be dedicated to these individual parts of the experiment to demonstrate their performance. Later, the cooperation of these two parts will be needed to achieve the time-resolution on the femtosecond scale.

The thesis is organized as follows: In Chapter 1, the two-photon photoemission experimental method will be explained from the theoretical point of view. Also the experimental setup will be described and possible objects of studies will be summarized.

In Chapter 2, the experimental higher-order photoemission results on Cu(001) surfaces will be described. It will be shown that even more than two-photon processes are observable.

Chapter 3 will be summarizing fundamentals of the Magnetization-Induced Surface

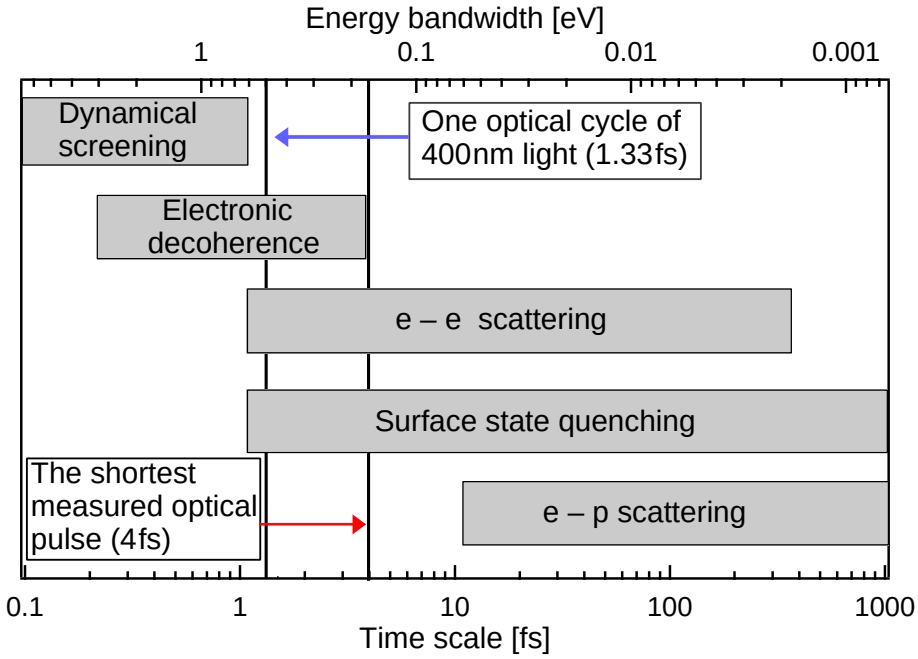

Figure 2: The time scales for various dynamical processes at metal surfaces after [8]. Vertical lines indicate benchmark time scales for state-of-art laser measurements.

Second Harmonic Generation technique. The experimental setup will be described and possible applications in experimental configurations with various symmetries will be discussed.

Experimental results obtained by the Magnetization-Induced Surface Second Harmonic Generation technique will be presented in Chapter 4. The object of the study will be the p(1×1)O/Fe/MgO(001) structure which is a model system for the adsorbate–metal interaction studies. Studies of surface magnetic properties during epitaxial layer-by-layer growth of the Fe layer with surfactant oxygen will be described.

In time-resolved studies, it is necessary to measure at the same time the photoemission and the second-harmonic generation signals. The theoretical background for these studies will be given in Chapter 5. A basic model for interpreting the experimental data will be introduced there.

A necessary precondition for successful interpretation of the time-resolved experiments is the femtosecond pulse shape determination. This issue will be addressed in Chapter 6. It will be checked whether the obtained accuracy is sufficient for correct analysis of the data from a time-resolved experiment.

Chapter 1

Two-photon photoemission

In this chapter, the two-photon photoemission phenomenon will be discussed. The photoemission technique was one of the triggers of the quantum mechanics development in the beginning of the 20th century. This experimental technique is used in a variety of its modifications for studies of the electronic structure of numerous materials for more than one century. In intense exciting fields, higher order effects can be detected, the two-photon photoemission for instance. However, practical observations of two-photon photoemission process are possible only in the case when the one-photon photoemission signal is not present. This can be achieved when the energy of exciting photons is insufficient for one-photon excitation. The two-photon photoemission brings new possibilities into the photoemission studies. The unoccupied states and the hot electron dynamics are the major issues which are conveniently studied by the photoemission caused by excitation by two photons. In this chapter, the theoretical background of two-photon photoemission will be summarized and possible experimental approaches will be discussed.

1.1 Principles of two-photon photoemission

In this section, we will first summarize the quantum mechanical principles of the one-photon photoemission. The complexity added by the two-photon excitation will be discussed afterwards.

The phenomenon of the photoemission was discovered by Hertz already in 1887. The following experiments allowed Einstein to explain this effect and to discover the quantum nature of light.

1.1.1 Energy conservation

The mechanism of the photoemission process is schematically depicted in Fig. 1.1. The minimum energy which has to be supplied to an electron coming from the Fermi level E_F to excite it to the vacuum state is called *a work function*. In Fig. 1.1, it is indicated as Φ. An electron from the states below E_F needs additional energy corresponding to its binding energy E_B to escape from the solid. Any other excessive energy supplied to the electron becomes its kinetic energy E_{kin}. As the energy is supplied to the electron by one photon, one can express the energy conservation law as

$$E_{\mathrm{kin}} + E_B + \Phi = \hbar\omega \ . \tag{1.1}$$

The momentum of the detected electron of mass m_e can be directly obtained as

$$p = \sqrt{2m_e E_{\mathrm{kin}}} \ , \tag{1.2}$$

the direction of the $\boldsymbol{p}$ (and $\boldsymbol{k}$) vector is obtained from the geometrical configuration of the experiment. The basic and the most attractive feature of the photoemission process is that the energy distribution of the emitted electrons (photoelectron spectrum) is corresponding to the statistical distribution of electron energies in the solid.

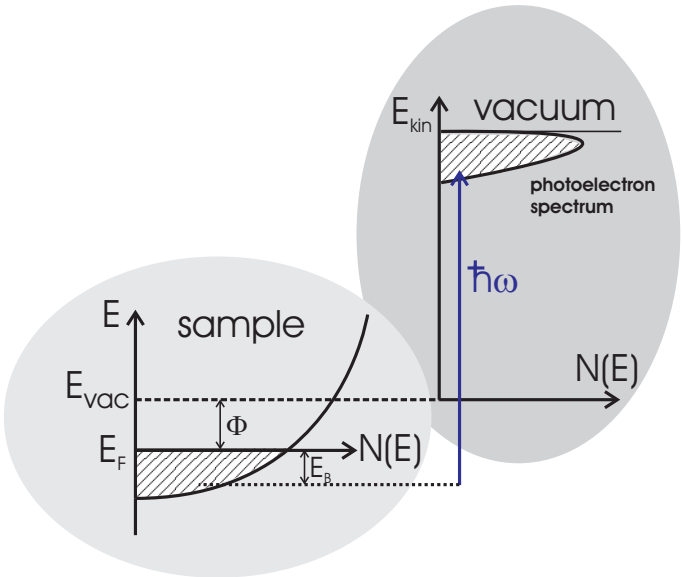

Figure 1.1: The energetic schematic of the photoemission process. In the solid are the binding energies referenced to the Fermi level E_F, in the vacuum serves E_{vac} as a reference.

1.1.2 Three step model

For the interpretation of a photoemission experiment, one can use quite successfully a so-called *three-step model* [9]. In this model, the photoemission process is separated into three independent steps, as shown in Fig. 1.2. In the first step, an absorbed photon excites an electron. This occurs over the whole penetration depth of the radiation used for the excitation. In the second step, the electrons travel though the material towards the surface. Secondary electrons are produced due to nonelastic scattering. Only the electrons within the escape depth can reach the surface with energy higher than Φ. In the third step, the electrons escape through the surface into the vacuum where they can be detected.

The separation of the photoemission process into three steps is in principle artificial and the whole process should be in fact treated as one step. The so called *one-step model* can handle this. In this model, the electron is excited directly form the ground state of a Bloch wave in the solid into the final state which is a wave propagating freely in vacuum

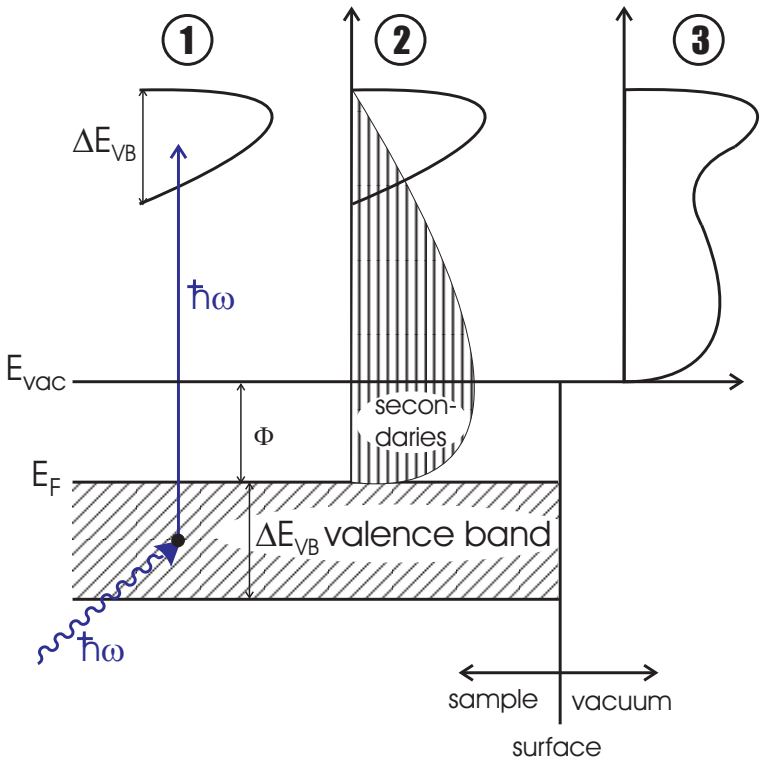

Figure 1.2: The 3 step model: 1) photoexcitation of electrons, 2) transport of the excited electrons to the surface, secondary electrons are produced, 3) penetration through the surface and escape into the vacuum.

but decaying rapidly into the solid. However, in most cases the much simpler three-step model is giving results very similar to those of the one-step model [9].

A very important aspect of the photoemission experiment is the small escape depth of the photoelectrons which is of the order of a few lattice constants. The probed electronic structure is therefore influenced by the surface. This brings difficulties when studying the bulk electron properties. On the other hand, the photoemission method is very suitable for studies of the surface effects.

1.1.3 Two-photon photoemission (2PP)

The conventional photoemission process involves one photon only. With the invention of the laser in sixties [10] the field of multiphoton excitations of the bound electrons started its development. The first observation of a two-photon photoemission (2PP) yield from a metal sample was done in 1964 by Teich et al. [11].

The two-photon photoemission process is schematically depicted in Fig. 1.3. The kinetic energy of the detected electron is related to twice the energy of exciting photons by modified Eq. 1.1

$$E_{\mathrm{kin}} + E_B + \Phi = 2\hbar\omega \ . \tag{1.3}$$

The effect is observed when the energy of one photon is not sufficient to excite the electron to a vacuum state. In other case, the one photon photoemission would be much more intense than 2PP which would make the observation of 2PP impossible.

The two-photon photoemission can be distinguished from the one-photon photoemission by its dependence on the exciting beam intensity. In contrary to the one-photon

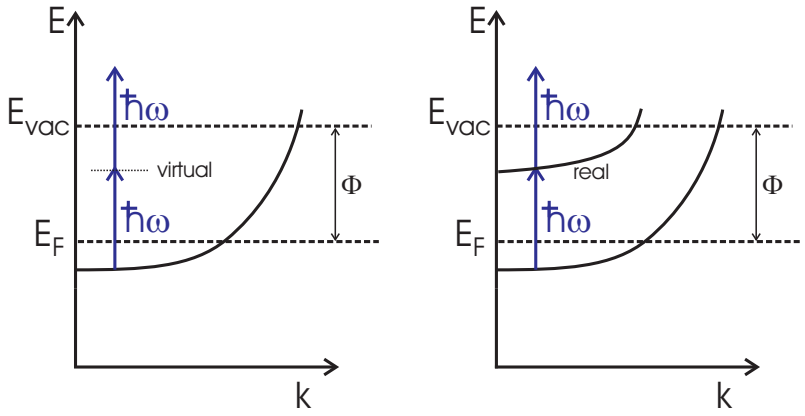

Figure 1.3: The schematic of the two photon photoemission process. It can involve either virtual intermediate states only (the left panel) or a real unoccupied state (the right panel).

process the two-photon photoemission intensity (i.e. the number of detected photoelectrons) is proportional to the square of the intensity of incoming light.

Another interesting aspect of 2PP is that the unoccupied bands above E_F can play a role in the two-photon photoemission process. In Fig. 1.3, it is seen that the two-photon photoemission can involve either virtual intermediate states (a truly two-photon process) or real unoccupied intermediate states (a cascade of two subsequent one-photon processes). The fact that the excitation pathway can involve a real intermediate state allows to study properties of unoccupied electronic states above the Fermi level by 2PP. This will be discussed in detail in Sec. 1.4.

In a case of the real intermediate state, the two photons involved in the excitation process do not have to arrive necessarily at the same time. A non-zero lifetime of the intermediate state allows the second step of the excitation even when the second photon comes with a non-zero delay after the first one. Changing the delay between the two photons allows to perform experimental studies of lifetimes of the intermediate states. This will be discussed in more detail in Chapter 5.

1.2 Experimental approaches

In this section, the experimental approaches used in photoemission experiments will be discussed. The focus will be put on the two-photon photoemission and on the other methods suitable for studies of unoccupied electronic states.

Photoemission is a classical experimental technique and its principles are the same for more than 100 years. The basic setup is sketched in Fig. 1.4 [9]. The photons are impinging on the sample and the photoelectrons with kinetic energy selected by an energy analyzer are counted by a detector. Important parameters allowing the reconstruction of the sample electronic structure are the kinetic energy of the detected electrons E_{kin} and

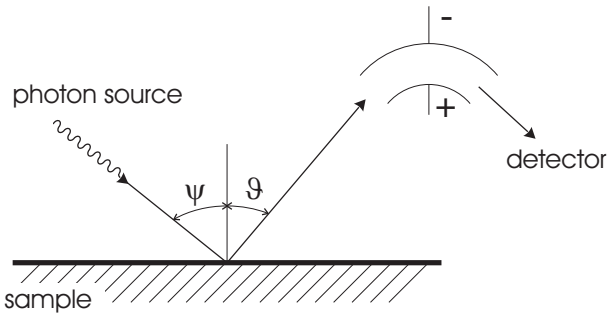

Figure 1.4: Schematic of the experimental setup used for photoemission experiments.

the angles of excitation ψ and emission ϑ related to the geometry of the experimental arrangement.

As the electron escape depth from a solid is of the order of a few atomic planes, the surface of the sample has to be atomically clean. Therefore, it is necessary to perform the photoemission experiments under Ultra High Vacuum (UHV) conditions.

As a photon source it is possible to use a gas discharge lamp, an X-ray tube, a laser or synchrotron source. Synchrotron radiation is recently very popular because its photon energy is easily tunable over a broad spectral range and it has a high intensity. However, the laser sources offer coherent radiation suitable for studies of the optically induced coherence between levels in the solid (see Sec. 5.3). In addition, pulsed lasers can offer a very high peak photon fluxes allowing to perform effectively multiphoton excitations.

For detection of the photoelectrons, the electrostatic analyzers are usually used. The effect of a change on a trajectory of an electron in the electrostatic field is employed. In principle, also magnetic analyzers could be used. Their application is bringing many difficulties, so that they are nowadays used only rarely. According to the geometry of the electrodes of the electrostatic analyzers, one distinguishes between Cylindrical Deflection Analyzer, Spherical Deflection Analyzer, Plane Mirror Analyzer, Cylindrical Mirror Analyzer etc.

Inverse processes to the photoemission experiments are employed in the *inverse photoemission* method. In this process, an impinging electron is captured by the sample. As the process is just an inverse to the photoemission effect, one photon is emitted. The energy of the photon is corresponding to the energy level to which the electron was captured. The energy distribution of the unoccupied electronic states in the solid can be determined by analyzing spectral properties of the emitted light. The inverse photoemission method was applied to studies of unoccupied states above E_F which are also a subject of our interest [12, 13].

For the two-photon photoemission experiment, a pulsed laser is used as a source of the exciting photons. The present advances in the femtosecond pulsed laser technology allow achieving very high peak powers ($\sim 10\,\mathrm{GW/cm^2}$ or even more). As the efficiency of the two-photon process is proportional to the square of the power density, a high attention has to be paid to the optimization of the pulse length and the overall output power of the laser system.

1.3 Experimental setup for two-photon photoemission

In this section, we will describe the experimental setup used for the two-photon photoemission experiments discussed in this work. The schematic of the setup is displayed in Fig. 1.5. It has two principal parts: a femtosecond laser and a UHV photoemission chamber. It is easily possible to modify the setup to perform time-resolved experiments. These modifications will be described later in Section 5.2.

The details of the experimental apparatus will be described in following subsections 1.3.1 – 1.3.4. Here we only summarize with use of Fig. 1.5 the basics of the cooperation of individual parts of the setup: The femtosecond laser pulses are generated in a home-built titanium-sapphire (Ti:S) oscillator. The central photon energy (1.55 eV) is not sufficient to perform two-photon photoemission experiment on most metals. Therefore, the beam is passing through a frequency-doubling stage where photons with sufficient energy (3.1 eV) are produced. The dispersion of the pulses has to be compensated afterwards to achieve the best performance (shortest pulse) at the sample location. The polarization of the incident beam is set before it is entering the UHV chamber. After

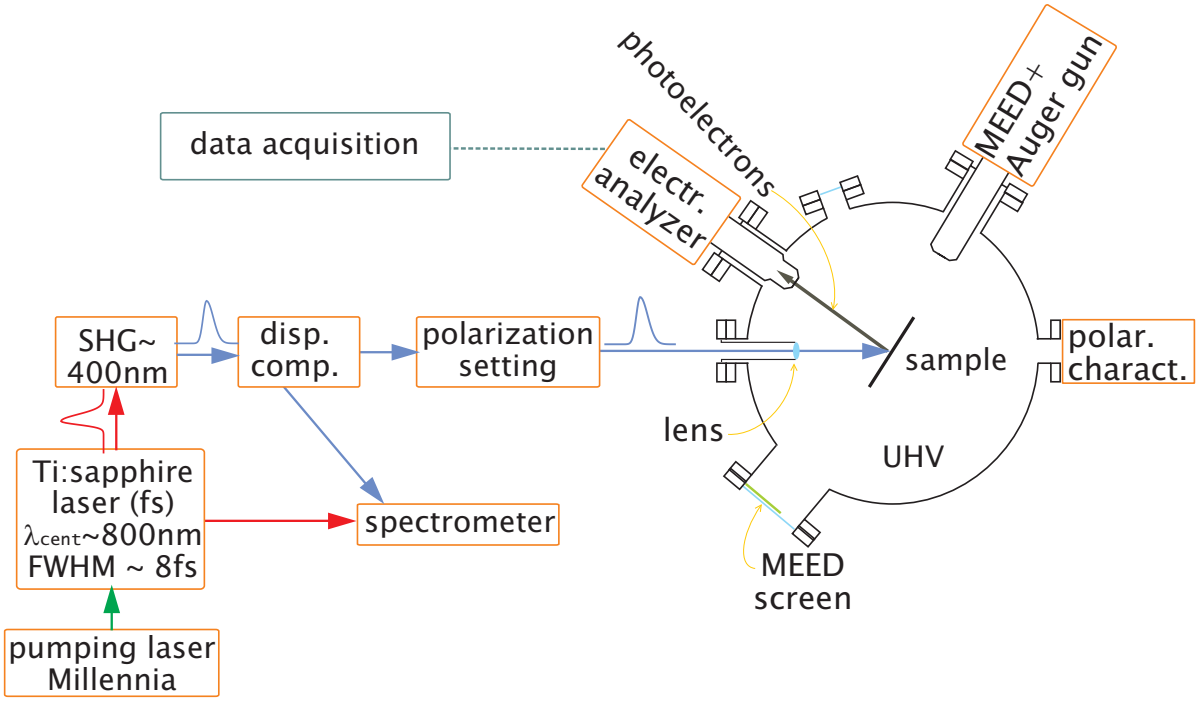

Figure 1.5: Schematic of the experimental setup used for two-photon photoemission experiments.

the electrons are liberated from the sample by the incident photons, their energy is analyzed in an electrostatic analyzer. The whole energetic spectrum of the electrons can be obtained and recorded by a data acquisition computer system. The individual parts of the experiment will be described the detail in the following text.

1.3.1 Femtosecond laser system

The schematic of the laser system used in the experiments is depicted in Fig. 1.6. For generation of the ultrashort pulses, a mode-locking operation is used [14, 15]. The laser cavity design is similar to that of Xu et al. [16]. The laser resonator consists of four planar and two convex dielectric mirrors and one output coupler. The planar mirrors posses negative group velocity dispersion ($\approx -60\,\mathrm{fs}^2$). The output coupler is formed by a glass wedge. Additional glass wedge is placed in the outgoing beam. By moving it towards the beam center a fine adjustment of the dispersion is possible.

As an active medium a considerably doped titanium-sapphire (Ti:S) crystal is used [17], generating the ultrashort pulses by Kerr-lens self-mode-locking [18]. For pumping of the crystal, a Millennia V laser (from Spectra Physics Inc.) is used which produces a beam at 532 nm wavelength by intracavity doubling of 1064 nm beam from the Nd:YVO_4 gain medium. The Ti:S crystal is placed in a special water-cooled holder to avoid its overheating. The pump power is about 5 W.

The negative dispersion mirrors have a design similar to that of Szipőcs et al. [19]. The

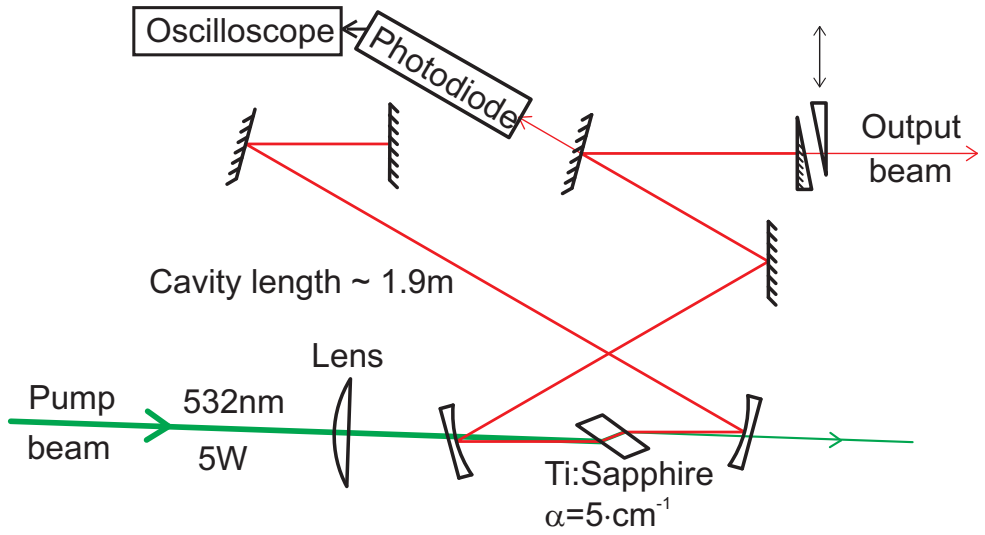

Figure 1.6: Schematic of a home-built laser setup used for the experiments described in this thesis.

dielectric stack of the mirrors is designed so that the resulting group velocity dispersion is achieving values which are not critically spoiling the ultrashort pulse properties.

The length of the laser resonator is $\approx 1.9\,\mathrm{m}$ which gives the repetition rate of the femtosecond pulses of $\approx 80\,\mathrm{MHz}$. The output power is close to 1 W which corresponds to the energy of $\approx 13\,\mathrm{nJ}$ per pulse.

The spectrum of the output beam was monitored always when the beam was not used for the experiment to check the quality of the mode-locking process. One such spectrum is plotted in Fig. 1.7. The estimated minimum pulse width can be deduced from this spectrum. It is well below 10 fs.

A very small part of the laser beam which is not reflected by one of the mirrors is pointed onto a photodiode (see Fig. 1.6) and the resulting signal is visualized on an oscilloscope. This allows to check whether there is always only one pulse propagating within the laser cavity. Propagation of two pulses is leading to a smaller peak intensity and it is also causing an instability of the system.

The laser is located in a semi-sealed box to avoid spoiling of the surfaces of the Ti:S crystal (especially in the beam focus) and mirrors by dust particles. In the box there is an overpressure of nitrogen gas maintained which quite effectively decreases the amount of dust deposited on the important cavity components.

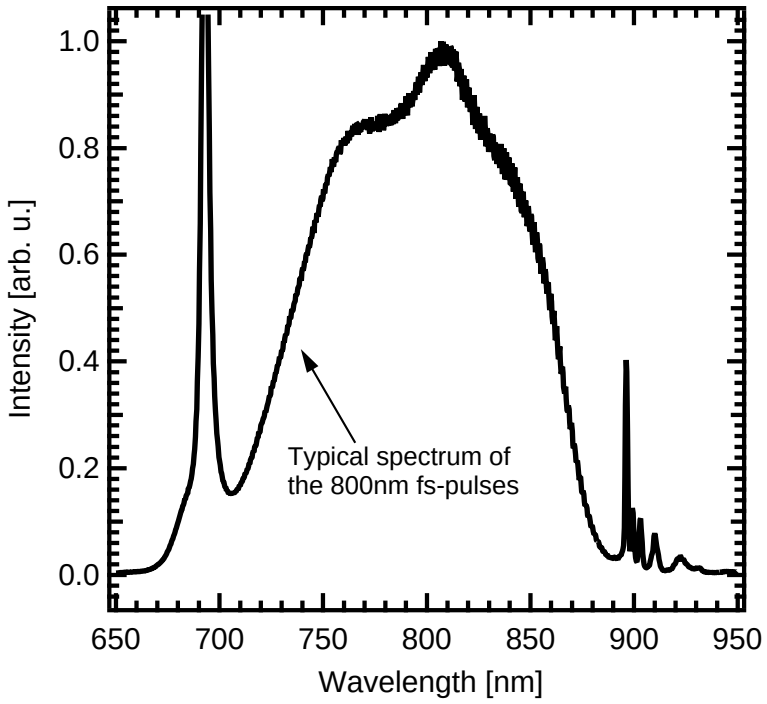

Figure 1.7: A typical spectrum of the 800 nm femtosecond pulses produced by the laser setup.

1.3.2 Frequency doubling and polarization preparation

After the fs-pulse at the 800 nm wavelength is produced in the laser system, it is necessary to double its frequency, so that photons with an energy sufficient for initiation of the two-photon photoemission process are obtained. For the frequency doubling, a β-BaB_2O_4 (BBO) crystal of 80 μm thickness (manufactured by Castech) is used. The conversion efficiency is about 15%, the maximum output power at 400 nm is about 150 mW.

The spectrum of the 400 nm pulses is much smoother compared to the 800 nm pulses which is caused by the effect of phase-matching conditions in the BBO crystal. One typical spectrum of the 400 nm beam can be seen in Fig. 1.8. The width of the spectrum corresponds to ≈18 fs pulse duration.

The knowledge of the changes of the output power from the frequency doubling stage is essential for the treatment of the experimental data as they are related to the intensity of the 400 nm light. It is therefore necessary to monitor changes of the intensity of the exciting beam by measuring the intensity of some residual part of the beam passing through one of the mirrors in the optical path after the frequency doubling.

Continuous nitrogen gas flow is used to avoid dust sticking on the BBO crystal surface

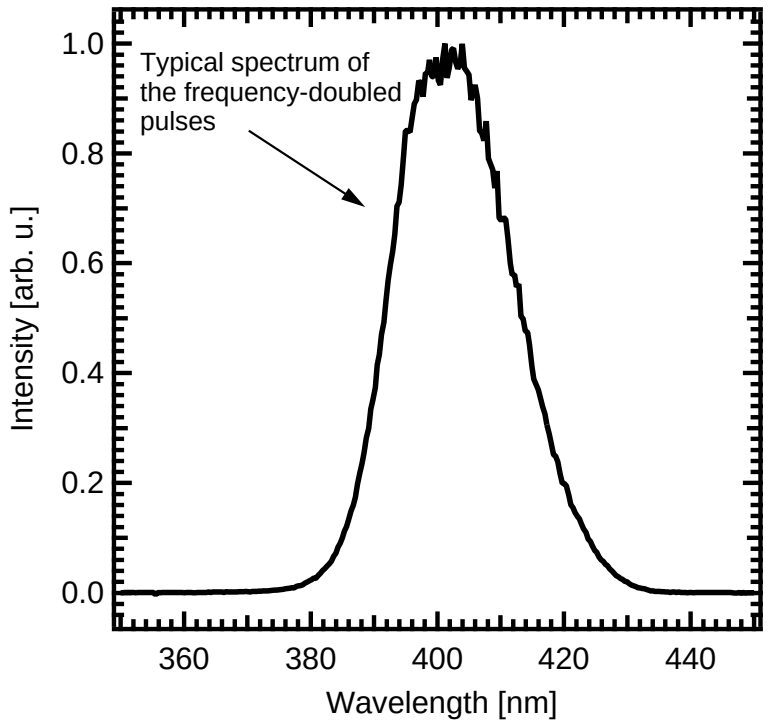

Figure 1.8: A typical spectrum of the 400 nm femtosecond pulses produced by the frequency doubling stage with a BBO crystal.

which would cause a decrease of the efficiency of the second harmonic generation and consequently lower the intensity of the exciting beam.

After the frequency doubling, the dispersion of the pulses is compensated by multiple reflections on negative-dispersion mirrors to achieve the shortest pulse. A set of two thin silica wedges is inserted into the 400 nm beam which allows to adjust the dispersion precisely by changing the effective silica thickness through which the beam has to propagate.

The linear polarization generated by the laser system is preserved by keeping the height of the beam constant along the whole optical path. The polarization desired for the photoemission experiment is set just before the beam is entering the UHV chamber by a set of $\lambda/2$ and $\lambda/4$ achromatic phase plates mounted on motorized rotation stages. The beam is then entering the UHV chamber via a differentially pumped CaF_2 focussing lens ($f = 10\,\mathrm{cm}$) viewport.

After the measurement is finished, a shutter is closing the laser beam of the femtosecond laser before the BBO frequency doubling stage. By this action, the BBO crystal and other experimental equipment is preserved as it is exposed to the laser pulses for the necessary time only.

1.3.3 UHV photoemission chamber

The UHV part of the experiment is schematically plotted in Fig. 1.5. The chamber itself is manufactured from a nonmagnetic stainless steel. Apart from the photoelectron analyzer, various tools for structural and chemical characterization of the sample surface are present in the chamber. Tools for characterization of the laser beam properties are present as well.

Some types of two-photon photoemission experiments (measurements of the magnetic circular dichroism for instance) need very precise adjustment of the polarization at the sample location. However, the polarization of the beam at the sample location cannot be measured with sufficient precision outside the UHV chamber because the viewports of the chamber are influencing the beam polarization by their birefringence. Therefore, a device for characterizing the polarization incident on the surface was mounted in the chamber. It is located just opposite the entrance viewport so that the 400 nm beam is entering directly the device when the sample is removed from the optical path. The tool consists of a rotating analyzer and a photodiode. The signal from the diode is recorded while the analyzer is rotating and the polarization ellipse is calculated from these data. By optimizing the orientations of the $\lambda/2$ and $\lambda/4$ plates before the chamber, a setting

corresponding to the desired polarization is achieved.

The sample is fixed in a holder which can be cooled down to -180°C. Its position can be adjusted in three directions (x,y,z) and in two angles. The angle between the incident beam and the detection axis of the electrostatic cylindrical sector electron energy analyzer is fixed by the chamber design at 35°.

The electrostatic cylindrical sector analyzer was manufactured by the Focus GmbH company. The electrons passing the analyzer can be detected by a channeltron. This detector can be also replaced by a spin analyzer for spin-resolved studies of photoemission from magnetic surfaces. The sample can be biased by a small (a few Volts) potential to achieve better collection efficiency of the photoelectrons by the energy analyzer.

The tools for the sample preparation and characterization include the ion-beam sputtering gun for cleaning the surface of the crystal. When working with atomically flat metal surfaces, the cleaning by ion-beam is necessary every day.

One of characterization techniques available in the chamber for checking of the progress of the sample surface cleaning is the Auger Electron Spectroscopy. It is providing an important information about the contamination of the sample, particularly when cleaning surfaces of crystals which were not kept in the UHV conditions. Other (much more sensitive) option for checking the cleanliness of the surface is based on the observation of saturation of the photoemission signal at energies where is it sensitive to the surface contamination. This will be discussed in Chapter 2, particularly in Sec. 2.2.2.

The orientation of the crystallographic axes of the sample with respect to the exciting beam can be determined by the Medium-Energy Electron Diffraction (MEED). The diffraction pattern is projected onto a phosphor screen and from its symmetry properties the correct setting of the sample can be determined.

There is also a possibility of growing thin metallic layers on the substrate by a Molecular Beam Epitaxy (MBE) technique. The electron beam evaporators used for this purpose were designed by Kirschner et al., further development of the evaporator design is described in [20].

In the chamber there is also a coil consisting of a few turns of a thick copper wire. It allows to switch magnetization of thin magnetic films by pulses of magnetic field. The electric current pulses for this coil are provided by a special pulsed source designed in the electronic workshop of the MPI-Halle.

The external magnetic fields generated outside the laboratory, which would affect the trajectories of low energy electrons, are automatically compensated in all three (x,y,z) directions by a system of large coils mounted on the walls of the laboratory.

1.3.4 Computer control of the experiment

The experiment is almost fully controlled by a personal computer. Writing a program for controlling all necessary devices and acquiring data was also a part of this thesis. The program is communicating with experimental devices via a GPIB bus (PCI-card from Agilent Technologies Inc.) and it is able to measure and to set analogue signals and digital levels by a Keithley KPCI-3108 PCI-card (A/D and D/A converters). Another devices for data acquisition are two multichannel scalers (ISA 7882 Multiscalers by FAST ComTec) which are used for counting TTL pulses.

As the signal from the channeltron detector is in a form of TTL pulses (to each photoelectron is corresponding one pulse), it is acquired by the multiscalers. The multiscaler is storing the data in so-called boxes, whereas the length (in time units) of one box and the number of boxes is specified at the beginning of the measurement. During the data acquisition, some of the parameters of the experiment is usually being changed. For instance, a gradual change of the energy of the detected electrons during the data acquisition results in photoelectron spectrum data stored in the multiscaler boxes. The main advantage of the multiscaler use is that the data can be added into the boxes in multiple runs, synchronized by a trigger signal. In this way, any influence of a possible drift in the acquired signal is minimized.

The measurements of the multichannel scalers and also of the Keithley A/D card can be started by an external trigger signal which allows to measure all the signals synchronously. As the Keithley card has digital and analogue outputs available, one can set also digital levels and analogue voltages during the measurements to modify the experimental settings. Via the GPIB bus, mainly the Owis DC 500 Motor Controller (used for precise setting of motorized stages holding polarizers, phase plates and other optical elements) and the settings of lock-in amplifiers are controlled during the experiment. The digital outputs can control the source of current pulses for the coil used for magnetizing the sample and shutters for closing the beam.

The settings of a particular measurement process are specified in two configuration files. The first configuration file is specifying which channels of the multiscaler and of the A/D card will be used for the data acquisition. The necessary settings for the boxes of the multiscaler (their length and amount) are also specified in this file.

The program is suitable for performing sets of measurements with changing parameters of the experiment. The second configuration file is used for control of these types of measurements. Commands which are to be performed after each individual set of measurements is finished are specified in the file. In this way, the experimental configu-

ration is being changed between acquisitions of individual data sets. These commands can be commands for the GPIB bus, commands setting voltages on the analog input of the D/A card, commands controlling via the settings of digital levels the pulsed current source or the shutters used to close the beam, for instance. The configuration file is written in a simple ad-hoc programming language and can be easily modified to design new types of measurements. Without need of manual control of the experiment by the experimentalist, measurements consisting of many sets of data can be performed in this way. This is bringing better data quality and reproducibility. Experiments running as long as 24-hours (see Chapter 4) are also performed more conveniently.

1.4 Systems studied by two-photon photoemission

As it has been pointed out already in the Sec. 1.1, the two-photon photoemission is a powerful method for studying unoccupied electronic states above the Fermi level. Here we summarize the most important phenomena which can be studied by two-photon photoemission. A main attention will be paid to the surface states.

1.4.1 Surface states

The presence of electronic states localized at a surface of a single crystal was predicted already 70 years ago by Tamm [21] and Shockely [22]. One of the most elegant approaches to the Shockley's surface states phenomenon was presented in 70's by Echenique and Pendry [23]. Their model is assuming that surface states are corresponding to electrons with an energy smaller than the vacuum energy E_{vac} which are trapped between the surface of the crystal (via bandgap) and the surface barrier potential.

Lets consider a wave ψ_+ carrying a unit flux towards the crystal (Fig. 1.9). A portion of

$$\psi_- = r_{\mathrm{C}} \mathrm{e}^{\mathrm{i}\Phi_{\mathrm{C}}} \psi_+ \tag{1.4}$$

will be Bragg reflected, where ψ_- carries the flux towards the surface barrier and $r_{\mathrm{C}}\mathrm{e}^{\mathrm{i}\Phi_{\mathrm{C}}}$ is the corresponding electron reflectivity. This amount of flux will be then reflected on the surface barrier and

$$\psi_+ = r_{\mathrm{B}} \mathrm{e}^{\mathrm{i}\Phi_{\mathrm{B}}} \psi_- = r_{\mathrm{B}} \mathrm{e}^{\mathrm{i}\Phi_{\mathrm{B}}} r_{\mathrm{C}} \mathrm{e}^{\mathrm{i}\Phi_{\mathrm{C}}} \psi_+ \tag{1.5}$$

will travel back towards the crystal. The respective electron reflectivity is $r_{\mathrm{B}}\mathrm{e}^{\mathrm{i}\Phi_{\mathrm{B}}}$. It is obvious that for a bound state at the surface the conditions

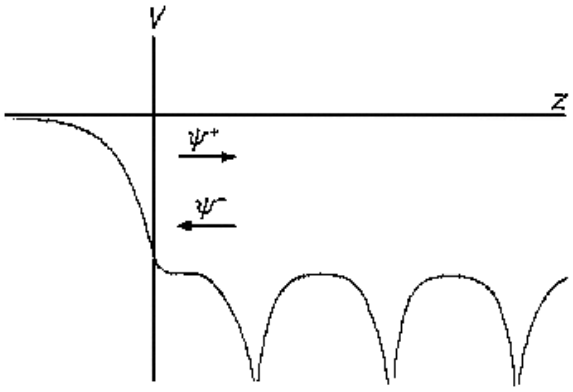

Figure 1.9: Schematic of a potential at the crystal surface showing atomic potentials and the surface barrier (after [23]).

$$r_{\mathrm{B}} r_{\mathrm{C}} = 1 \,, \tag{1.6}$$

$$\Phi_{\mathrm{B}} + \Phi_{\mathrm{C}} = 2\pi n \qquad (n = 0, 1, ...) \tag{1.7}$$

have to be satisfied.

Considering a flux conservation, equation (1.6) implies $r_{\mathrm{B}} = r_{\mathrm{C}} = 1$. The phase condition will not be satisfied for any arbitrary energy E and momentum parallel to the surface $k_{||}$ (the perpendicular and parallel motion of the electron is fully separable in this model). The phases are functions of energy, so a detailed calculation is needed for determination of the position of the surface states on the energy scale [23, 24].

The solution of equation (1.7) for $n = 0, 1, ...$ gives a series of surface states. The "ground" state $n = 0$ is usually called *Shockley state* (or *surface resonance*) because it is corresponding to Shockley's calculation in 30's [22, 25]. States for $n > 0$ are usually called *image potential states*, contrary to the Shockley state they are less localized and are extending more into the vacuum. They are forming a Rydberg-like series on the energetic scale. In the most simple view [26] one can write for their energies

$$E_{\mathrm{vac}} - E_n = \frac{0.85\,\mathrm{eV}}{n^2} \qquad n = 1, 2, .. \tag{1.8}$$

The total energy of individual states is then given as

$$E_n(\boldsymbol{k}) = E_n + \frac{\hbar^2 k_{||}^2}{2m_e} \,, \tag{1.9}$$

where $k_{||}$ is a component of the wavevector parallel to the sample surface. In this approximation, the electrons are treated as free in the surface plane, so their effective mass (for the effective mass definition see [27], for instance) is equal 1. When interacting with

the electromagnetic waves, the surface states are for symmetry reasons sensitive only to excitation having a non-zero component of the $\boldsymbol{E}$ vector perpendicular to the sample surface. This means that the light linearly polarized perpendicularly to the plane of incidence doesn't interact with the surface states.

The surface states were already observed by the inverse photoemission [28, 29] and by the two-photon photoemission [30, 31] for various metallic surfaces. However, in the experiment presented in Chapter 2 the relation of the exciting photon energy and the sample Fermi energy is causing that the surface states will affect the observed photoemission spectra mainly due to the three- and four-photon processes.

1.4.2 Other applications of two-photon photoemission

Other applications of two-photon photoemission can be found in surface chemistry. The two-photon photoemission signal is emerging from the topmost layers, so it is extremely influenced by the cleanliness of the surface. Therefore, an influence of adsorbates can be studied with high sensitivity [32]. The main power of the two-photon photoemission experiment is the possible achievement of time resolution. This allows experimental studies of ultrafast processes at the surface of the investigated sample to be performed. Overview of studies of the desorption of alkali atoms from noble metals can be found in [33] or [34].

Two-photon photoemission can be used also for more general and fundamental studies of the hot electron population dynamics [8, 35–41]. Transport effects can be also detected [42]. In the photoelectron detection part of the experiment, a spin-analyzer can be incorporated and the spin-resolved information about the hot-electron dynamics can be obtained as well [43].

While combining Photoemission Electron Microscopy (PEEM) setup with the two-photon excitation one can achieve a spatial resolution for investigating surface inhomogeneities [44, 45].

In conclusion, in this chapter we have summarized the theoretical and experimental background of the two-photon photoemission technique. The experimental apparatus for this method was described and the most important phenomena which can be investigated by this technique were summarized.

Chapter 2

Multiphoton photoemission from Cu(001) surfaces

In this chapter, the results obtained on Cu(001) surfaces by means of the two- and more than two-photon photoemission will be discussed. The advantage of this choice is that copper has a well known electronic structure and it was studied also quite recently even with the two-photon photoemission method [8, 32]. Because the experimental setup has several parameters (especially the peak photon flux density) better than those used in previous experiments, a better observation of known effects and detection of new phenomena is expected. The most important experimental result presented in this chapter will be the observation of multiphoton (up to four-photon) excitation of photoelectrons with an efficiency which is enhanced by a presence of surface states and bulk Bloch states.

2.1 Normal emission geometry

In this section, the experimental data obtained in a photoemission experiment on a Cu(001) surface in normal emission geometry will be presented. Quite intense femtosecond pulses were used for the excitation. The observation of higher-order effects will be discussed.

The photoemission experiments with the Cu(001) surface were performed in a UHV apparatus ($p < 10^{-10}$ mbar). The surface was optically excited by frequency-doubled pulses from a Ti:sapphire oscillator. A central energy of the frequency-doubled pulses was $E_0 = 3.07$ eV, the corresponding excitation spectrum linewidth was ~ 0.17 eV, the pulse duration (i.e. the intensity FWHM) was < 18 fs, the pulse energy was ~ 1 nJ. The

beam was focused on a small area ($\sim$ 20 μm in diameter) of the specimen surface which resulted in the peak power of the order of 10^{10} W·cm^{-2}. The apparatus was described in detail in Sec. 1.3.

A clean and ordered Cu(001) surface was obtained by repeated sputtering and annealing cycles. For the sputtering, the Ar^+ ions accelerated by 1 keV voltage were used, the annealing temperature was 870 K. The surface quality during the sample cleaning cycles was checked by the Auger Electron Spectroscopy, the Medium-Energy Electron Diffraction (MEED) and above all by reaching the saturation of the photoemission signal related to the excitation via surface states (7.1 eV final state energy). The orientation of the scattering plane was parallel either to the Cu[100] or Cu[110] axis and it was checked by the Medium-Energy Electron Diffraction (MEED).

The Cu crystal was biased at -1 V to achieve a better efficiency of the photoelectron detection. It was possible to vary the angle of incidence from -15° to 85° (i.e. -50° to 50° emission angle).

2.1.1 The s and p excitation at normal emission geometry

The data reported in this section were acquired at normal emission geometry which corresponds to a 35° angle of incidence of the exciting beam. Two linear polarizations were used for the excitation — the p polarization with the electric field vector in the incidence plane and the s polarization with the electric field vector perpendicular to the incidence plane. The respective photoemission intensities are reported in Fig. 2.1 (linear scale) and in Fig. 2.2 (logarithmic scale). The energy of the detected electrons is denoted with respect to the Fermi level, E_F. In the figures, there are also indicated energies corresponding to the electrons excited from the Fermi level by two and three photons. The $E_F + 2\hbar\omega$ energy can be understood as a border between the two- and three-photon excitation, whereas the $E_F + 3\hbar\omega$ energy is a border between the three- and four-photon excitation.

In the right panel of Fig. 2.1, the band structure of Cu(001) along the Δ line calculated by Burdick [46] is plotted. The symmetry of the bands involved in the photoemission process is also indicated in the figure. The selection rules (in dipolar approximation) applicable to the normal emission geometry allow $\Delta_1 \rightarrow \Delta_5$ and $\Delta_5 \rightarrow \Delta_1$ transitions for both s and p excitation, whereas the $\Delta_1 \rightarrow \Delta_1$ transition is allowed for the p excitation only [47]. There is also a restriction on the final state symmetry — in the normal emission configuration it should posses the Δ_1 symmetry.

In the two-photon photoemission region (the final state energies up to 6.2 eV), the

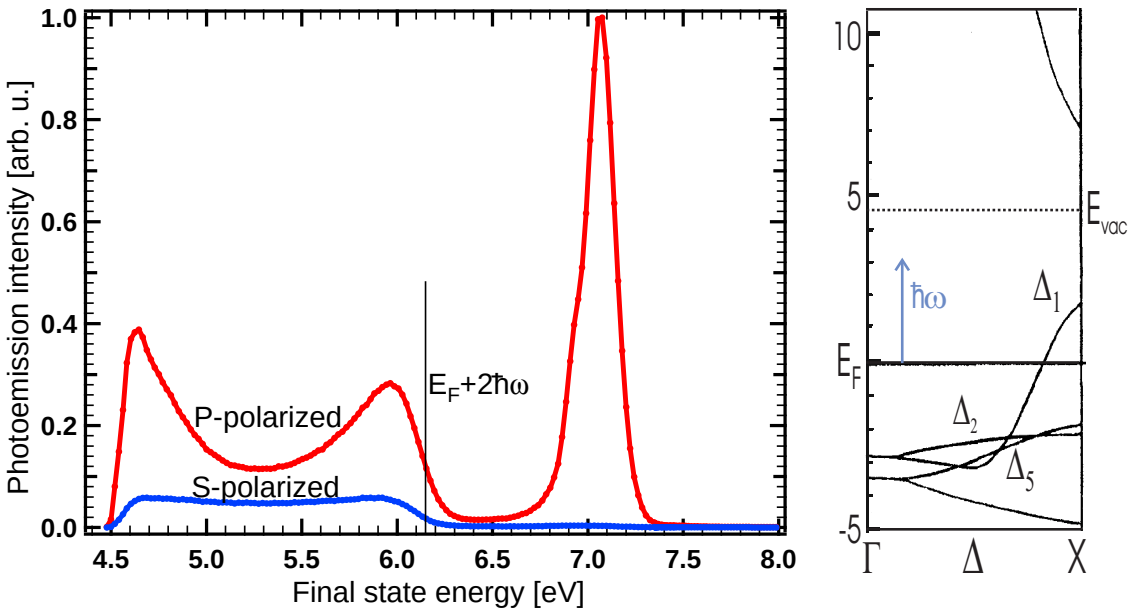

Figure 2.1: Left panel: Photoemission signal as a response to p- and s-polarized excitation of the Cu(001) surface. Right panel: Band structure of copper along the Δ line as calculated by Burdick [46], the energy scale is in electronvolts.

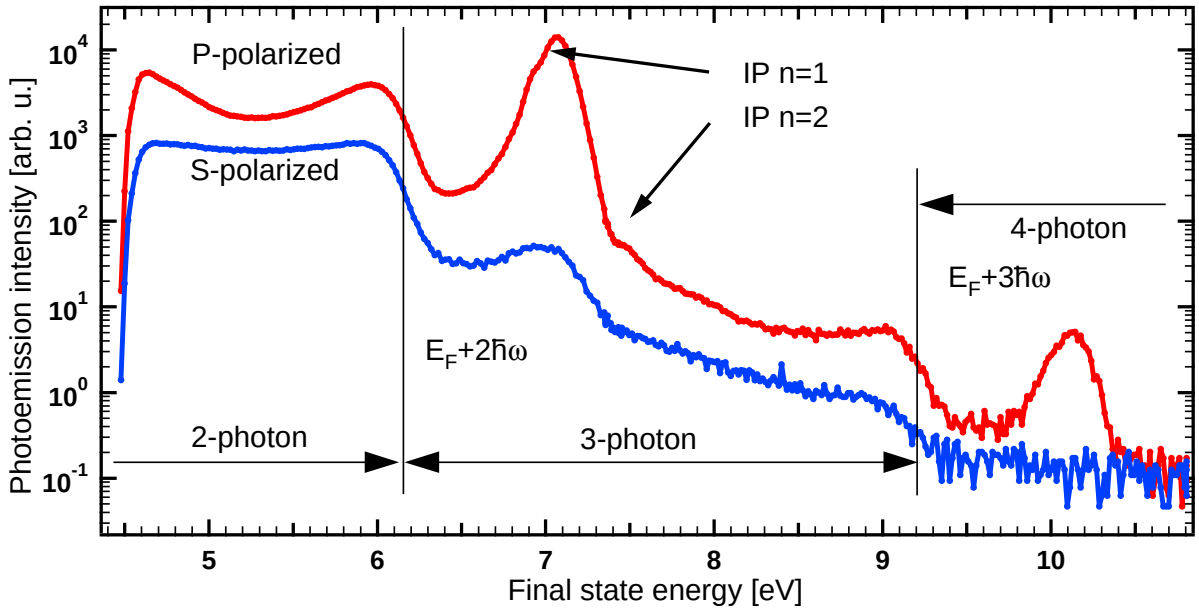

Figure 2.2: Photoemission signal from Cu(001) for p- and s-polarized excitation beam in logarithmic scale. Multiphoton processes are clearly visible.

initial states are mainly the sp-band states with Δ_1 symmetry. Only the enhancement of the photoemission intensity at the low energy cutoff can be attributed to the excitation from d-band states with a Δ_5 symmetry. As the two-photon excitation by s-polarized light from d-band can proceed only in the $\Delta_5 \rightarrow \Delta_1 \rightarrow \Delta_5$ sequence, the enhancement is only weekly observable in the s-polarized light. It is contributing by off-normal emission only which is because of $\pm 2.5^\circ$ angular acceptance of the electron analyzer also partly detected in the normal emission configuration.

Another enhancement of the photoemission signal in the two-photon photoemission region is observable at $\approx 6.0\,\mathrm{eV}$, close to the two-photon replica of the Fermi edge. The feature is again much more intense with the p-polarized excitation. It can be ascribed to a tail of density of states diffusing from the n=0 surface resonance (see Sec. 1.4.1). The surface resonance has Δ_1 character [32] which implies possible excitation pathways $\Delta_1 \rightarrow \Delta_1 \rightarrow \Delta_1$ and $\Delta_1 \rightarrow \Delta_5 \rightarrow \Delta_1$ for the p excitation. Only $\Delta_1 \rightarrow \Delta_5 \rightarrow \Delta_1$ transition is allowed for s excitation, but it is unfavorable due to symmetry constrains of the surface state in addition, as the surface state needs a component of the electric field vector perpendicular to the surface to be excited. Only virtual states can act as intermediate states within this energy region.

The above described features are a result of the two-photon excitation process. The photoelectrons detected at energies above $E_F + 2\hbar\omega$ are results of the multiple-photon excitation and will be discussed in the following text.

2.1.2 Multiphoton processes

The figures 2.1 and 2.2 are showing that the highest photoelectron yield is observed at energies around 7.1 eV. To reach such an energy of a photoelectron, at least three photons have to act in the excitation process. The occurrence of such a strong signal in the three-photon photoemission region is quite surprising as the electron yield is normally decreasing with increasing order of the nonlinearity. The reason why such a strong signal is observed here is in the resonant character of the process which will be described below.

The most pronounced feature in the three-photon photoemission region in the p-excited spectrum is the peak close to 7.1 eV. Its magnitude is about four times as large as the two-photon photoemission signal at 6.0 eV. The peak is having a shoulder at 7.0 eV. Also the spectrum excited by the s-polarized beam is showing (although much less intense) peak at 7.0 eV. The band structure and the related excitation schematic is plotted in Fig. 2.3. The first step of the excitation process is common for both s and p polarization. It involves excitation of an electron from an occupied d-band with Δ_5 symmetry to

an unoccupied sp-band with Δ_1 symmetry. It should be noticed that the n=0 surface resonance can also play a role in the p-excited process.

In the case of s-polarized light, the only path in which the three-photon excitation can proceed is $\Delta_5 \rightarrow \Delta_1 \rightarrow \Delta_5 \rightarrow \Delta_1$. From this fact and from the lack of the component of the exciting electric field vector perpendicular to the surface it follows that the n=1 image potential state with Δ_1 symmetry cannot play any role in the s-excited spectra. From the sp-band a direct two-photon process (via a virtual intermediate state) lifts the electron to a vacuum state. The peak at 7.0 eV is an indication of the transition from the top of a d-band with Δ_5 symmetry which is having higher density of initial states than the sp-band. For higher final state energies, only the sp-band states can contribute as initial states.

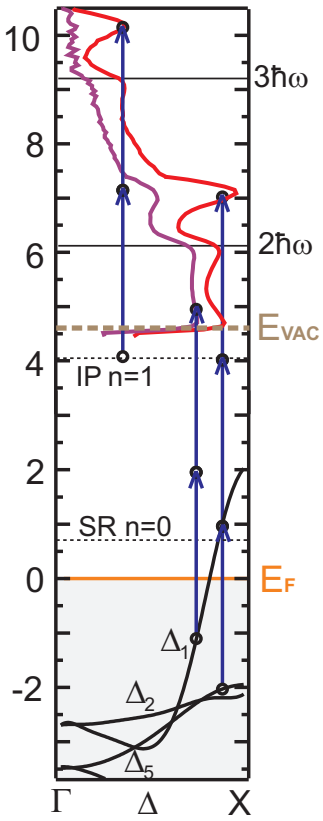

Figure 2.3: The band structure of Cu(001) along the Δ line with indication of the process leading to the huge peak in the p-excited photoemission spectrum.

The p-excited spectrum is showing at 7.1 eV much more intense peak due to the fact that also the n=1 image potential state can be resonantly populated (the excitation scheme $\Delta_5 \rightarrow \Delta_1 \rightarrow \Delta_1 \rightarrow \Delta_1$ is allowed for the p-polarized light). The energy position of the n=1 image potential state E_1 calculated from the energy of the observed peak is $E_1 = 7.1\,\mathrm{eV} - \hbar\omega = 4.03\,\mathrm{eV}$. This is in a good agreement with previous experimental observations [48–52]. The shoulder at 7.0 eV is a sign of a superposition of the excitation via the image potential state and the excitation scheme described already for the s-polarized light. This is because the in-plane component of the p-polarized light is having the same symmetry properties as the s-polarized light. It should be noted that the surface-states-enhanced feature at 7.1 eV is in recent observations much more intense than in previous multi-photon photoemission studies by Ogawa and Petek [32].

In addition to the large peak at 7.1 eV, a small peak corresponding to the excitation via the n=2 image potential state can be observed at the final state energy of 7.5 eV. This feature is gaining less from the higher density of d-band states as its initial state is at $\approx -1.7\,\mathrm{eV}$, however is it still well resolved. The calculation of the n=2 image potential state energy gives $E_2 = 7.5\,\mathrm{eV} - \hbar\omega = 4.43\,\mathrm{eV}$. This is again in a good agreement with previous observations [49].

For energies larger than 7.5 eV, the intensities of both s- and p-excited spectra are

decreasing roughly exponentially up to the next Fermi edge imprint located at $3\hbar\omega \approx 9.2\,\mathrm{eV}$ final state energy. As the initial states posses the Δ_1 sp-band symmetry, the s excitation can proceed only in the $\Delta_1 \rightarrow \Delta_5 \rightarrow \Delta_1 \rightarrow \Delta_5$ pathway whose final state is not detectable in the normal emission experimental geometry. Therefore, only because of the nonzero angular acceptance of the electron energy analyzer the photoelectrons are detected also in the case of s-polarized excitation. The p-excitation is not limited so strongly as its final state can posses the Δ_1 symmetry. The intensity of the p-excited spectra is therefore about 5-times larger.

One interesting aspect of the spectrum generated by the p-polarized excitation is that it is not reproducing the peak observed below the two-photon Fermi edge at 6.0 eV also in the three-photon photoemission region. The feature is very much reduced for the three-photon excitation. This can be attributed to a fact that the final states at the energy $\approx 9.1\,\mathrm{eV}$ are already lying within the projected bulk band structure (Fig. 2.1). In the 6.0 eV region, the final states of the excitation process in the bulk are only extremely shortly living virtual states. The enhancement of the photoemission signal by the surface resonance is therefore clearly observable at 6.0 eV, as it is influencing the electrons located at the surface only. In the 9.1 eV region, the situation is different, as the final states are within the projected bulk band structure and thus have longer lifetime. Not only surface electrons are escaping into the vacuum in this case, therefore the effect of the surface resonance is not so important.

Above the three-photon imprint of the Fermi edge ($E_F + 3\hbar\omega$) one well resolved peak is observed at 10.2 eV in the p-polarized light. Its energy is just $\hbar\omega$ above the huge peak at 7.1 eV, its intensity is about $2500\times$ reduced. It can be concluded that the excitation mechanism is the same as in the case of 7.1 eV peak, the only difference is that a two-photon process (via a virtual state) takes place in the last step of excitation from the n=1 image potential state to the final vacuum state. With the s-polarized excitation this feature is already not resolvable due to a very low signal level (~ 4 orders of magnitude less than its maximum at the 5 eV final state energy — see Fig. 2.2).

In this section, the photoemission spectra acquired by means of multiphoton photoemission were presented and the observed spectroscopic features were discussed. The high photon flux density was allowing to observe features which have not been observed before by laser-excited photoemission spectroscopy.

2.2 Off-normal emission

The normal emission spectra from Cu(001) surfaces described in the previous section showed several features which could be interpreted with help of a fact that the selection rules in the normal emission geometry are quite restrictive, at least in the case of s-polarized excitation. However, it is also useful to perform measurements at different emission angles. The angle-resolved photoemission can probe the dispersion of individual electronic states involved in the excitation process and thus help in classifying the features observed in the photoemission spectra. In the first part of this section, the results of an angle-resolved experiment will be therefore presented and the observed phenomena will be discussed.

Electronic states at surfaces are generally very sensitive to the surface quality. Adsorbates at the surface can modify the spectra significantly. On the other hand, the behavior of the spectroscopic features while changing the surface properties by adsorption of adatoms is also a good method which can be used for determination of the character of the processes involved in the photoexcitation. Therefore, in the second part of this section the results of the photoemission experiment on the Cu(001) surface exposed to oxygen will be presented.

2.2.1 Off-normal photoemission — dispersion of surface states

The photoemission spectra at varying emission angles were acquired along both $\overline{\Gamma}\overline{\mathrm{X}}$ and $\overline{\Gamma}\overline{\mathrm{M}}$ directions of the surface Brillouin zone [9], i.e. the orientations of the incidence plane are parallel to the [011] resp. [001] crystallographic axes of the surface. One set of data acquired along the $\overline{\Gamma}\overline{\mathrm{X}}$ direction is displayed in Fig. 2.4.

The spectra excited by p-polarized light are showing one strongly dispersing feature which can be related to the n=1 surface state dispersion, starting from 7.1 eV at normal emission. The 7.0 eV shoulder appearing at normal emission is almost not dispersing and can be therefore attributed to the d-band contribution to the photoemission signal as discussed already in the previous section. The dispersion of the small peak corresponding to the n=2 surface state can be detected up to $\approx 25^\circ$ emission. The peak at 6.0 eV, close to the two-photon Fermi edge imprint is gradually disappearing for increasing emission angles. This supports the idea that its origin is a consequence of the n=0 surface resonance.

The spectra excited by s-polarized light are not showing so interesting behavior. The d-bands involved are not dispersing much in the observed region. The surface states

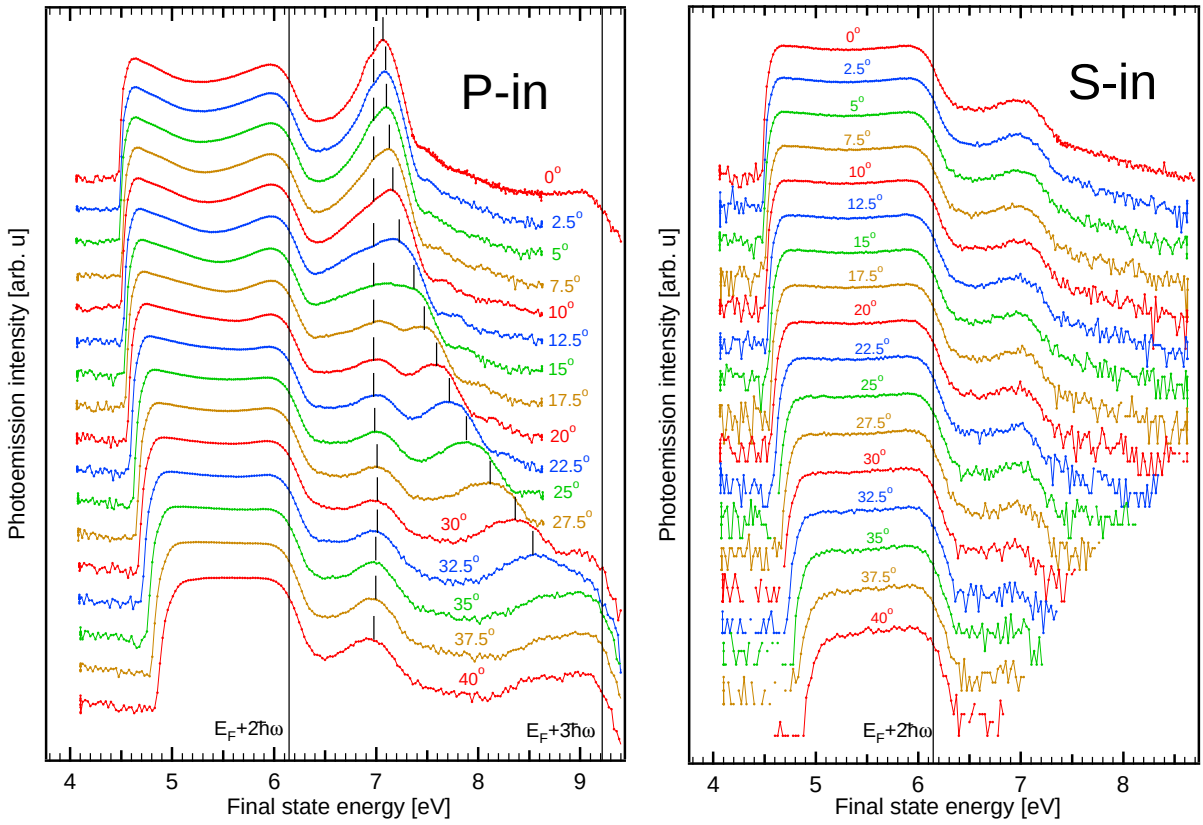

Figure 2.4: The photoemission spectra of Cu(001) at room temperature measured as a function of the emission angle. The sample orientation was corresponding to the $\overline{\Gamma}\overline{X}$ direction. In the left panel the spectra for p-polarization incident on the sample are displayed, in the right panel the s-polarization is used for excitation. The obtained dispersion relations are displayed in Fig. 2.5 and in Fig. 2.6.

cannot be populated by s-polarized light.

The positions of peaks observable in the angle-resolved measurements where the exciting light was p-polarized are summarized in Fig. 2.5. It is clearly seen that the n=1 and n=2 image potential states show a free-electron-like quadratic dispersion, as expected from the theory (Eq. 1.9) and from the previous results obtained by the inverse photoemission [50] and by the two-photon photoemission [29, 49] measurements. The dispersion of the n=0 surface resonance measured by Hulbert et al. [50] is also indicated in the figure.

In the vicinity of the $\overline{\Gamma}$ point, no dependence of the effective mass on the crystal orientation was observed. However, for larger emission angles (>30°) the dispersion of the surface state in the $\overline{\Gamma}\overline{X}$ direction slightly differs from the parabolic behavior. The

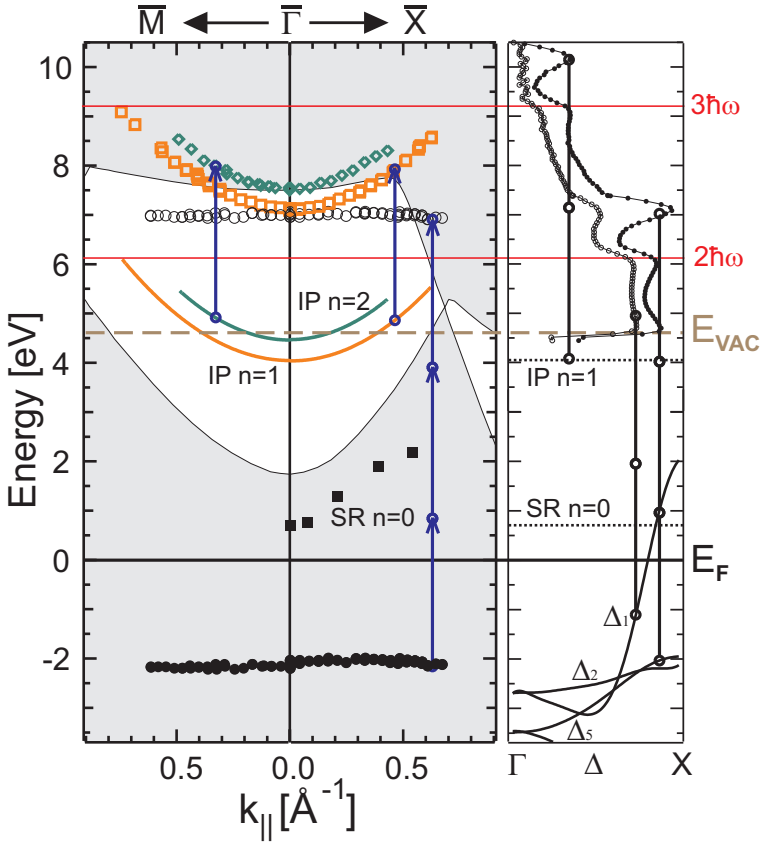

Figure 2.5: Left panel: Surface projected band structure of Cu(001) with the results of the angle-resolved photoemission experiment. The open symbols indicate the final states peaks. Circles represent the enhancement of the signal due to the higher density of d-band states. Corresponding initial d-band states are indicated by solid circles. Squares represent the n=1 IP state resonant enhancement, diamonds the n=2 IP state resonant enhancement. Solid squares represent the n=0 surface resonance [50]. Right panel: The band structure of Cu(001) along the Δ line with indication of the excitation process leading to the huge peak in the p-excited spectrum at normal emission geometry.

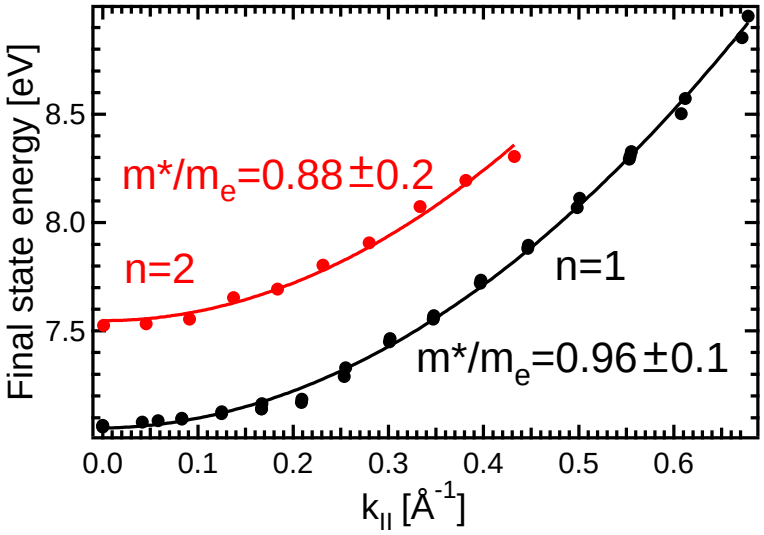

Figure 2.6: Calculation of the effective masses of the n=1 and n=2 image potential states. Data from multiple experiments in the $\overline{\Gamma X}$ direction are compiled and the effective masses are extracted.

reason for this is most probably the fact that the surface state energy position is already almost outside the bulk projected band gap and can therefore mix with the bulk states. The bulk projected band gap is in Fig. 2.5 indicated by white background color, the surface state dispersion curve is leaving the gap at $k_{||} \approx 0.65\text{Å}^{-1}$. In the $\overline{\Gamma}\overline{\text{M}}$ direction, the gap is larger, so that the parabolic dispersion can be observed even for larger values of $k_{||}$.

From the positions of the observed dispersing peaks the effective mass m^*/m_e of the image potential states can be obtained. Firstly, the value of $k_{||}$ is calculated from the energy position of the dispersing peak E and the emission angle ϑ

$$k_{||} = \sin\vartheta \sqrt{\frac{2m_e}{\hbar^2}(E - \Phi)} \ . \tag{2.1}$$

Then the corresponding $k_{||}$ and E values are coupled by a dispersion relation

$$E = \frac{\hbar^2 k_{||}^2}{2m^*} + E(\vartheta = 0) \ , \tag{2.2}$$

where the effective mass m^* stands as a parameter. It can be easily obtained by a numerical fit. The theoretical value of m^*/m_e is equal 1 (see Sec. 1.4.1). The experimental dispersion curves in the $\overline{\Gamma}\overline{\text{X}}$ direction for n=1 and n=2 image potential states with quadratic fits are plotted in Fig. 2.6, the resulting effective mass is $m^* = (0.96 \pm 0.1)\, m_e$ for the n=1 image potential state and $m^* = (0.88 \pm 0.2)\, m_e$ for the n=2 image potential state. This is within the experimental accuracy coherent with the theoretical values.

2.2.2 Effect of oxidation

It is well known that the oxygen coverage influences the work function of the Cu(001) surface [53]. With increasing oxygen coverage the work function is increasing up to a 0.5 monolayer coverage. The maximum work function shift is about 0.3 eV. At room temperature the 0.5 ML coverage is reached at $\approx 150 - 200$ L exposures. Here 1 L (Langmuir) $= 10^{-6}$ Torr·s.

It was experimentally observed [29, 54, 55] that the surface states are pinned to the vacuum level. When the work function Φ increases, the energy position of the surface states with respect to the Fermi level is increasing as well. In addition, the oxygen adsorption is quenching the surface states. Experimental observations of the behavior of the gradually oxidized Cu(001) surfaces in the multiphoton photoemission regime can therefore elucidate the origin of the observed spectroscopic features in the photoelectron spectra and thereby support the explanations given already before in this chapter.

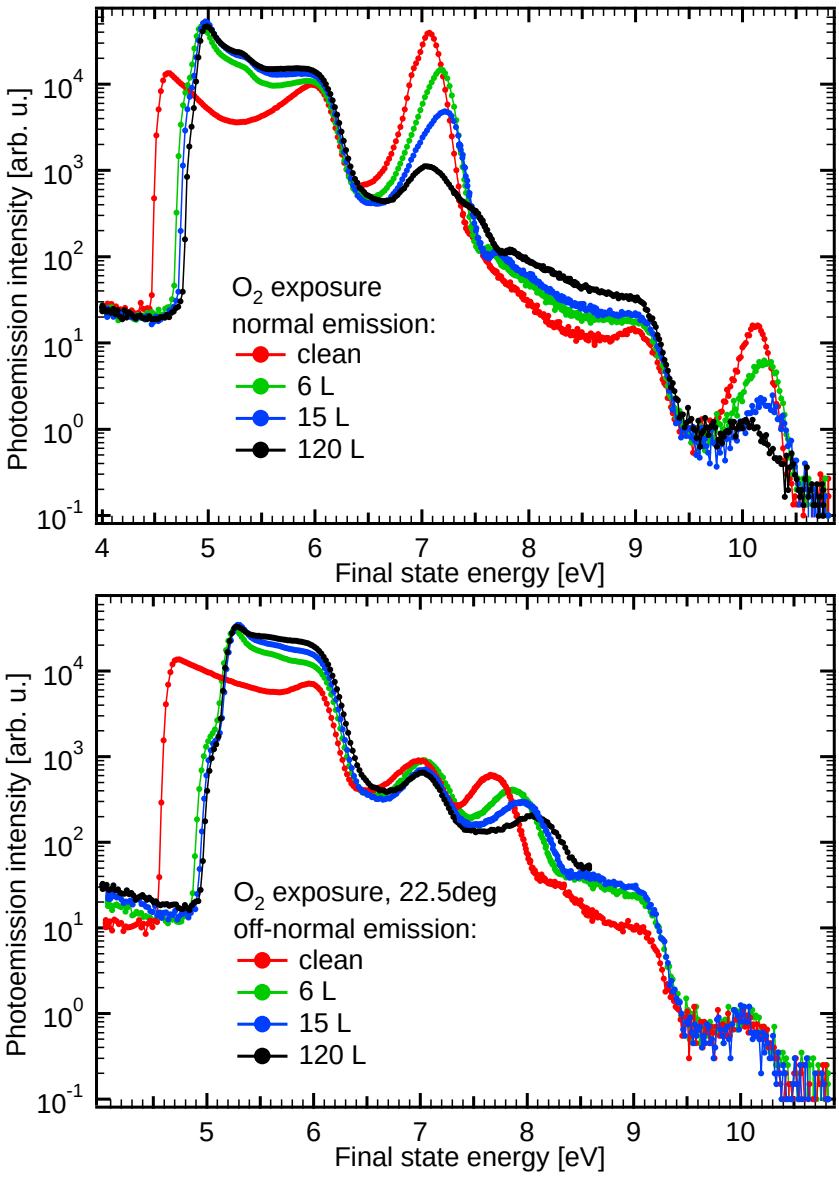

Figure 2.7: Effect of oxidization on the photoelectron spectra of Cu(001). The exciting beam was p-polarized.

The p-excited photoemission spectra acquired on the Cu(001) surface which was exposed to oxygen are displayed in Fig. 2.7. Both normal and off normal photoemission spectra were recorded while the exposure was gradually increased up to 120 L. The off-normal emission spectra are more easily interpreted because the d-band contribution and the surface states contribution are well separated in energy in this case. It is clearly observed that the d-band contribution to the photoemission signal is only slightly affected

by the oxygen adsorption. The surface state feature is shifting to higher energies with increasing O_2 coverage, as an expected manifestation of the surface states pinning to the vacuum level, E_{vac}.

The normal emission spectra are showing similar behavior. The magnitude of the huge peak at 7.1 eV is decreasing with increasing O_2 coverage. Taking into account the off-normal emission spectra, it can be stated that the main reason for the intensity decrease is the loss of the resonance condition (see Fig. 2.3) when the work function (and thereby the image potential state energy) is increasing. The same effect is also observable in the four-photon photoemission region.

From the behavior of the off-normal emission spectra it can be concluded that the quenching of the surface states by oxygen adsorption is not so strong. After 120 L coverage, the corresponding spectroscopic features are still well observable. This is coherent with the fact that when populating the image potential states, the electrons are well separated from the surface. The influence of the oxygen adsorption on the observed spectra is quite complex (mainly in the two-photon photoemission part). Its complete explanation goes beyond a scope of this thesis.

However, the behavior of the photoemission spectra under exposure of the Cu(001) to oxygen is fully supporting the interpretations of the spectroscopic features in the multiphoton photoemission spectra given in this chapter up to now. The resonance between bulk electronic states and surface states is giving rise to the most spectacular effects.

In conclusion, in this chapter the photoemission experiments with high photon flux densities were presented. One of the most interesting aspects is that the photoemission signal is observed even for energies higher than $E_{\mathrm{vac}} + \hbar\omega$ which implies that an intermediate state above the vacuum level is involved in the excitation process. It can be either a virtual state (then the last excitation step is a real two-photon process) or a real state. As the last intermediate state is located in the gap of the surface projected band structure (with exception of $k_{||} > 0.5\,\mathrm{\AA}^{-1}$ region in the $\overline{\Gamma}\overline{\mathrm{X}}$ direction), the only real intermediate states available are the image potential states for larger values of $k_{||}$ (see Fig. 2.5). An electron excited into such an intermediate state has already enough energy to escape into vacuum, but before it is completely separated from the sample, it is excited by another photon to even higher energy. Such a process is called an *above-threshold ionization* (ATI). It has been already well established in experiments with atoms [56] and molecules [57]. Several experiments were reported also in solids [58–60], some results were published recently [61]. However, the four-photon photoemission regime in solids with clearly pronounced electronic features was obtained in this work for the first time to our knowledge.

In this chapter, the individual contributions to the photoemission spectra were identified and discussed with help of the angle-resolved measurements and oxygen adsorption. It was proven that the experimental setup is capable of achieving photon flux densities which are able to find new physical processes as the above-threshold ionization up to the four-photon photoemission regime.

Chapter 3

Studies of surface magnetism by the Second Harmonic Generation (SHG) technique

In previous chapters, the photoemission technique was introduced as a method suitable for studies of surface properties of solid materials. In this chapter, another surface-sensitive technique will be described which is the Second Harmonic Generation (SHG). It is a very versatile and sensitive tool allowing an in-situ and ex-situ characterization of surface properties, including surface magnetism. In the beginning of this chapter, a theory of the surface-generated SHG will be summarized. Then, the complexity added by the surface magnetism will be addressed. At the end of this chapter, the experimental apparatus used for the SHG experiments will be described.

3.1 Theory of the surface second harmonic generation

In this section, the theory of the optical second harmonic generation will be reviewed. The focus will be put on the description of the SHG signals generated from surfaces. This is the principle of the SHG-based methods for studying surface properties of solid materials.

The discovery of maser by Maiman in 1960 [10] allowed to reach much higher photon densities than before. Therefore, the threshold for observing a generation of higher optical harmonics from various materials was overcome [62]. Already in early papers of

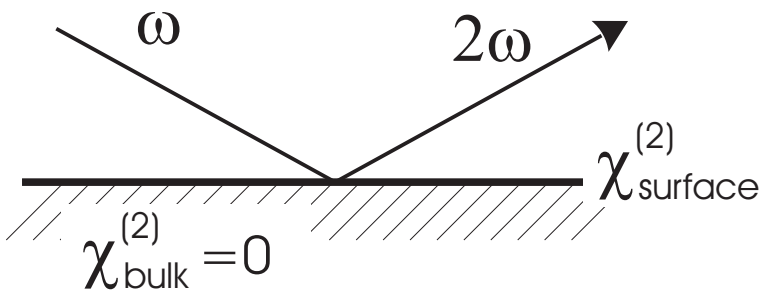

Figure 3.1: A schematic view of the second harmonic generation from centrosymmetric material.

Bloembergen [63], it was predicted that the surface should be contributing to the second harmonic generation signal. Decades later in 1989, it was proposed to use SHG as a surface sensitive probe of magnetism [64, 65] and in a short time the method was also experimentally used by Reif et al. [66].

The SHG arises from a nonlinear polarization induced by an incident electromagnetic field $\boldsymbol{E}(\omega)$ which writes

$$\boldsymbol{P}(2\omega) = \boldsymbol{\chi}^{(2)}\boldsymbol{E}(\omega)\boldsymbol{E}(\omega) + \boldsymbol{\chi}^{(Q)}\boldsymbol{E}(\omega)\nabla\boldsymbol{E}(\omega) + ... \tag{3.1}$$

The nonlinear susceptibility tensor $\boldsymbol{\chi}^{(2)}$ is zero in centrosymmetric media because of symmetry reasons. In these materials, the bulk nonlinear polarization is limited to the quadrupole term $\boldsymbol{\chi}^{(Q)}\boldsymbol{E}(\omega)\nabla\boldsymbol{E}(\omega)$. However, the symmetry is broken at the surface or at the interfaces and therefore the dipole contribution in Eq. 3.1 can be observed even in centrosymmetric media (see Fig. 3.1), but it is limited to a small region of one or two atomic planes at the surface or interface. The bulk quadrupole effect is not limited to the small surface volume. However, there is still a limitation of the penetration depth of the incident radiation. For a large number of materials, this contribution is still negligible and therefore the SHG can be used as a useful tool for studies of surface properties in such systems. In addition, one has to deal with the effects of light propagation in the material.

For highly symmetric materials, most of the tensor elements of $\boldsymbol{\chi}^{(2)}$ are zero for symmetry reasons. If we take as an example the (001) surface of a cubic crystal, $\boldsymbol{\chi}^{(2)}$ can be written in the form

$$\boldsymbol{\chi}^{(2)} = \left(\begin{array}{ccc|ccc} 0 & 0 & 0 & 0 & \chi_{xxz} & 0 \\ 0 & 0 & 0 & \chi_{yyz} & 0 & 0 \\ \chi_{zxx} & \chi_{zyy} & \chi_{zzz} & 0 & 0 & 0 \end{array}\right) . \tag{3.2}$$

	Non-zero elements of $\boldsymbol{\chi}^{(2)}$
normal $\|\|z$	$xxz = xzx = yyz = yzy$ $zxx = zyy$ zzz

Table 3.1: Non-zero tensor elements of the nonlinear susceptibility tensor $\boldsymbol{\chi}^{(2)}$ for the (001) cubic surface. For simplicity, only indices are displayed.

The nonzero elements of tensor (3.2) are summarized in Table 3.1.

3.2 Surface magnetism and the SHG

The magnetization is influencing the nonlinear susceptibility tensor via the combination of a spin-orbit coupling and an exchange interaction [65, 67]. The spin-orbit coupling acts similarly to an external magnetic field. It changes the orbital momentum of the electron and thus rotates the polarization plane of the generated light. In nonferomagnetic materials, the effect cancels while both spin states are equally occupied. However, in ferromagnetic materials the exchange interaction splits the electronic bands in energy and the spin-up and spin-down states are not equally occupied. This implies that new non-zero terms of the nonlinear susceptibility tensor can arise. The magnitude of the original terms can be changed, as well.

The presence of magnetization vector $\boldsymbol{M}$ is not affecting the inversion symmetry of the material (since $\boldsymbol{M}$ is an axial vector). Therefore, the dipolar term in Eq. 3.1 is zero in bulk also for ferromagnetic materials. However, magnetization is lowering the symmetry of the surface. Therefore, new non-zero elements in the surface-generated nonlinear susceptibility tensor $\boldsymbol{\chi}^{(2)}$ are arising. These magnetization-induced elements are in the first approximation linearly dependent on the magnetization vector $\boldsymbol{M}$ and thus they are changing their sign when the magnetization is reversed. One can then write the nonlinear polarization in a dipolar approximation as

$$\boldsymbol{P}(2\omega, \pm\boldsymbol{M}) = \left(\boldsymbol{\chi}^{(2,\mathrm{even})} \pm \boldsymbol{\chi}^{(2,\mathrm{odd})}\right) \boldsymbol{E}(\omega)\boldsymbol{E}(\omega) \,, \tag{3.3}$$

where $\boldsymbol{\chi}^{(2,\mathrm{even})}$ is the part of the nonlinear susceptibility tensor even in magnetization and $\boldsymbol{\chi}^{(2,\mathrm{odd})}$ is the part of the tensor odd in magnetization.

The basic information about the nonlinear susceptibility tensor can be obtained from symmetry considerations. By applying symmetry transformations on the chosen system, one can easily determine which tensor elements of the susceptibility tensor should be

zero, and which should be odd or even in magnetization for individual configurations of $\boldsymbol{M}$ with respect to the sample surface and the incidence plane of the exciting light beam. In the longitudinal optical configuration (for the definition of the Cartesian coordinate system see Fig. 3.2) one gets

$$\boldsymbol{\chi}^{(2)}(\pm\boldsymbol{M}) = \left(\begin{array}{ccc|ccc} 0 & 0 & 0 & 0 & \chi_{xxz} & \pm\chi_{xxy} \\ \pm\chi_{yxx} & \pm\chi_{yyy} & \pm\chi_{yzz} & \chi_{yyz} & 0 & 0 \\ \chi_{zxx} & \chi_{zyy} & \chi_{zzz} & \pm\chi_{zyz} & 0 & 0 \end{array}\right) , \tag{3.4}$$

in the transverse configuration the tensor has a form

$$\boldsymbol{\chi}^{(2)}(\pm\boldsymbol{M}) = \left(\begin{array}{ccc|ccc} \pm\chi_{xxx} & \pm\chi_{xyy} & \pm\chi_{xzz} & 0 & \chi_{xxz} & 0 \\ 0 & 0 & 0 & \chi_{yyz} & 0 & \pm\chi_{yxy} \\ \chi_{zxx} & \chi_{zyy} & \chi_{zzz} & 0 & \pm\chi_{zxz} & 0 \end{array}\right) , \tag{3.5}$$

and in the polar configuration the tensor writes

$$\boldsymbol{\chi}^{(2)}(\pm\boldsymbol{M}) = \left(\begin{array}{ccc|ccc} 0 & 0 & 0 & \pm\chi_{xyz} & \chi_{xxz} & 0 \\ 0 & 0 & 0 & \chi_{yyz} & \pm\chi_{yxz} & 0 \\ \chi_{zxx} & \chi_{zyy} & \chi_{zzz} & 0 & 0 & \pm\chi_{zxy} \end{array}\right) . \tag{3.6}$$

In Table 3.2, the non-zero elements from (3.4), (3.5) and (3.6) are summarized, according to [68].

With help of Table 3.2 it is possible to suggest several methods for obtaining the magnetic SHG signal in various optical configurations. Let us assume that the magnetization is longitudinal. The optical plane of incidence is defined by the x and z axes of the Cartesian coordinate system in agreement with the notation in Table 3.2 (see also the schematic in Fig. 3.2). Then the basic experimental configurations are:[1]

s-in For the incident s-polarization (i.e. the electric field intensity vector $\boldsymbol{E}$ is in the y-direction, perpendicular to the plane of incidence), there are photons generated at the 2ω frequency which are p-polarized and also those which are s-polarized. The source component of the nonlinear susceptibility tensor giving the main p-polarized output is the χ_{zyy} tensor element even in $\boldsymbol{M}$. For the s-polarization there is also the χ_{yyy} tensor element odd in $\boldsymbol{M}$. The direct information about magnetization can be therefore obtained by measuring the intensity of the s-polarized 2ω light (s-in/s-out geometry) which usually provides very low signal levels.

[1] The correct quantitative analysis should also include the Fresnel reflection and transmission coefficients of the interfaces, as specified in the *surface sheet model* [69]. In the following text we will include these factors into the elements of the $\boldsymbol{\chi}$ tensor.

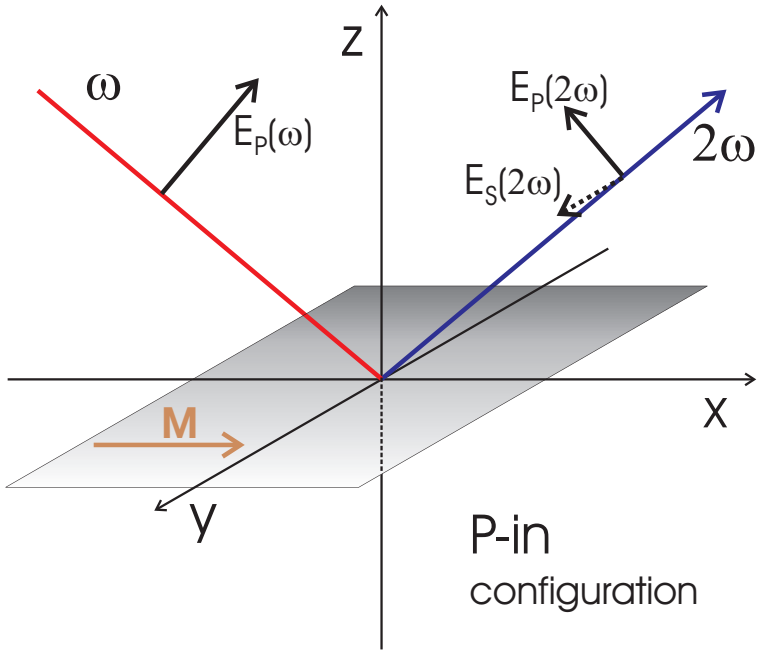

Figure 3.2: Definition of the coordinate system in the longitudinal geometry of the Magnetization-Induced Surface Second Harmonic Generation (MSSHG) experiment, a p-polarization is incident on the specimen surface.

normal $\|\|z$	Even in $\boldsymbol{M}$ ($\boldsymbol{\chi}^{(2,\text{even})}$)	Odd in $\boldsymbol{M}$ ($\boldsymbol{\chi}^{(2,\text{odd})}$)
Longitudinal $\boldsymbol{M}\|\|x$	$yzy = yyz$ $xzx = xxz$ zzz zyy zxx	$xyx = xxy$ $zyz = zzy$ yzz yyy yxx
Transverse $\boldsymbol{M}\|\|y$	$xxz = xzx$ $yyz = yzy$ zxx zyy zzz	$yxy = yyx$ $zxz = zzx$ xxx xyy xzz
Polar $\boldsymbol{M}\|\|z$	$xxz = xzx = yyz = yzy$ $zxx = zyy$ zzz	$xyz = xzy = -yxz = -yzx$ $zxy = zyx$

Table 3.2: Non-zero tensor elements of the nonlinear susceptibility tensor $\boldsymbol{\chi}^{(2)}$ for the (001) cubic surface in the presence of magnetization. The normal of the surface is parallel to the z axis. For simplicity, only indices of the tensor elements are displayed.

p-in For the incident p-polarization (the electric field intensity vector $\boldsymbol{E}$ is in the $x-z$ plane of incidence), there are generated photons at the 2ω frequency which are p-polarized and also s-polarized. The source components of the nonlinear susceptibility tensor responsible for the p-polarization output are the χ_{xxz}, χ_{zxx} and χ_{zzz} tensor elements even in $\boldsymbol{M}$, while for the s-polarization there are responsible the χ_{yzz} and χ_{yxx} tensor elements odd in $\boldsymbol{M}$. Therefore, an information about magnetization can be obtained also in this case by measuring the intensity of the s-polarized 2ω light (p-in/s-out geometry).

sp-in For the incident sp-polarization (the direction of $\boldsymbol{E}$ is by 45° shifted with respect to the incidence plane), a more complicated mixture of polarizations is generated. Either in the case of the detection of the p-polarized light or for the s-polarized light detection, the resulting signal is generated by a sum of magnetic and nonmagnetic tensor elements. In this case, it turns out to be useful to define the magnetic asymmetry as

$$\mathcal{A} = \frac{I(\boldsymbol{M}) - I(-\boldsymbol{M})}{I(\boldsymbol{M}) + I(-\boldsymbol{M})} \,, \tag{3.7}$$

where I is the intensity of the 2ω light detected for in the chosen experimental configuration. For the intensity magnitude, one can write

$$I(\pm\boldsymbol{M}) \propto |\chi_{\mathrm{eff}}^{(2,\mathrm{even})} \pm \chi_{\mathrm{eff}}^{(2,\mathrm{odd})}|^2 \tag{3.8}$$

where the effective nonmagnetic $\chi_{\mathrm{eff}}^{(2,\mathrm{even})}$ and magnetic $\chi_{\mathrm{eff}}^{(2,\mathrm{odd})}$ tensor elements are introduced as sums of respective non-zero tensor elements (including the Fresnel factors). The asymmetry is then given as

$$\mathcal{A} = \frac{2|\chi_{\mathrm{eff}}^{(2,\mathrm{even})}||\chi_{\mathrm{eff}}^{(2,\mathrm{odd})}|}{|\chi_{\mathrm{eff}}^{(2,\mathrm{even})}|^2 + |\chi_{\mathrm{eff}}^{(2,\mathrm{odd})}|^2} \cos(\varphi_{\mathrm{even}} - \varphi_{\mathrm{odd}}) \,. \tag{3.9}$$

Because the absolute values of the magnetic elements of the susceptibility tensor are usually much smaller than the nonmagnetic ones, one can simplify the equation (3.9) and obtain the term proportional to the tensor element odd in $\boldsymbol{M}$

$$\mathcal{A} \approx \frac{2|\chi_{\mathrm{eff}}^{(2,\mathrm{odd})}|}{|\chi_{\mathrm{eff}}^{(2,\mathrm{even})}|} \cos(\varphi_{\mathrm{even}} - \varphi_{\mathrm{odd}}) \,. \tag{3.10}$$

In the above given equations, the $\cos(\varphi_{\mathrm{even}} - \varphi_{\mathrm{odd}})$ term is arising due to the complex nature of the susceptibility tensor elements, i.e. due to their, in general, unequal phase.

The magnetic information is then obtained by means of the asymmetry value. The same approach as for the sp-in/p-out (or s-out) geometry can be applied to other geometries with are leading to a mixture of magnetic and nonmagnetic components in the output intensities, the p-in/sp-out geometry, for instance.

The above given review has shown several ways how to obtain the information about the surface magnetism by means of the Surface Second Harmonic Generation technique. Quantitative assumptions would be necessary to decide which configuration is giving for an individual surface the best signal-to-noise ratio. In a real experiment, the trial and failure approach gives usually the fastest answer to this issue.

3.3 Experimental approaches to the surface SHG

In this section, the Magnetization-Induced Surface Second Harmonic Generation (MSSHG) technique will be discussed from the experimental point of view. The recently used experimental approaches will be described with emphasis on the setup used in this work. The description of the method is similar for MSSHG and the (nonmagnetic) surface SHG, only the tool for magnetizing the sample is needed for MSSHG in addition.

Nonlinear optical effects are usually achieved by strong electromagnetic fields. The need of a source of strong electromagnetic fields is common for all the surface SHG methods described in following subsections. One of the most preferable excitation sources is a laser. Therefore, the nonlinear optics development is directly related to the advances of the laser technology. For the surface nonlinear optics, the intensities above $1\,\mathrm{MW{\cdot}cm^{-2}}$ are necessary. A continuous laser radiation cannot be used because any material would be immediately destroyed by such a high power. The technology of pulsed lasers is therefore needed. The shorter is the pulse width, the higher is the peak power. Therefore, the ultrashort femtosecond lasers are now preferable for experiments in nonlinear optics. The recent developments in high-repetition-rate mode-locked lasers (Sec. 1.3.1) improve considerably the experimental capabilities of the MSSHG methods.

3.3.1 General description of a surface SHG experiment

The principal schematic of a surface SHG experiment is sketched in Fig. 3.3. The laser system producing ultrashort pulses serves usually for the exciting optical beam generation. As in some experimental geometries the resulting signal is extremely sensitive to the proper polarization of the exciting beam, the setting of the polarization before the

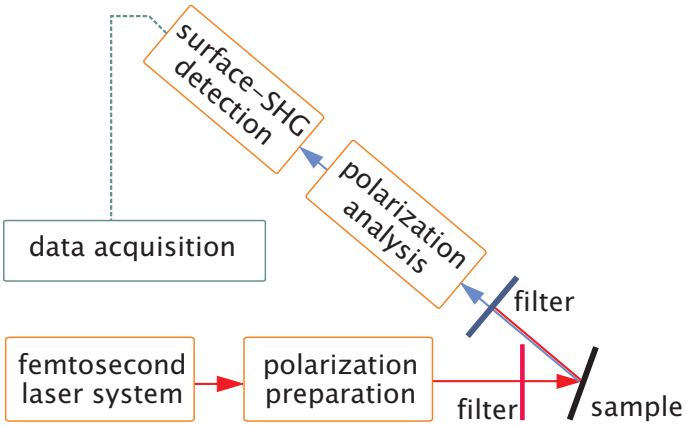

Figure 3.3: General schematic of the experimental setup used for surface SHG experiments.

beam impinges onto the sample has to be done with a high carefulness.

When the surface of the sample is not very reactive, it can be placed in air. However, if the sample surface is reactive or if the measurement during its growth is to be performed, special conditions are mandatory. In such a case, the sample can be located either in ultrahigh vacuum (UHV) conditions or in an electrochemical cell [70, 71]. The experiments in electrochemical cells allow to study the SHG response of the sample during the electrolytic process. In this way, the changes of the surface properties (roughness, chemical composition...) during the process can be observed. However, most of the experiments are nowadays performed under UHV conditions which are offering more versatile sample preparation and characterization procedures.

After the interaction with the sample the fundamental frequency has to be filtered out and the light at the 2ω frequency is detected. In most experimental configurations, the polarization of the detected 2ω light is selected by an analyzer and its intensity is measured afterwards by a photon counting photomultiplier.

3.3.2 Experimental setup — MSSHG in UHV

The experiments which were the objective of this work were dealing mainly with reactive metallic surfaces. The changes of magnetic properties during the layer-by layer growth were studied. Therefore, the employment of a UHV apparatus was necessary. The schematic description of the setup is displayed in Fig. 3.4.

The femtosecond laser system used for the production of ultrashort laser pulses was already described in Sec. 1.3.1. It is producing linearly polarized pulses at 800 nm. The typical pulse length is below 10 fs. The average power of the beam is about 1 W. The

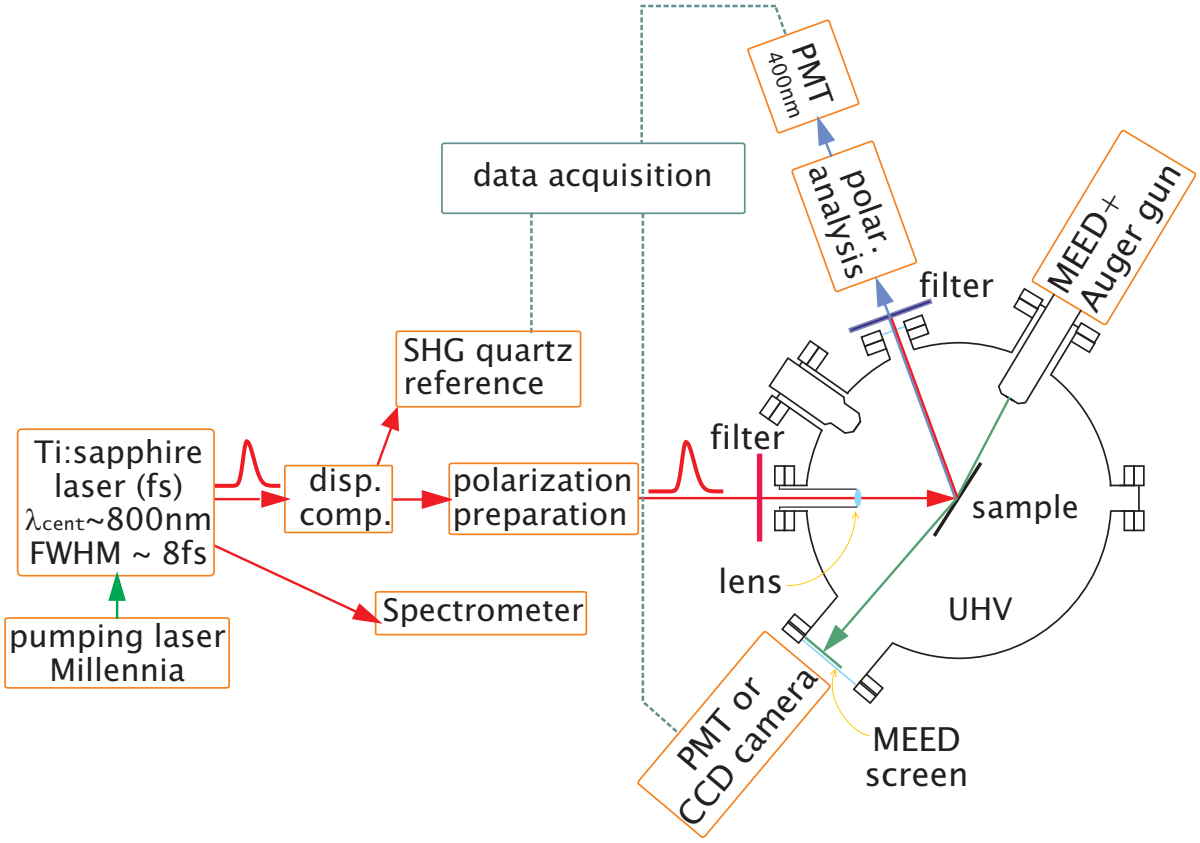

Figure 3.4: Schematic of the experimental setup used for Magnetization-Induced Surface Second Harmonic Generation (MSSHG) experiments.

corresponding energy of one pulse is $\approx 13\,\mathrm{nJ}$.

As the samples could be overheated by the full power from the laser, there was an option of inserting a chopper in the laser beam. For most of the measurements discussed in Chapter 4, about 10% of the power was used and the rest was rejected by the chopper blades. A complementary method avoiding overheating of one spot on the sample is consisting of a raster-scanning of the sample surface by the laser beam. One of the mirrors outside the chamber is mounted on a piezo-element which is allowing to change slightly the direction of the beam in two axes. By putting an AC signal on the piezo elements it is possible to scan the sample surface. The area of the sample scanned in this way is about $60\,\mu\mathrm{m}\times 60\,\mu\mathrm{m}$. The frequencies $10\,\mathrm{Hz}<f<100\,\mathrm{Hz}$ were used for the scan.

For the quantitative interpretation of the MSSHG experiments, it is necessary to normalize the obtained SHG intensities. Unluckily, the SHG yield is not directly proportional to the exciting beam intensity, as the pulse width (and the related peak power) is not absolutely stable during the experiment. Broadening of the pulse is causing a de-

crease of the SHG yield even when the 800 nm light intensity stays constant. Therefore, a measurement of the exciting light intensity cannot be used as a reference. For the correct normalization of the obtained results, a reference SHG channel has to be used. A part of the beam is selected by a beam splitter and sent through a quartz crystal. The intensity of the generated 400 nm light is measured by a photomultiplier operating in an analogue mode. This signal gives a correct normalization to the SHG generated on the sample in the UHV chamber.

Before entering the chamber, the beam is passing through the part of the setup which is used to set its polarization. Using of a prism polarizer would cause broadening of the pulse (and therefore also decrease of the peak power) due to the dispersion. Therefore, one has to use phase plates for polarization manipulation. One $\lambda/2$ achromatic phase plate is used to rotate the polarization direction in this case. A filter is used as the last optical element before the pulse enters the UHV chamber to reject the 400 nm light which is created while passing through preceding optical elements. This 400 nm light would otherwise create high background to the SHG signal generated from the surface of the sample in the UHV chamber.

The UHV chamber itself, the sample holder, the coil used for magnetizing the sample and the MBE evaporators were described already in Sec. 1.3.3. The Medium-Energy Electron Diffraction (MEED) is serving not only for an adjustment of the orientation of the crystallographic axes of the sample, but also for monitoring of the growth of the thin films on the sample surface [72]. The MEED pattern can be recorded by a 15-bit water-cooled CCD camera (Hamamatsu Inc.) allowing also a quantitative analysis of the intensity of the diffraction spots. However, for monitoring of the specular beam intensity during the experiment a photomultiplier working in an analogue mode is used, as it is providing the desired signal without additional data treatment (needed for the camera data).

The choice of the angle of incidence is constrained by the chamber geometry — it is 43° for most of the MSSHG experiments. After the beam leaves the chamber by the output viewport, the 800 nm component of the beam is filtered out and only the SHG signal at 400 nm remains. By a Glan-Thompson analyzer it is possible to chose the polarization of the SHG light desired for the detection. Photons which pass through the analyzer are detected by a photomultiplier (from the Perkin-Elmer Optoelectronics company) in the photon-counting mode.

The data acquisition and the controlling of the experiment is provided with a help of a personal computer, for details see Sec. 1.3.4.

In this chapter, the theoretical background of the Magnetization-Induced Surface

Second Harmonic Generation (MSSHG) technique was summarized. The experimental approaches were described with emphasis on the arrangement used for the experiments discussed in the following chapter.

Chapter 4

Experimental study of the O/Fe/MgO system by MSSHG

In this chapter, typical experimental results obtained by the Magnetization-Induced Surface Second Harmonic Generation (MSSHG) technique will be presented. The magnetic properties of the surface in the p(1×1)O/Fe/MgO(001) system were studied. A complete data treatment leading to a quantitative information about the surface magnetism will be presented. The result will be compared with another method, i.e. the Spin Polarized Metastable Deexcitation Spectroscopy (SPMDS), used for the analysis of the surface magnetization.

4.1 Contradictory results of MSSHG and SPMDS

The previous experimental studies which have motivated the MSSHG investigations described in this work are summarized in this section.

It is well established that atoms placed on the surface in some less coordinated positions, for instance step edges of an uncompleted layer during the epitaxial growth, have different magnetic properties from those in bulk or in a complete surface layer. However, theoretical quantitative studies give somewhat contradictory results [73–75].

Up to now, there were two experimental works dealing with this phenomenon — a study of layer-by-layer growth of fcc Co films on Cu(001) surface by Magnetization-Induced Surface Second Harmonic Generation (MSSHG) [76, 77] and a study of surfactant-aided growth of Fe on p(1×1)O/Fe(001) surface (for details about the structure see Sec. 4.2) by Spin Polarized Metastable Deexcitation Spectroscopy (SPMDS) [78]. These experiments are, however, not giving the same result. Both of them are showing oscil-

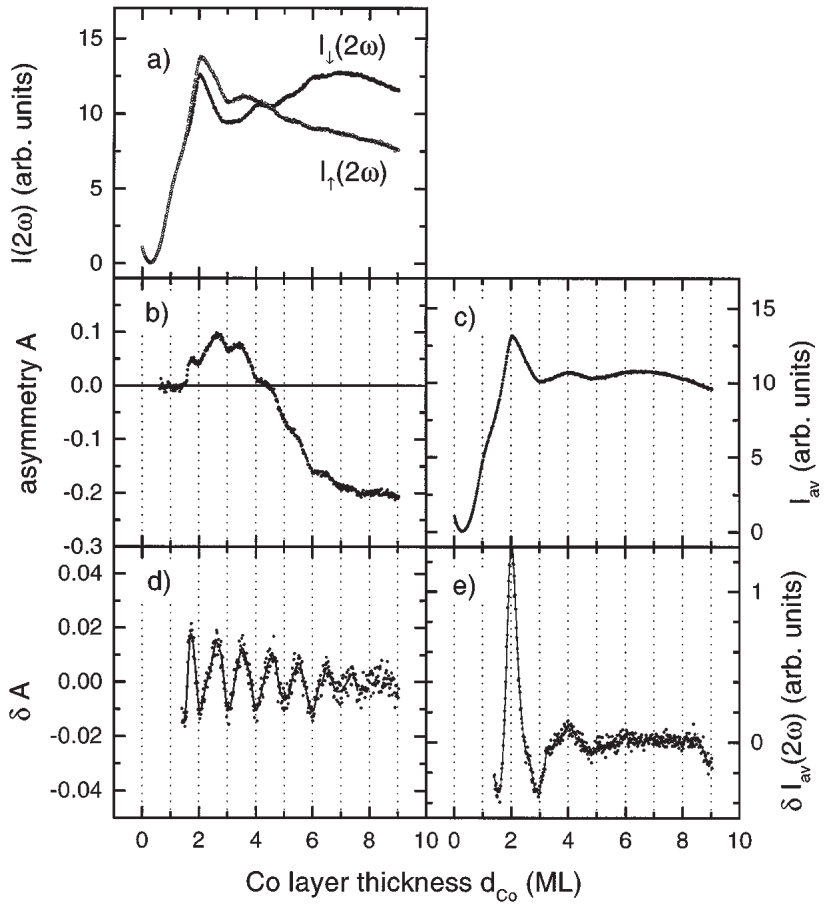

Figure 4.1: Experimental results of Jin at al. [76]. (a) Measured total SH intensity as a function of the Co film thickness for s-polarized incident light in the transversal Kerr geometry for the magnetization in opposite directions. (b) Magnetic asymmetry and (c) average SH intensity calculated from the SH intensities in (a). In (d) the difference of the magnetic asymmetry and its running average over 50 points is plotted. In (e) the similar difference as in (d) is plotted for the average SH intensity I_{av}

latory behavior of the magnetic signal with a period of one monolayer, but for Co on Cu(001) minima of the magnetic signal were observed for completed Co layers (the panel (d) in Fig. 4.1) while for Fe on p(1×1)O/Fe(001) maxima were observed for completed layers (the left panel of Fig. 4.2). Then there arises a question whether this incoherence is because of different nature of studied systems or because the experimental methods were used in some oversimplified way.

The aim of this chapter is to identify the origin of the difference between the MSSHG and the SPMDS results. Therefore, an experiment on the p(1×1)O/Fe(001) system was performed with use of the MSSHG method to find the origin of this different behavior.

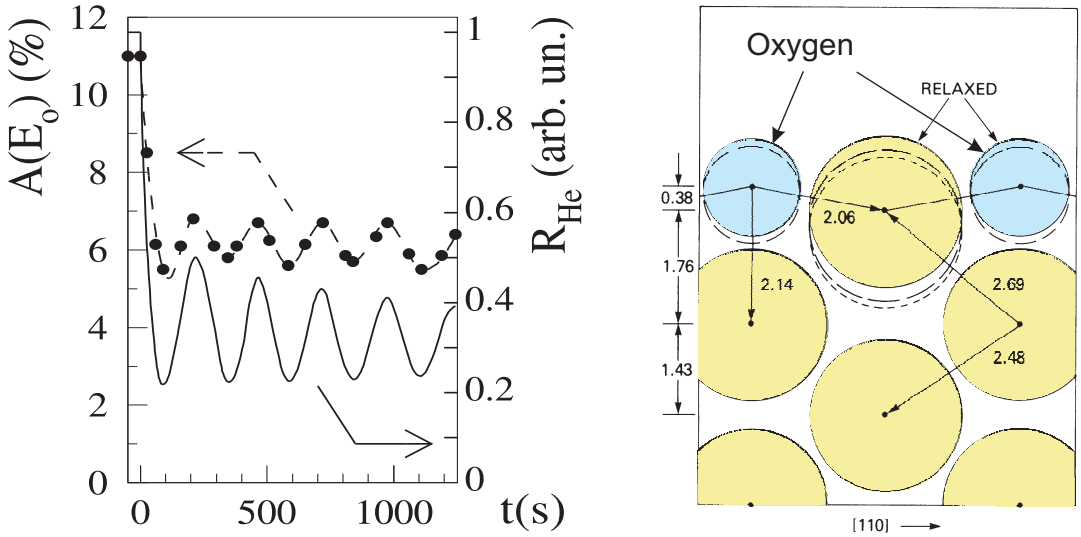

Figure 4.2: Left panel: Experimental results of Bisio et al. [78] obtained for Fe growth on p(1×1)O/Fe(001) at room temperature. He reflectivity (R_{He}, continuous line) and SPMDS asymmetry $A(E_0)$ at $E_0 \simeq 11.5\,\mathrm{eV}$ (dots) as a function of deposition time are displayed. The dashed line serves as a guide to the eye. Right panel: The geometry of p(1×1)O/Fe/MgO(001) system predicted by Chubb and Pickett [79].

4.2 p(1×1)O/Fe/MgO(001) system studied by MSSHG

In this section, the experimental results obtained by the MSSHG technique applied to the p(1×1)O/Fe/MgO(001) system will be presented. Firstly, the p(1×1)O/Fe/MgO(001) system and its preparation will be described. Then the experimental results in various optical geometries will be presented. At the end, the findings will be compared with the Spin Polarized Metastable Deexcitation Spectroscopy (SPMDS) results.

4.2.1 The p(1×1)O/Fe/MgO(001) system

The p(1×1)O/Fe/MgO(001) system is a model system for the adsorbate–metal interaction studies. At the surface of Fe(001), strong covalent bonds between the Fe and O atoms form a chemically stable FeO monolayer. The prediction of the bond lengths at the relaxed surface was calculated by Chub and Pickett [79], as shown in the right panel of Fig. 4.2. While depositing additional Fe layers, the FeO monolayer is floating at the top of the system and the oxygen monolayer is acting as a surfactant promoting epitaxial layer-by-layer growth [80]. After finishing an experiment, the sample surface can be

easily renewed by annealing at 600°C. The oxygen atoms which were buried under the Fe layer during the deposition are moved back to the location at the surface during the annealing procedure.

The p(1×1)O/Fe/MgO(001) system is for the experiments prepared as follows. The MgO(001) substrate is polished, annealed in O_2 and after loading to the UHV chamber is it flashed at 950 K. The Fe/MgO(001) system is one of a few metal-insulator systems which grow layer-by-layer under certain conditions [81, 82]. After *in situ* epitaxial growth of a single crystal Fe film on a clean MgO(001) substrate at a pressure below 10^{-10} mbar and by subsequent annealing at 870 K, a clean and ordered Fe(001) surface is obtained. During the deposition, the temperature is risen from 300 K to 420 K to promote the epitaxial growth. The resulting Fe width is ≈50 nm. The surface quality is checked by Medium-Energy Electron Diffraction (MEED). Afterwards the Fe(001) surface is exposed to ≈20 L O_2 (1 L = 10^{-6} Torr·s) and it is annealed at 870 K for 30 min. This results in a formation of the p(1×1) oxygen adlayer on the Fe(001) surface.

The MSSHG experiments motivated by the inconsistency of previous MSSHG and SPMDS results described in Sec. 4.1 are performed during in situ epitaxial growth of additional Fe layers onto the p(1×1)O/Fe/MgO(001) specimen. The growth is monitored by MEED. The comparison with the growth of iron layers on the clean Fe/MgO(001) surface (without oxygen) can be seen in Fig. 4.3. The surfactant effect of oxygen is obvious, multiple layers can be grown on the sample without large dumping of the MEED oscillations. This is in contrast with growth of Fe on the Fe/MgO(001) system, where the three-dimensional growth is dominating.

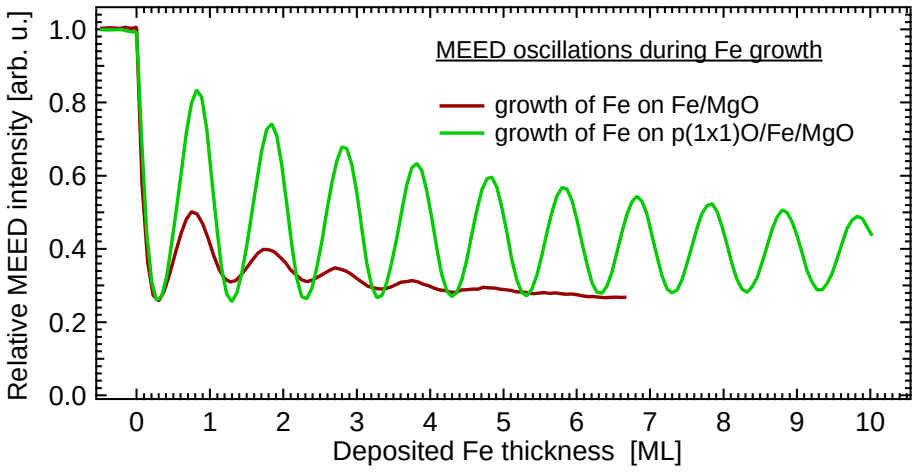

Figure 4.3: Oscillations of the intensity of the specular MEED spot during the Fe growth on Fe/MgO(001) and p(1×1)O/Fe/MgO(001) systems at 310 K.

4.2.2 Results of the MSSHG experiments

The MSSHG experiments on the p(1×1)O/Fe/MgO(001) system were performed with the apparatus described in Sec. 3.3.2 (Fig. 3.4). For the preparation of Fe layers, a MBE evaporator was used. During the data acquisition, the evaporator was shut down, so that no light emitted from the hot Fe source could influence the optical measurement.

First, an experiment for determination of the magnitude of the SHG signal was performed. One monolayer of Fe was grown onto the p(1×1)O/Fe/MgO(001) system and afterwards the MSSHG was measured for incident p-polarization. The orientation of the analyzer was gradually changed in 12° steps so that the MSSHG signal and the magnetic asymmetry could be observed for varying polarization of the detected light. This helps in choosing the best experimental geometry for experiments performed during the Fe layer growth.

The results of this experiment are shown in Fig. 4.4. Important experimental setting is the p-in/s-out configuration, as mentioned in Sec. 3.2. The SHG signal is very low in this case. However, it is of solely magnetic origin, therefore this configuration is preferable for studies of the surface magnetism. It will be chosen as one of the experimental configurations used for the MSSHG studies of the p(1×1)O/Fe/MgO(001) system during the epitaxial growth of the Fe layer. This will be described in the following part of this section.

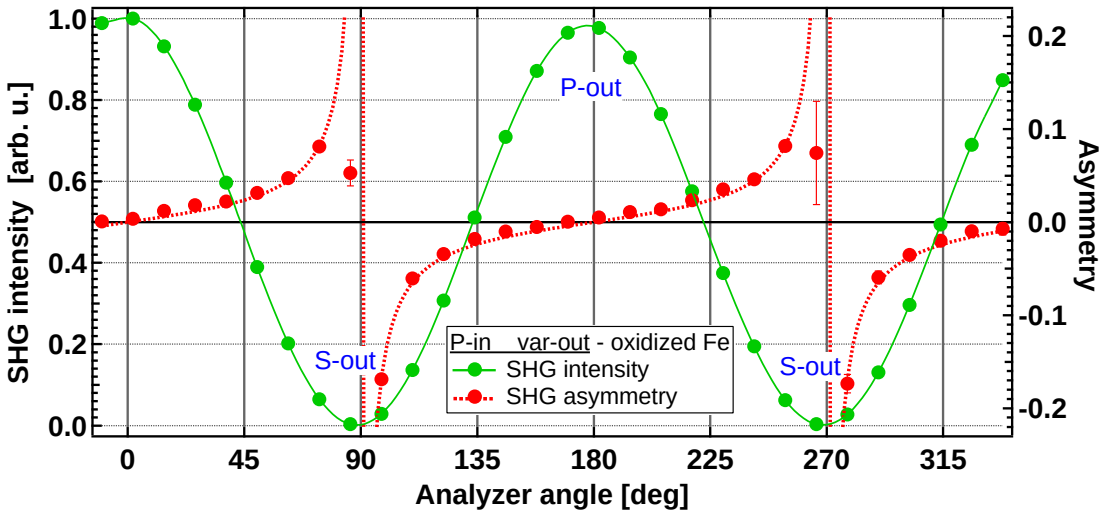

Figure 4.4: The SHG intensity (average of $I(\boldsymbol{M})$ and $I(-\boldsymbol{M})$) and the MSSHG asymmetry for the p-in excitation and rotating analyzer. Analyzer angles corresponding to p-out and s-out settings are pointed up.

p-in/s-out geometry

As stated above, the p-in/s-out experimental geometry gives the information about the surface magnetization in a straightforward way. The intensity of the measured second harmonic signal is directly proportional to the effective sum of the "magnetic" tensor elements χ_{yzz} and χ_{yxx} which are linearly dependent on the magnetization. The experimentally obtained normalized SHG intensities during the epitaxial growth of the Fe layer on the p(1×1)O/Fe/MgO(001) system are displayed in Fig. 4.5. The measurement time was 40 minutes per one point in this case. The SHG intensity in the beginning of the Fe deposition was chosen as the reference.

The measured SHG intensity exhibits an initial drop to about 57% of its starting value when depositing the first 0.5 monolayer of Fe. Later, it displays clear one-monolayer periodic oscillations with maxima corresponding to full monolayer completion.

When we indicate the effective sum of the magnetic tensor elements involved as $\chi_{\mathrm{eff}}^{(2,\mathrm{odd})}$, then for the intensity of the detected SHG signal one can write

$$I_{\mathrm{P-in,S-out}} \propto |\chi_{\mathrm{eff}}^{(2,\mathrm{odd})}|^2 \ . \tag{4.1}$$

From this equation it follows that the effective magnetic tensor element oscillates with the same phase as the measured MSSHG intensity. This already gives an answer to the issue addressed in Sec. 4.1. However, the experiment in another geometric configuration

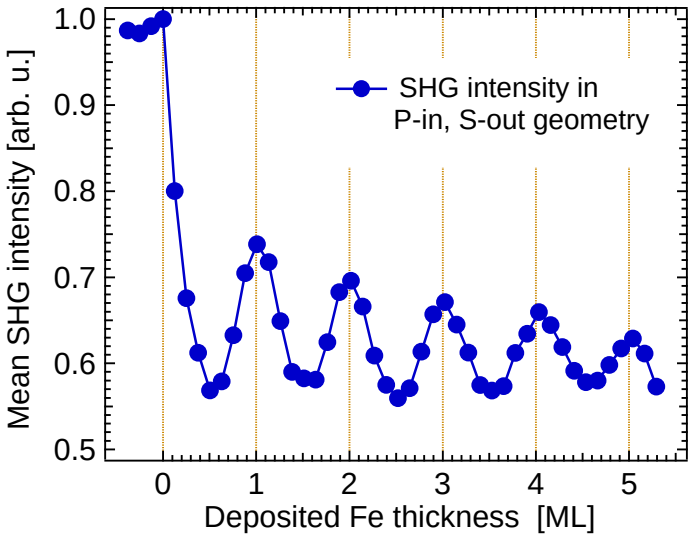

Figure 4.5: SHG measurements during the Fe growth on the p(1×1)O/Fe/MgO(001) system. The normalized SHG intensity (average of $I(\boldsymbol{M})$ and $I(-\boldsymbol{M})$) for the p-in/s-out geometry is displayed. The signal oscillates with the one monolayer period.

was performed to justify the result.

sp-in/s-out geometry

In the sp-in/s-out geometry, a mixture of magnetic tensor elements (χ_{yzz}, χ_{yxx} and χ_{yyy}) and one nonmagnetic element χ_{yyz} is generating the SHG signal. For the determination of magnetic properties of the sample, the magnetic asymmetry should be obtained during the experiment and the SHG intensity as well (see Sec. 3.2).

The experimental curves for the SHG intensity $I_{\mathrm{SP-in,S-out}} = (I_{\mathrm{SP-in,S-out}}(\boldsymbol{M}) + I_{\mathrm{SP-in,S-out}}(-\boldsymbol{M}))/2$ and the asymmetry $\mathcal{A}_{\mathrm{SP-in,S-out}}$ are plotted in Fig. 4.6. Both the intensity and the asymmetry show oscillations with one-monolayer periodicity. The measurement time was also 40 minutes per one point in this case.

The asymmetry for this experimental configuration can be expressed by Eq. 3.10:

$$\mathcal{A}_{\mathrm{SP-in,S-out}} \approx \frac{2|\chi_{\mathrm{eff}}^{(2,\mathrm{odd})}|}{|\chi_{\mathrm{eff}}^{(2,\mathrm{even})}|} \cos(\varphi_{\mathrm{even}} - \varphi_{\mathrm{odd}}) \ . \tag{4.2}$$

The intensity (see also Eq. 3.8) is proportional to the square of the nonmagnetic tensor element $\chi_{\mathrm{eff}}^{(2,\mathrm{even})}$, the magnetic tensor elements are negligible compared to the nonmagnetic ones:

$$I_{\mathrm{SP-in,S-out}} \propto |\chi_{\mathrm{eff}}^{(2,\mathrm{even})}|^2 \ . \tag{4.3}$$

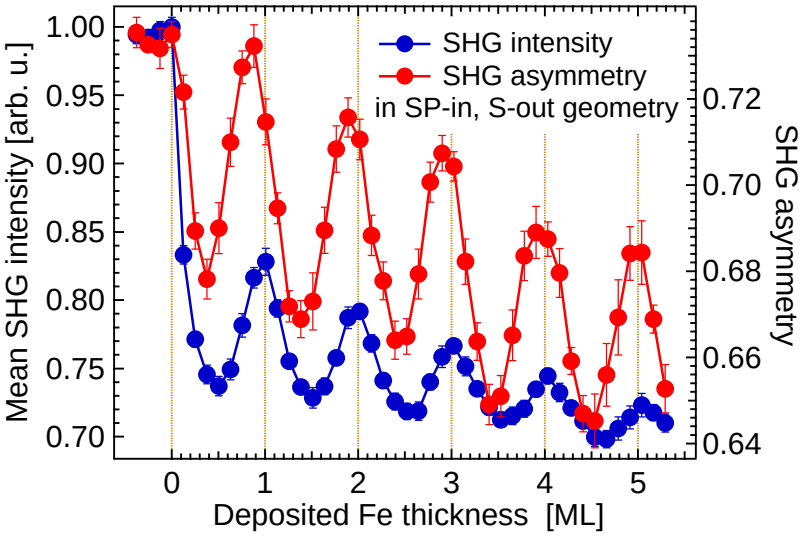

Figure 4.6: SHG measurements during the Fe growth on the p(1×1)O/Fe/MgO(001) system. The normalized SHG intensity (average of $I(\boldsymbol{M})$ and $I(-\boldsymbol{M})$) and the asymmetry for the sp-in/s-out geometry are displayed. The signal oscillates with the one monolayer period.

The calculation of the effective magnetic tensor element from the experimental data is then straightforward, as will be seen in the following.

Magnetic signal separation

For both experimental configurations mentioned above, the effective magnetic tensor element $\chi_{\mathrm{eff}}^{(2,\mathrm{odd})}$ can be extracted from the experimental data. The effective magnetic tensor element is proportional to the magnetization magnitude. Therefore, it gives a direct measure of the surface magnetization during the epitaxial growth of the Fe layer. As the extraction of absolute values of the tensor elements is not possible, all the results are normalized to the value in the beginning of the Fe deposition.

In the case of **p-in/s-out** geometry, the calculation of $\chi_{\mathrm{eff}}^{(2,\mathrm{odd})}$ is straightforward. From Eq. 4.1 one obtains immediately

$$|\chi_{\mathrm{eff}}^{(2,\mathrm{odd})}| \propto \sqrt{I_{\mathrm{P-in,S-out}}} \ . \tag{4.4}$$

For the **sp-in/s-out** geometry, the combination of Eq. 4.2 and Eq. 4.3 leads to

$$|\chi_{\mathrm{eff}}^{(2,\mathrm{odd})}| \propto \sqrt{I_{\mathrm{SP-in,S-out}}} \cdot \mathcal{A}_{\mathrm{SP-in,S-out}} \ . \tag{4.5}$$

Here the assumption of a constant phase difference $\varphi_{\mathrm{even}} - \varphi_{\mathrm{odd}}$ was applied.

Results provided by equations (4.4) and (4.5) are displayed in Fig. 4.7. As the results are matching very well, one can say that the assumption of constant phase difference was correct in this case and possible error was below the experimental resolution. Also the fact that in the case of the sp-in/s-out configuration is in $\chi_{\mathrm{eff}}^{(2,\mathrm{odd})}$ the χ_{yyy} element included in addition doesn't seem to play an important role, this tensor element will be negligible in comparison to χ_{yzz} and χ_{yxx}.

Similar oscillatory behavior of the effective magnetic tensor element $\chi_{\mathrm{eff}}^{(2,\mathrm{odd})}$ was obtained also in the p-in/sp-out and sp-in/p-out geometry. Another experiments were carried out at 400 nm fundamental wavelength. They were providing almost identical results as well.

From the results presented in this section, it can be concluded that the magnetic contribution to the SHG for the p(1×1)O/Fe/MgO(001) system during the deposition of additional Fe layers exhibit local maxima for completed monolayers.

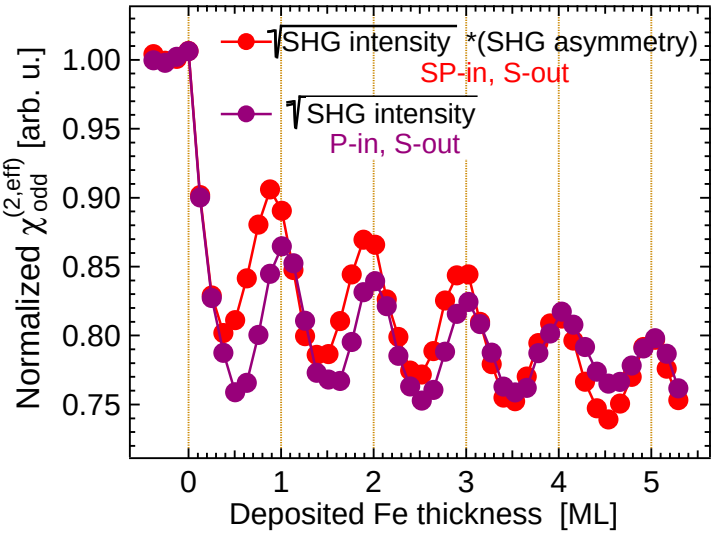

Figure 4.7: Calculated effective magnetic tensor element of the susceptibility tensor from measurements in p-in/s-out geometry and sp-in/s-out geometry as well. The results were normalized to their starting value for zero Fe-coverage. The source data are displayed in Fig. 4.5 and Fig. 4.6.

4.2.3 Conclusion and comparison of the O/Fe/MgO and Co/Cu systems

The above described study gives an answer to the problem addressed in Sec. 4.1. The question was whether the surface magnetization of the p(1×1)O/Fe/MgO(001) and Co/Cu(001) systems is behaving differently during the epitaxial growth of the top magnetic layer or whether the applied experimental techniques (SPMDS resp. MSSHG) provide different physical quantities.

By comparing the results obtained on the p(1×1)O/Fe/MgO(001) system displayed in Fig. 4.7 and results obtained by Bisio et al. [78] (the left panel of Fig 4.2), one can easily conclude that the results are fully compatible showing the maxima of the magnetic signal for full monolayer coverage. Therefore, it can be concluded that both Magnetization-Induced Surface Second Harmonic Generation (MSSHG) and the Spin Polarized Metastable Deexcitation Spectroscopy (SPMDS), despite completely different physical mechanisms, provide compatible results even in the sub-monolayer range. The surface magnetic response of the p(1×1)O/Fe/MgO(001) and Co/Cu(001) systems is different probably due to surface relaxation and other effects caused by the oxygen adlayer in the p(1×1)O/Fe/MgO(001) system and also by contributions of two interfaces in the Co/Cu(001) system.

Besides the initial drop, the relative magnitude of the magnetic signal oscillations (as displayed in Fig. 4.7) is of the order of 15% to 20%. This is much more than values expected in the case when only magnetic moments of the edge atoms are involved. The key-role in determining the observed oscillations must be therefore played by the characteristics of the O-Fe bonds within the surface Fe layer. As a confirmation of this hypothesis the same SHG experiments were performed during the Fe deposition on the clean Fe(001) surface (without oxygen). No oscillations of the SHG signal were observed, despite few damped, but still well resolved, oscillations of the MEED signal (see Fig. 4.3).

The ab-initio calculations [79] predict about 23% increase of the surface-to-subsurface bond length and a large sensitivity of the surface Fe magnetic moment upon the O-Fe geometry [83]. The enhancements of the top layer Fe magnetic moments from 10% to 15% with respect to clean Fe(001) surface were predicted. Recent studies show that even for homoepitaxial growth a considerable strains are induced between the islands and the layer underneath [84]. It is plausible to expect that a creation of islands is resulting in decrease of the magnetic moments, as it is breaking the ideal surface structure and thus decreasing the surface relaxation. This would agree with the observations reported in this chapter. However, the exact mechanism of the oscillatory behavior of the surface magnetization in the p(1×1)O/Fe/MgO(001) system is an open issue for future theoretical studies.

In conclusion, in this chapter the study of the surface magnetism by the Magnetization-Induced Surface Second Harmonic Generation method was reported. To our knowledge, it was for the first time the thin film magnetism during its growth was studied by using the p-in/s-out longitudinal geometry. This brings advantage of purely magnetic origin of the observed SHG intensity. Also results in other experimental geometries which are mixing the magnetic and nonmagnetic SHG response were coherent with the p-in/s-out SHG experiment. All the experiments were showing clearly one-monolayer periodic oscillations of surface magnetic response with local maxima for completed layers. This is in agreement with the previous SPMDS observations [78].

Chapter 5

Ultrafast electron dynamics

In many physical phenomena the excitation and relaxation of electrons in solid state materials plays an important role. The electron dynamics has to be taken into account when dealing with interactions of molecules with surfaces, surface "femtochemistry", optical processing of surfaces, magneto-optical recording, surface phase transitions, electrical charge and heat transport and with other phenomena.

Of high importance are also studies of spin-dependent lifetimes in ferromagnets, because there is a direct link to the applications in the data-recording industry. From the relaxation of hot electrons in ferromagnets one can learn about the decay of transient magnetization and about spin-selective transport and tunneling.

In this chapter, the issue of experimental methods feasible for studies of the ultrafast electron dynamics will be therefore addressed. A simple theoretical model for explanation of the experimental results will be shown as well.

5.1 Experimental methods for measurements of the ultrafast electron dynamics

For understanding the fundamentals of the electron dynamics in metals, the knowledge of the lifetimes and decay mechanisms for hot electrons is necessary. By "hot electrons" we mean the bound electrons excited above the Fermi level. The theory of electron scattering in metals was first formulated by Drude [85]. There exist several classical methods to measure the lifetimes of these hot electrons: the optical conductivity measurements [86–88], the transport measurements of thermal electrons at the Fermi surface [89, 90] and ballistic transport studies of hot electrons injected into metal from the vacuum or from

an interface with another material [91–93].

Basic information about the lifetimes of the hot electrons can be obtained also by measuring the width of spectroscopic resonance features by means of the inverse photoemission [12, 94], for instance. The width of the spectroscopic line Γ is given by the sum of elastic and inelastic scattering processes through the uncertainty relation

$$\Gamma \cdot \tau = 660\,\mathrm{meV}\cdot\mathrm{fs}\ , \tag{5.1}$$

where the average time between the phase-breaking scattering events is denoted as τ. Other spectroscopic techniques are using the high-resolution soft X-ray spectroscopy for studies of Auger resonant Raman intensities [95, 96] which is also accessing the field of femtosecond dynamics of adsorbate-substrate charge transfer processes.

Recently, a novel approach to measure the lifetimes of hot surface state and surface resonance electrons with use of a 4 K scanning tunneling microscope (STM) was given by Bürgi et al. [97].

In this work, we will focuss on the time resolved two-photon photoemission spectroscopy which is allowing in its pump-probe modification to perform highly resolved investigations of the electron dynamics at surfaces [8, 38].

5.2 Experimental apparatus for time-resolved two-photon photoemission

In this section, the experimental setup used by us for the time-resolved studies will be described. Most of the parts of the setup were already mentioned in previous chapters. Therefore, we will mainly focus on the improvements providing the time-resolution.

The principle of the time-resolved two-photon photoemission (TR-2PP) is sketched in Fig. 5.1. An ultrafast femtosecond laser pulse is exciting the electrons from the states below the Fermi level E_F to unoccupied states above the E_F and below the vacuum level E_{vac} (part 1 of Fig. 5.1). The other (probe) pulse is coming with a delay τ. During the delay between the pump and the probe pulses, the electron can either decay back from the excited state or it can stay at the excited level (depending on its lifetime and on the length of the delay τ). When the delay τ is short enough with respect to the lifetime of the hot electron, the photoelectrons can be detected (part 3a of Fig. 5.1).

As both the pump and the probe pulses are consisting of many photons, it should be pointed out that the two-photon photoemission signal can be generated also by excitation by two photons from the pump pulse or by two photons from the probe pulse. This

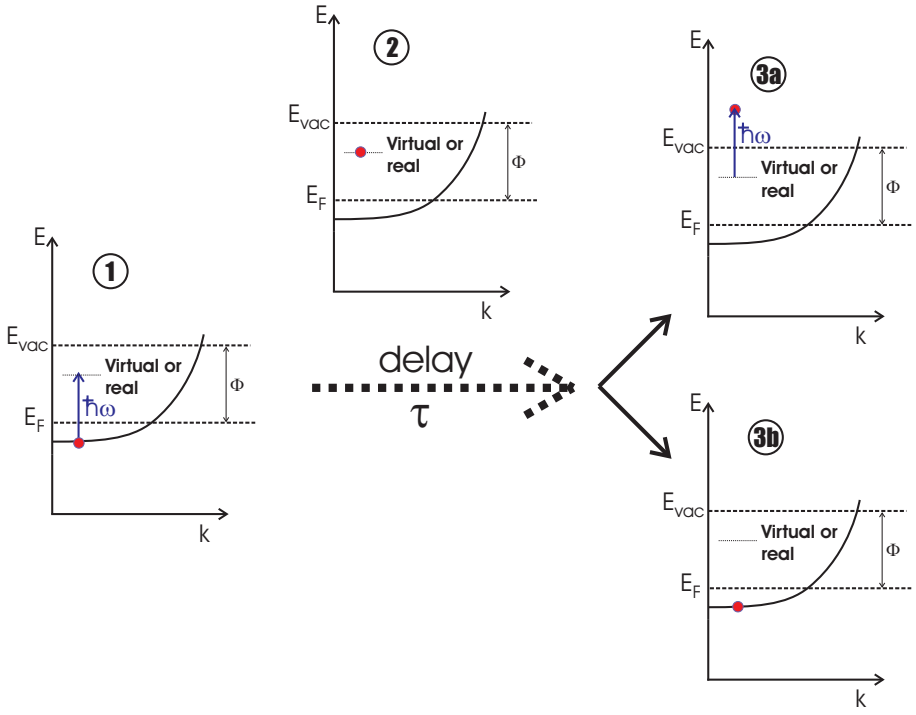

Figure 5.1: Principle of the time-resolved two-photon photoemission. 1: The electron from below the Fermi level is lifted by the first photon to an unoccupied state below the vacuum level. 2: During the delay between the pump and the probe pulse the electron can decay back from the excited state or stay in this state, depending on its lifetime and on the delay length τ. 3a + 3b: When the delay τ is short enough, the probe pulse is exciting the hot electron to the vacuum state and it can be detected.

contribution to the 2PP signal is, however, independent on the delay τ and therefore it can be easily identified when evaluating the results of the TR-2PP experiment.

The energy of the exciting fs-pulses should be well below the vacuum energy E_{vac} (measured with respect to E_F), so that the one photon photoemission is not possible (i.e. $\hbar\omega < E_{\mathrm{vac}} - E_F$). Otherwise the 2PP signal would not be resolved, because the 1PP intensities are much higher. On the other hand, the energy of the photons should be high enough to allow the excitation from the ground state to the vacuum level by two photons. It means that the $2\hbar\omega > E_{\mathrm{vac}} - E_F$ condition should be fulfilled.

The experimental arrangement used for the time-resolved 2PP experiments is displayed in Fig. 5.2. Most of its parts have been already described in Section 1.3 dealing with the two-photon photoemission, therefore only the differences necessary for the time-resolved measurements will be given here in detail.

The home-built fs-laser system and the frequency doubling stage attached are pro-

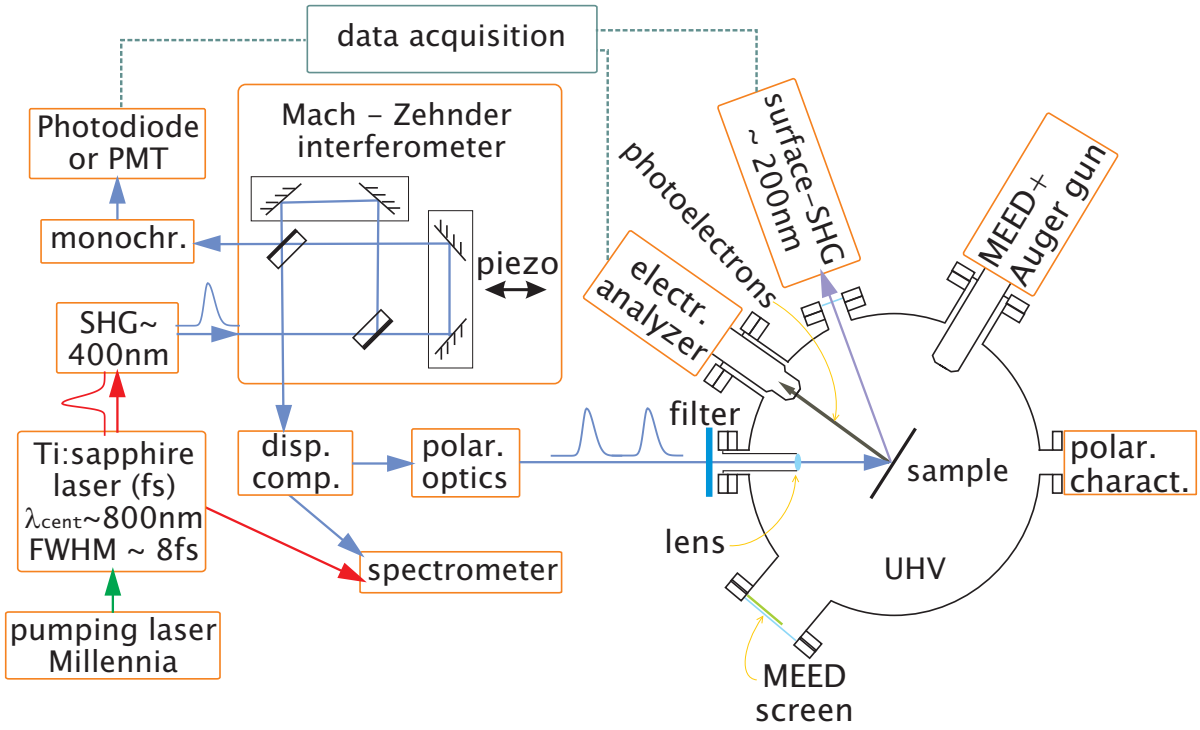

Figure 5.2: Schematic of the experimental setup used for time-resolved photoemission experiments.

ducing femtosecond laser pulses at 400 nm with a length well below 20 fs (see Sec. 1.3.2). After the frequency doubling stage, the beam is entering the Mach-Zehnder interferometer which is splitting the pulse into two parts and which allows to introduce a delay τ of one part of the beam by moving the appropriate arm of the interferometer. The use of the Mach-Zehnder interferometer allows to keep the pump and the probe pulses collinear, so that they can interfere. This is important for obtaining the information about the coherence decay of the hot electrons (see Sec. 5.3).

As 1 fs delay is corresponding to a shift of the arm of the interferometer by 0.3 μm, the high-stability piezoelectrically actuated stage (Piezosystem Jena GmbH) has to be used to position the arm of the interferometer if the sub-fs resolution is desired. The Mach-Zehnder interferometer was machined from stainless steel and the moving stage of titanium to achieve high thermal stability of the system. The laboratory was air-conditioned in addition, because also other parts of the experiment are temperature-sensitive. The stability of the interferometer was further improved by the fact that the interferometric optical table (by Newport Inc.), the laser was mounted on, was chosen to effectively damp the vibrations. Its thickness is 45 cm and it is placed on pneumatic

isolators I2000 with automatic leveling in addition. The interferometer is located in a semi-sealed box to avoid spoiling of the surfaces of the beam splitters and mirrors by dust particles.

As can be seen in Fig. 5.2, there are two outputting beams from the Mach-Zehnder interferometer. One is used for the excitation of the sample surface (the signal output). The other one is monochromatized (at 400 nm) and its intensity is measured as a reference signal to monitor the delay (the reference output). Key property of the Mach-Zehnder interferometer is that one of the two interfering beams is having the phase shifted by $\lambda/2$ in the case of the reference output compared to the case of signal output. Therefore, when a constructive interference in the signal output is observed, in the reference output there is a destructive interference occurring.

The experiment can be usually conducted in two ways. One way is to detect the complete photoelectron spectra at discrete values of the delay τ. The other way is to choose discrete values of the energy for the detected photoelectrons and scan the whole available range of the delay τ for each of these values.

When the constant-delay mode of operation is chosen, the interferometer should be set so that there is a constructive interference in the signal beam. This setting can be achieved by minimizing the signal from the reference measurement diode. To be able to measure over extended time periods (hours), the piezo positioning of the interferometer arm is controlled through a lock-in feedback by the signal from the diode measuring the reference beam intensity. To enable the lock-in detection, a small AC voltage (at $\approx$2 kHz) has to be added to the voltage controlling the piezo position.

However, in this chapter, we will deal with the other mode of operation of the interferometer only. It serves for acquiring photoemission and SHG data at continuously varying delays τ, so that the complete interferogram can be constructed. The energy of detected photoelectrons is kept constant during this experiment. In this case, the feedback control of the piezo position is switched off and a voltage ramp from an Agilent 33120A function generator is applied instead. The voltage ramp is displayed in Fig. 5.3. It is applied periodically with a ≈ 2 Hz frequency. The data acquisition was synchronized by a trigger signal at the start of the ramp. The range in which the data were recorded is indicated in the figure. By changing the amplitude of the ramp the range of the delays between the pulses can be modified, the maximum range allowed by the piezo actuator was $\pm$130 fs. Prior to applying it on the piezo, the voltage ramp is passed through a low-pass filter to have a smoother time behavior. As the response of the piezo element is not linear with the applied voltage, an additional measurement is needed to obtain the time-scale for the recorded interferograms. The signal measured by the diode in the

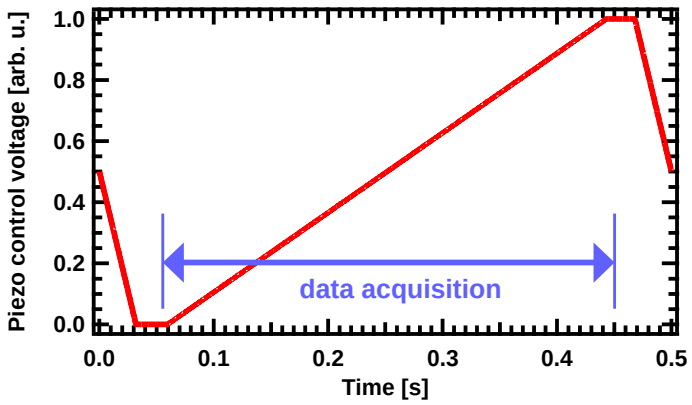

Figure 5.3: The voltage applied on the piezo moving one arm of the Mach-Zehnder interferometer during the TR-2PP experiment. The voltage is applied periodically, only one period is displayed.

reference beam is used for this purpose. While the arm of the interferometer is moving, the interferometric fringes are passing across the diode. From a known wavelength of the detected monochromatized light, one can easily calculate the delay between the two interfering beams.

The signal beam is after the Mach-Zehnder interferometer passing through dispersion-compensating and polarization-setting optics which was described in detail in Section 1.3.2.

In the UHV-photoemission chamber (see Sec. 1.3.3), the laser beam is impinging on the sample. Both photoemission and the surface SHG signals are detected at the same time. The SHG response of the surface is instantaneous. Therefore, the recorded SHG signal is providing the interferometric autocorrelation of the femtosecond pulse directly. By contrast, the photoemission signal is influenced by lifetimes of the intermediate states, as indicated in Fig. 5.1. Roughly said, the lifetimes of the hot electrons can be deduced from the difference between the SHG and 2PP traces. A broadening of the 2PP trace compared to the SHG trace is an indication of the non-zero lifetimes of the intermediate states. More detailed analysis will be provided in the next Section 5.3.

The geometry of the experiment is constrained by the fact that the intention is to measure the 2PP and SHG signals simultaneously. From the design of the UHV chamber used in the experiment, the 35° incidence angle of the 400 nm beam and normal (0°) emission geometry for the photoelectron detection is resulting. When the laser pulse properties are stable in time, however, it is possible to perform the experiment also with an oblique angle of emission of the photoelectrons. Then the SHG autocorrelation and

the 2PP signal have to be measured separately with the varying angle of incidence. The electrostatic photoelectron energy analyzer with a channeltron used for the detection of photoelectrons was described already in Section 1.3.3.

The SHG detection is complicated by a fact that the second harmonic of the 400 nm light is already in the UV region. Therefore, the filter-off of the fundamental (400 nm) light after the chamber cannot be done by a glass filter. The beam is sent through a prism instead and a spatial filtration is performed. For the detection of the 200 nm light, a photomultiplier working in a photon-counting regime is used. No polarization analysis of the SHG light is done. A background SHG signal is caused by the SHG generated in optical elements before the UHV-chamber. For suppressing this background, a blue filter is placed just before the beam is entering the vacuum apparatus.

Both SHG and 2PP signals are recorded by the pulse counting techniques (the FAST ComTec 7882 Multiscaler data acquisition system). The number of boxes in which the multiscaler is storing the data was chosen as 4096, the measurement time for one box was 125 μs which is at $\approx$2 Hz scan frequency covering the whole interferogram. The resolution of the interferogram is therefore $\approx$50 as. As the signal from the diode measuring the intensity of the reference beam is providing the time scale for the SHG and 2PP interferometric traces, correct timing over the whole acquisition window (500 ms for $\approx$2 Hz scans) with precision of one box of the multiscaler (125 μs) is absolutely necessary. The synchronization of the multiscaler and the A/D converter KPCI-3108 (used for measurements of the reference diode voltage) was not sufficiently precise. Replacing the diode by another photomultiplier (with a thick grey filter in front of it) helped to avoid any timing problems. The signal from the photomultiplier could be acquired also by the FAST ComTec 7882 Multiscaler and the correct timing was justified.

The number of scans needed for obtaining data of sufficient quality was determined by the intensity of both SHG and 2PP signals. In Fig. 5.4, results of a test measurement performed on the Au(111) surface can be seen. The SHG interferogram has clearly better quality than the 2PP interferometric trace. However, the improvement of the statistics can be easily done by measuring over an extended time interval or by averaging multiple interferograms.

The photoelectron analyzer is ready for attaching the spin analyzer, in this way the spin resolution can be achieved. The other way to obtain the spin resolution is an excitation by a circularly polarized light. The experimental setup described in this section is therefore a versatile tool allowing to conduct various experiments in the field of hot electron dynamics.

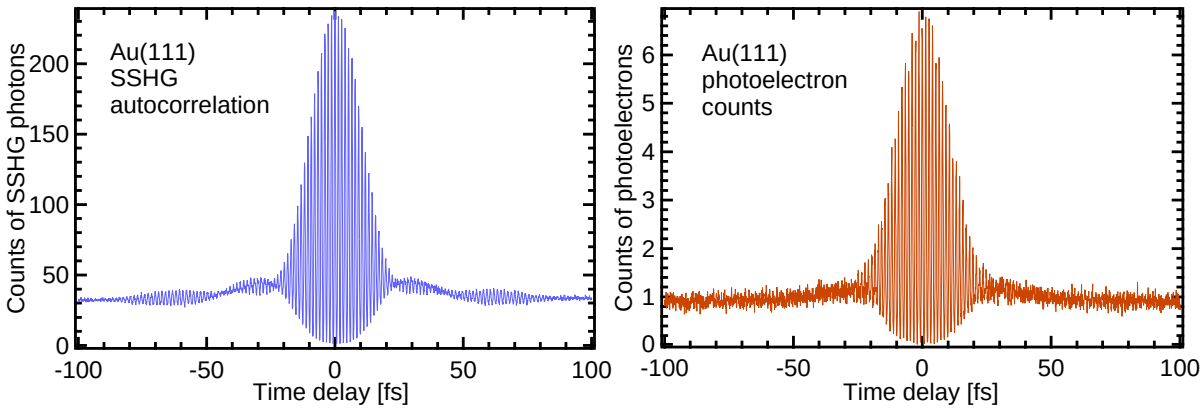

Figure 5.4: Left panel: The interferometric autocorrelation measured as the surface SHG on the Au(111) surface. Right panel: Simultaneously measured two-photon photoemission trace.

5.3 Processing of the experimental data — theory of ultrafast electron dynamics

From the experiment described in the previous section a data set consisting of two interferometric traces is obtained: the interferometric autocorrelation of the optical pulse (IfAC) measured by the surface SHG technique and the 2PP interferometric signal (in further text denoted as I2PP). In this section, it will be described how the lifetimes of the hot electrons can be obtained from these data.

The IfAC data are containing the information needed for the description of the femtosecond pulse. Important part of this work was focussed on obtaining the ultrashort pulse properties (the amplitude and the phase of the electric field) from the IfAC data. This is in detail described in Chapter 6. For the rest of this section, we will assume that the femtosecond pulse properties are known.

The complete theoretical description of the two-photon photoemission experiment should include the interaction of the electrons with the radiation, lattice and other electrons. Such a description would be rather complex, but it turns out that also simplified model can provide valuable results. Such model, feasible for the time-resolved two-photon photoemission experiment description, involves the optical Bloch equations (OBE) formalism. The OBE model is described in detail elsewhere [14, 98], however, for the two-level system only.

The OBE model is based on a density matrix description of the time evolution of an atomic system in response to an external time-dependent perturbation. It serves well as a heuristic model for analyzing the data from the TR-2PP experiments [8, 99, 100]. The

I2PP measurements are simulated by calculating the final state population of electrons (vacuum state) excited by a two-pulse sequence

$$E(t) = \tilde{\mathcal{E}}(t)\mathrm{e}^{\mathrm{i}\omega_0 t} + \tilde{\mathcal{E}}(t-\tau)\mathrm{e}^{\mathrm{i}\omega_0(t-\tau)} \ , \tag{5.2}$$

where $\tilde{\mathcal{E}}(t)$ is the slowly varying complex envelope of the pulse (which has to be determined from the IfAC data), ω_0 is a carrier frequency and τ is the delay between the two pulses. The response of the system to a perturbation is described by a linear combination of the basis functions of the undisturbed system φ_j, $\psi(t) = \sum_j a_j(t)\varphi_j$, $j = 0, 1, 2$. It is useful to transform the coefficients into a rotating set of coordinates: $c_j(t) = \mathrm{e}^{\mathrm{i}j\omega_0 t}a_j(t)$. The differential equations for motion of c_j then write

$$\frac{\mathrm{d}c_j}{\mathrm{d}t} = -\mathrm{i}\Delta_j c_j + \frac{\mathrm{i}}{2\hbar}p_{j,j-1}\tilde{E}^*(t)c_{j-1} + \frac{\mathrm{i}}{2\hbar}p_{j,j+1}\tilde{E}(t)c_{j+1} \ , \tag{5.3}$$

where p_{nm} are transition dipole moments and $\Delta_j = \omega_j - j\omega_0$ is describing the nonresonant energy of the level j with respect to the ground state and j-multiple of the central laser energy ω_0. The equation (5.3) is used to derive nine coupled differential equations (the optical Bloch equations) describing the time evolution of populations and polarizations associated with the levels indicated in Fig. 5.5. The populations and polarizations can

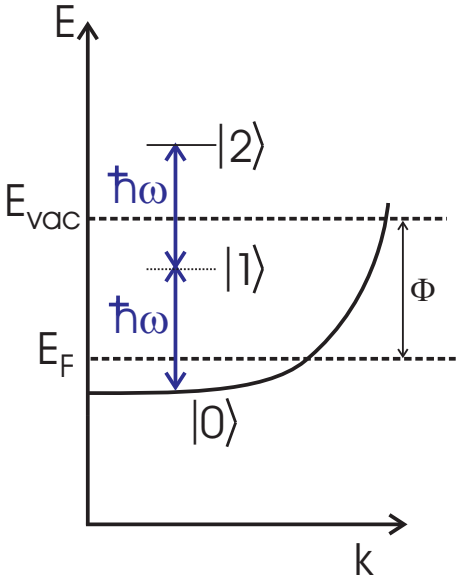

Figure 5.5: Schematic energy diagram of the two-photon photoemission. Initial $|0\rangle$, intermediate $|1\rangle$ and final $|2\rangle$ state are coupled by pump and probe pulses.

be represented by the density matrix:

$$\rho = \begin{pmatrix} c_0c_0^* & c_0c_1^* & c_0c_2^* \\ c_1c_0^* & c_1c_0^* & c_1c_2^* \\ c_2c_0^* & c_2c_0^* & c_2c_2^* \end{pmatrix} . \tag{5.4}$$

The diagonal elements provide the time-dependent populations $\rho_n = c_n^* c_n$, $(n = 0, 1, 2)$, while the off-diagonal elements represent the polarizations — optically induced coherence between the levels $\rho_{nm} = c_n^* c_m$, $(n, m = 0, 1, 2)$. The complete set of optical Bloch equations for a three-level system can be found in Ref. [100]: for the complex electric field that excites the system

$$E(t) = \tilde{\epsilon}(t)\mathrm{e}^{\mathrm{i}\omega_0 t} \tag{5.5}$$

the optical Bloch equations write

$$\frac{\partial \rho_{11}}{\partial t} = \frac{\mathrm{i}}{2\hbar} d_{01} \left(\tilde{\epsilon}^* c_0 c_1^* - \tilde{\epsilon}\, c_1 c_0^*\right) + \frac{\mathrm{i}}{2\hbar} d_{12} \left(\tilde{\epsilon}\, c_2 c_1^* - \tilde{\epsilon}^* c_1 c_2^*\right) - \frac{1}{T_1^1}\rho_{11} \tag{5.6}$$

$$\frac{\partial \rho_{22}}{\partial t} = \frac{\mathrm{i}}{2\hbar} d_{12} \left(\tilde{\epsilon}^* c_1 c_2^* - \tilde{\epsilon}\, c_2 c_1^*\right) - \frac{1}{T_1^2}\rho_{22} \tag{5.7}$$

$$\frac{\partial \rho_{00}}{\partial t} = -\frac{\partial \rho_{11}}{\partial t} - \frac{\partial \rho_{22}}{\partial t} \tag{5.8}$$

$$\frac{\partial (c_1 c_0^*)}{\partial t} = \frac{\mathrm{i}}{2\hbar} d_{01} \tilde{\epsilon}^* \left(\rho_{00} - \rho_{11}\right) - \frac{\mathrm{i}}{2\hbar} d_{12} \tilde{\epsilon}\, c_2 c_0^* - \left(\mathrm{i}\Delta_1 + \frac{1}{2T_1^1} + \frac{1}{T_2^{01}}\right) c_1 c_0^* \tag{5.9}$$

$$\begin{aligned} \frac{\partial (c_2 c_1^*)}{\partial t} = {} & \frac{\mathrm{i}}{2\hbar} d_{12} \tilde{\epsilon}^* \left(\rho_{11} - \rho_{22}\right) - \frac{\mathrm{i}}{2\hbar} d_{01} \tilde{\epsilon}\, c_2 c_0^* \\ & - \left(\mathrm{i}\left(\Delta_2 - \Delta_1\right) + \frac{1}{2T_1^2} + \frac{1}{2T_1^1} + \frac{1}{T_2^{12}}\right) c_2 c_1^* \end{aligned} \tag{5.10}$$

$$\frac{\partial (c_2 c_0^*)}{\partial t} = \frac{\mathrm{i}}{2\hbar} \tilde{\epsilon}^* \left(d_{12} c_1 c_0^* - d_{01} c_2 c_1^*\right) - \left(\mathrm{i}\Delta_2 + \frac{1}{2T_1^2} + \frac{1}{T_2^{02}}\right) c_2 c_0^* . \tag{5.11}$$

The decay of ρ_n and ρ_{nm} is caused by scattering and it is included in the optical Bloch equations through T_1^n — the energy relaxation time due to inelastic collisions and T_2^{nm} — the phase relaxation time due to elastic collisions. The optical Bloch equations are solved numerically for the given population of the final state $\rho_2(\tau) = \int c_2^* c_2 \mathrm{d}t$ measured in the experiment (I2PP) as a function of the pump-probe delay τ.

From the numerical solution of the optical Bloch equations the relaxation times are obtained. T_1^1, T_2^{01}, T_2^{12} and T_2^{02} contribute to the τ dependence of the I2PP, while T_1^0 and T_1^2 influence only the magnitude of the measured photoemission signal. T_1^1 is the inelastic scattering time of the intermediate state $|1\rangle$ which in causing an incoherent (nonoscillating) decay of the correlation traces, T_2^{01} and T_2^{12} describe the decoherence of the polarizations that couple $|0\rangle$ and $|1\rangle$ states (respectively $|1\rangle$ and $|2\rangle$). The T_2^{02} decay time is describing the two-photon induced polarization between $|0\rangle$ and $|2\rangle$.

For the relaxation parameters, much longer than the pulse width a simplified processing of the experimental data is possible [99]. It is based on a decomposition of the I2PP data into 0ω, 1ω and 2ω envelopes. However, for relaxation times comparable to the pulse width a complete numerical fitting of the optical Bloch equations is necessary [100].

The optical Bloch equation analysis is providing a scheme for processing the experimental data. However, no information about the physical nature of the processes that are influencing the electron dynamics can be obtained. Generally, the decoherence is caused by the scattering of the electron-hole pairs with the deformation potential, impurities, Fermi sea, or the surface. For the decay of the population of the intermediate state, there is responsible mainly the electron-electron scattering. However, the detailed study of these processes is not an aim of this work.

In this section, the optical Bloch equations formalism for describing the decay times of the hot electrons was introduced. The experimental input for the analysis is the 2PP interferometric signal. However, the first step in the calculation has to be the determination of the properties of the optical pulse used in the experiment. The objective of this work was therefore focussed more on the femtosecond pulse shape and phase analysis than on the application of the OBE formalism. The next chapter will be therefore fully concerned about the determination of the ultrashort pulse properties.

Chapter 6

Characterization of ultrashort laser pulses

In the experimental arrangement for the time-resolved two-photon photoemission the sub-10 fs pulses are produced by the titanium-sapphire laser system (see Section 1.3.1). As the resolution of the time-resolved experiments is directly related to the laser pulse width, it is necessary to work with the pulses as short as possible. For the adjustment of the whole setup, it is very important to be able to measure the detailed pulse properties (i.e. the amplitude and the phase of the electric field), so that a setting producing the shortest pulses can be achieved. For the analysis of the results of the time-resolved experiments by means of the optical Bloch equations, it is also necessary to know the exact amplitude and a phase of the electric field in the femtosecond pulse. In this chapter, we will therefore deal with a problem of determination of the laser pulse length and its shape in a sub-10 fs scale. Also a novel method which is quite easily applicable in the experimental arrangement used for the TR-2PP will be described.

6.1 Overview of pulse-characterization methods

In this section, the principles which are used for obtaining the amplitude and the phase of the electric field in ultrashort optical pulses will be briefly reviewed. The limits of use and basic advantages and disadvantages will be addressed.

6.1.1 Intensity autocorrelation

The temporal intensity profile $I_s(t)$ of an optical pulse can be easily determined when a shorter reference pulse of known shape $I_r(t)$ is available. If we define the Fourier transforms of the intensity profiles as

$$I_j(\omega) = \int_{-\infty}^{\infty} I_j(t) \mathrm{e}^{-\mathrm{i}\omega t} \mathrm{d}t \ , \qquad \text{where} \quad j = r \text{ or } s \ , \tag{6.1}$$

then the pulse shape can be determined by measuring the *intensity cross-correlation*

$$A_c(\tau) = \int_{-\infty}^{\infty} I_s(t) I_r(t-\tau) \mathrm{d}t \ . \tag{6.2}$$

This can be done by detecting a second-harmonic response in a nonlinear medium to the simultaneous excitation by the signal and the reference beams delayed by τ with respect to each other. Thanks to the fact that in the Fourier domain the equation (6.2) transforms into

$$A_c(\omega) = I_r(\omega) I_s^*(\omega) \ , \tag{6.3}$$

the Fourier transform of the pulse shape $I_s(\omega)$ can be easily extracted and after applying the inverse Fourier transform the pulse shape $I_s(t)$ can be obtained. Since now on we denote the Fourier transform of a function by replacing its time argument by a frequency argument (for instance $I(\omega)$ is the Fourier transform of $I(t)$).

This operation can be used with any reference pulse, in principle, but only for reference pulses which are shorter than the signal pulse (i.e. they have a broader spectrum) this procedure can lead to a reasonable signal-to-noise ratio. Unfortunately, for the experiments described in this thesis, no reference pulse shorter than the signal pulse was available. This is because the aim was to to make the signal pulse as short as possible (a few femtoseconds). In such a case, the signal pulse itself can be used also as a reference pulse $I_s(t) = I_r(t) = I(t)$ and the definition (6.2) transforms into a definition of the *intensity autocorrelation* (IAC)

$$\mathrm{IAC}(\tau) = \int_{-\infty}^{\infty} I(t) I(t-\tau) \mathrm{d}t \ . \tag{6.4}$$

In the Fourier domain, one gets then

$$\mathrm{IAC}(\omega) = |I(\omega)|^2 \ . \tag{6.5}$$

One has to keep in mind that the signal and the reference pulse should not interfere which is guaranteed by a noncollinear adjustment of the first beam and the beam delayed by τ. However, from the autocorrelation IAC(τ) it is not possible to obtain an unambiguous pulse shape $I(t)$ as the autocorrelation contains too little information. Usually, one has to assume a certain pulse shape and then the pulse length is adjusted to satisfy the equation (6.4).

For a laser setup producing ultrashort pulses, it is expectable that such an apriori pulse shape assumption would not lead to a result describing the pulses satisfactorily well. Moreover, it is not possible to obtain a phase information (which is necessary for a complete pulse description) from the IAC without any further measurements.

6.1.2 Interferometric autocorrelation

When the beam of the pulsed laser system is split into two parts in an interferometer (Michelson, Mach-Zehnder...) and the collinear arrangement of the two beams is maintained, the beams can interfere prior to exciting the nonlinear medium. Then, instead of the intensity autocorrelation, one obtains the interferometric autocorrelation (IfAC)

$$\mathrm{IfAC}(\tau) = \int_{-\infty}^{\infty} \{[E(t) + E(t-\tau)]^2\}^2 \mathrm{d}t \ . \tag{6.6}$$

For three basic pulse shapes (see Table 6.1), the IfAC is plotted in Fig. 6.1 for illustration.

The interferometric autocorrelation contains much more information about the pulse than the intensity autocorrelation. Even the phase information can be extracted. Howev-

Pulse shape	Intensity profile
Gaussian	$\mathrm{e}^{-2\left(\frac{t}{\tau}\sqrt{2\ln 2}\right)^2}$
Lorentzian	$\left(\frac{1}{1+\left(\frac{t}{\tau}2\sqrt{\sqrt{2}-1}\right)^2}\right)^2$
Secant hyperbolic	$\left(\frac{2}{\mathrm{e}^{\frac{t}{\tau}(2\ln(\sqrt{2}+1))}+\mathrm{e}^{-\frac{t}{\tau}(2\ln(\sqrt{2}+1))}}\right)^2$

Table 6.1: The basic pulse shapes, τ denotes the intensity-FWHM.

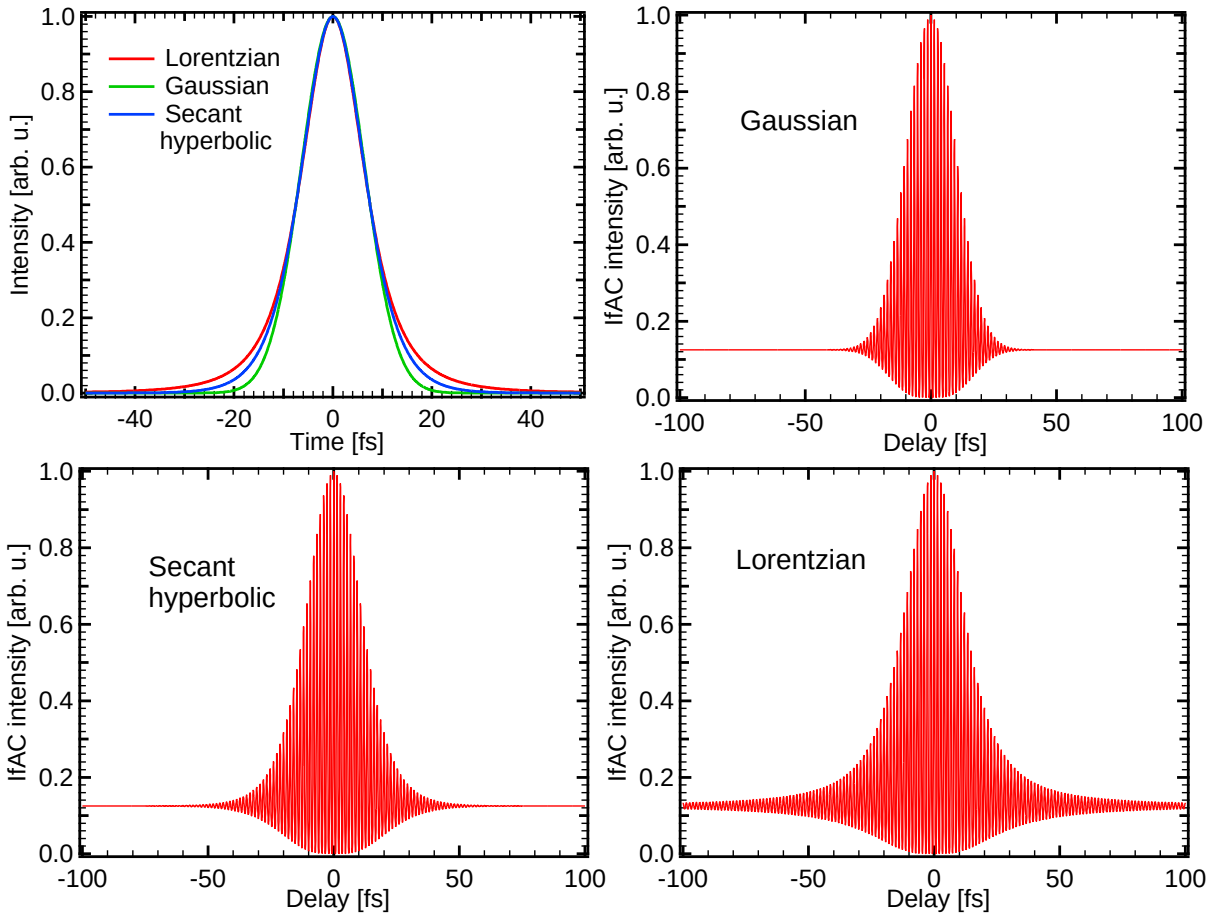

Figure 6.1: The interferometric autocorrelation calculated for three basic pulse shapes. The pulse intensity FWHM is 15 fs, the wavelength used for the calculation is 400 nm.

er, most of the methods for obtaining a pulse shape and a phase from the interferometric autocorrelation need an additional information about the pulse (i.e. the spectral intensity for instance). In Section 6.2, some of these approaches will be discussed.

6.1.3 Frequency-resolved optical gating

One of commonly used methods for characterization of femtosecond laser pulses is a Frequency-Resolved Optical Gating (FROG). This method operates in so called *time-frequency domain* which means that the complete set of experimental data required for the pulse reconstruction has to be both temporally and spectrally resolved. For the most sensitive type of FROG, which is involving the second harmonic generation process

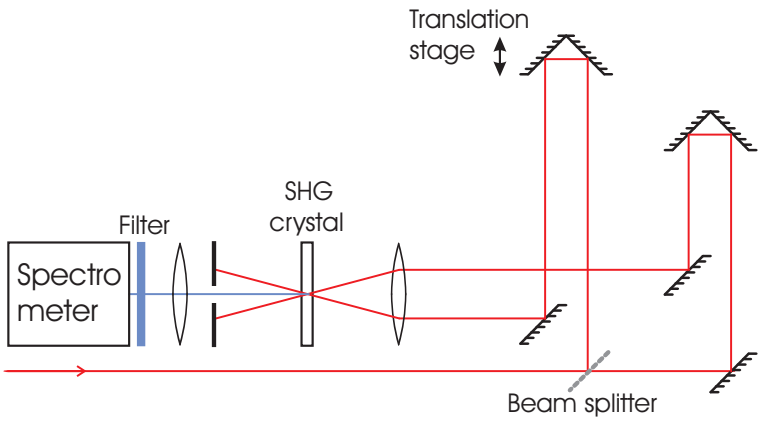

Figure 6.2: Basic experimental setup of the SHG FROG.

(SHG FROG), the required data are forming a time-resolved spectrogram [101]

$$I_{\mathrm{FROG}}^{\mathrm{SHG}}(\omega,\tau) = \left| \int_{-\infty}^{\infty} E(t)E(t-\tau)\mathrm{e}^{-\mathrm{i}\omega t}\mathrm{d}t \right|^2 . \tag{6.7}$$

The experimental setup is displayed in Fig. 6.2. In principle, this is a spectrally resolved autocorrelator. For varying delays τ between the two parts of the beam, the spectrum of the SHG signal is recorded and thereby the $I_{\mathrm{FROG}}^{\mathrm{SHG}}(\omega,\tau)$ function acquired.

An iterative algorithm has to be applied to extract the pulse shape and the phase from the experimental data [102–105]. A general property of the pulse retrieval algorithms is that for experimental data consisting of N spectra, each spectrum having N points, it is necessary to perform N Fourier transforms (and additional N inverse Fourier transforms) in each step of the iterative algorithm.

6.2 Determination of the fs-pulse properties

The FROG method described in the previous section seems to be a robust tool for determination of the pulse shape. However, in the two-photon photoemission experimental setup there appear some difficulties when applying this method. It is important to know the pulse shape and its phase directly at a position of the sample which is located in a UHV chamber. In this case, it is not very simple to build a FROG apparatus inside the UHV chamber. Such a setup needs precise alignment of very tiny optical components (the nonlinear crystal, for instance). Other complication arises from a fact that the SHG signal of the pulses (with a wavelength $\approx$400 nm) is already in the UV region

(≈200 nm) which is even more complicating the manipulation with the beams. Also the noncollinearity of the FROG setup (see Fig. 6.2) is complicating its use in UHV. However, the noncollinearity issue can be solved [106] for the price of more complex data processing.

As the FROG methods are quite unfavorable in the case of the experimental setup described in Chapter 5, it is feasible to rely on methods which are using the interferometric autocorrelation (IfAC) as a basic data set for obtaining the pulse shape and the phase. Very convenient approach is to use a surface of the sample as a nonlinear medium and generate the IfAC by the surface SHG from the sample itself. Details about the surface SHG can be found in Chapter 3. The major advantage of this method is that the IfAC is generated directly on the surface of the sample and therefore it describes pulse properties directly at the specimen location. Because the efficiency of the surface SHG is very low, it doesn't allow to analyze spectrally the signal. Therefore, an application of the FROG approach is not possible and one has to rely on other methods.

The first use of the interferometric autocorrelation for the pulse characterization was reported by Diels et al. [107] in 1985. The method was improved and rigorous mathematical theory was developed by Naganuma et al. [108] a few years later. However, there was always a need of some additional experimental data to complement the IfAC information. Usually, the intensity spectrum was used. A robust algorithm for the pulse shape and phase retrieval with the use of an intensity autocorrelation and an intensity spectrum was developed by Peatross and Rundquist [109]. The method developed here is also based on this algorithm. However, it will be shown that solely the IfAC can be used instead of a combination of IAC and intensity spectrum measurements, as proposed by Weida et al. [110].

6.2.1 The pulse shape — TIVI algorithm

The present algorithm for the pulse shape retrieval is based on the work of Peatross and Rundquist [109]. Their TIVI (temporal information via intensity) method is schematically illustrated in Fig. 6.3.

The calculation is based on a so called error-reduction algorithm developed by Fienup [111]. The fitting cycle is formed by a forward and inverse Fourier transforms applied on the pulse intensity profile $I(t)$. For the Fourier transform calculation, the FFTW C-subroutine library [112] was used in this work. An input for the algorithm consists of the intensity autocorrelation IAC(t) and the initial guess of the pulse shape $I(t)$. The convergence is achieved by applying constrains which arise from physical nature of the

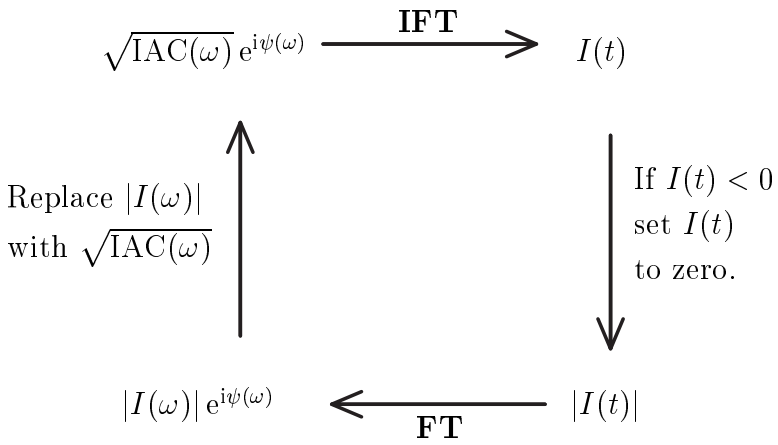

Figure 6.3: Schematic of the TIVI method for recovering of the pulse shape, as proposed by Peatross and Rundquist [109].

data set. In the time-domain, the constrain is that the $I(t)$ should be nonnegative. In the frequency domain, the measured intensity autocorrelation gives directly the absolute value of the Fourier-transformed intensity profile $I(\omega)$, as can be seen from the equation (6.5). When these constrains are applied in a fitting cycle, as indicated in Fig. 6.3, the procedure is converging to the correct pulse shape $I(t)$ (and also to the correct phase $\psi(\omega)$ in the frequency domain). It has been shown that the error reduction algorithm never increases the error. In the worst case it is stagnating. However, modifications of the fitting cycle can be made in order to achieve better convergence [109].

Our modification of the approach of Peatross and Rundquist is based on replacing the intensity autocorrelation (IAC) by the interferometric autocorrelation (IfAC). The interferometric autocorrelation is in this case favorable because it contains a phase information as well. It can be therefore used also in the next part of the pulse characterization procedure. Moreover, the experimental setup which is normally used for time-resolved measurements (see Chapter 5, Fig. 5.2) is providing the interferometric autocorrelation conveniently. Here it will be shown that one can obtain the information contained in the intensity autocorrelation by simple treatment of the interferometric autocorrelation. The IfAC was defined already in the equation (6.6) as

$$\mathrm{IfAC}(\tau) = \int_{-\infty}^{\infty} \{[E(t) + E(t-\tau)]^2\}^2 \mathrm{d}t \ . \tag{6.8}$$

The electric field of the pulse can be written

$$E(t) = \tilde{\mathcal{E}}(t)\mathrm{e}^{\mathrm{i}\omega_0 t} \ , \tag{6.9}$$

where ω_0 is a carrier frequency and $\tilde{\mathcal{E}}(t) = \mathcal{E}(t)\mathrm{e}^{\mathrm{i}\varphi(t)}$ is slowly varying complex envelope. By substituting this expression of $E(t)$ into the equation (6.8) it can be seen that it is possible to split the expression into three terms well separated in the Fourier space [14]

$$\mathrm{IfAC}(\tau) = G(\tau) + \mathrm{Re}\left\{4\tilde{B}(\tau)\mathrm{e}^{\mathrm{i}\omega_0\tau}\right\} + \mathrm{Re}\left\{2\tilde{C}(\tau)\mathrm{e}^{\mathrm{i}2\omega_0\tau}\right\} \ , \tag{6.10}$$

where

$$G(\tau) = \int_{-\infty}^{\infty} \left(\mathcal{E}^4(t-\tau) + \mathcal{E}^4(t) + 4\mathcal{E}^2(t-\tau)\mathcal{E}^2(t)\right) \mathrm{d}t \ , \tag{6.11}$$

$$\tilde{B}(\tau) = \int_{-\infty}^{\infty} \mathcal{E}(t-\tau)\mathcal{E}(t)\left[\mathcal{E}^2(t-\tau) + \mathcal{E}^2(t)\right] \mathrm{e}^{\mathrm{i}[\varphi(t-\tau)-\varphi(t)]} \mathrm{d}t \ , \tag{6.12}$$

$$\tilde{C}(\tau) = \int_{-\infty}^{\infty} \mathcal{E}^2(t-\tau)\mathcal{E}^2(t)\mathrm{e}^{2\mathrm{i}[\varphi(t-\tau)-\varphi(t)]} \mathrm{d}t \ . \tag{6.13}$$

It is obvious that the zero-frequency term $G(\tau)$ is corresponding to the intensity autocorrelation (plus background term). In the Fourier-image, the $G(\tau)$ term can be separated from $\tilde{B}(\tau)$ and $\tilde{C}(\tau)$ and used instead of the IAC in the TIVI algorithm (the background term vanishes). Schematic of the procedure using the $G(\tau)$ term from the interferometric autocorrelation is displayed in Fig. 6.4. In each iteration step, only one forward and one inverse Fourier transform has to be calculated, in contrast to the FROG

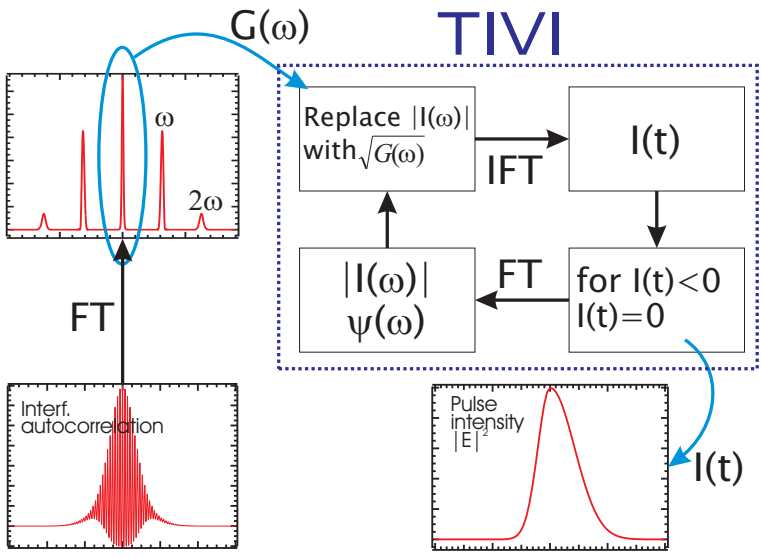

Figure 6.4: Schematic of the modified TIVI method used for the recovering of the pulse shape.

algorithm, where during every iteration cycle $2N$ transforms have to be performed (N being the dimension of the FROG data set).

6.2.2 The pulse phase — Gerchberg-Saxton algorithm

In Fig. 6.5, a schematic of the Gerchberg-Saxton algorithm which is used for recovering of the phase of the electric field in the femtosecond pulse can be seen. The algorithm was originally developed for reconstruction of a two-dimensional spatial phase information of images from known amplitudes of the field at the near- and far-field planes [113]. As an input uses this calculation the electric field amplitude (obtained in the previous step by the TIVI algorithm) and the intensity spectrum $S(\omega)$ which can be expressed in terms of the electric field Fourier transform as

$$S(\omega) = |E(\omega)|^2 \ . \tag{6.14}$$

The algorithm is based on the fact that the modulus of a complex field in the time domain $|E(t)| = \sqrt{I(t)}$ and a modulus of its Fourier transform $|E(\omega)| = \sqrt{S(\omega)}$ define the electric field $E(t)$ (and also the $E(\omega)$) completely in most situations [114]. The calculation consists of a sequence of forward and inverse Fourier transformations with the spectral and temporal amplitudes being replaced by $\sqrt{S(\omega)}$ and $\sqrt{I(t)}$ in each iteration step. It is useful to shift the $S(\omega)$ on the frequency axis so that its maximum is at zero, the frequency shift then corresponds directly to the central frequency ω_0 of the recovered pulse.

The procedure for obtaining the phase information described above has one principal disadvantage — one needs to know the intensity spectrum of the pulse. To obtain

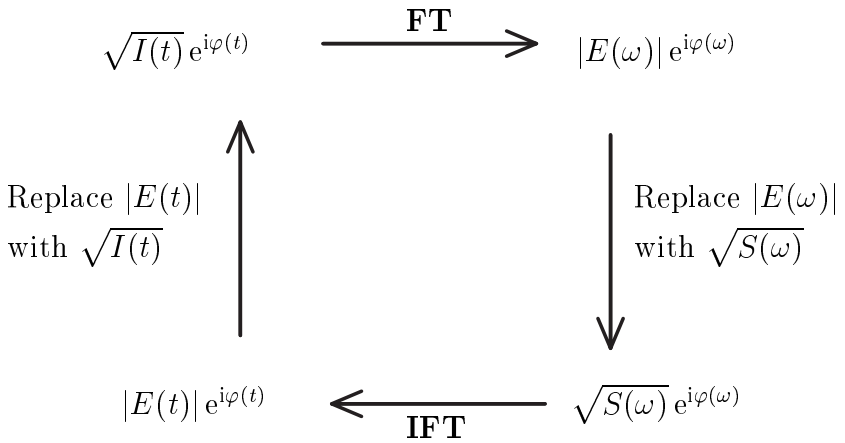

Figure 6.5: Schematic of the Gerchberg - Saxton method [113], as proposed by Peatross and Rundquist [109] for recovering of the phase of the electric field.

the spectrum directly at the sample position in the UHV chamber brings experimental difficulties, the intensity spectrum is therefore usually measured outside the chamber. However, such spectrum can slightly differ from the real spectrum in the chamber and the result of the fitting procedure can be thereby influenced. In this work, it will be demonstrated that the determination of the phase of the electric field can be done with a knowledge of the IfAC only. No additional data have to be measured for the phase determination because the IfAC was measured already as the input for the TIVI method for the pulse shape determination.

It can be seen directly from the equations (6.10) and (6.13) that the feature located in the Fourier transform at two times the laser fundamental is the Fourier transform of the autocorrelation of the square of the electric field $\tilde{u}(t) = \tilde{\mathcal{E}}(t)^2$:

$$\tilde{C}(\omega) = |\tilde{u}(\omega)|^2 \,, \tag{6.15}$$

as was pointed out already by Naganuma et al. [108]. The Gerchberg - Saxton algorithm is then modified so that it recovers the phase of $\tilde{\mathcal{E}}(t)^2$ as can be seen in Fig. 6.6. The phase of the electric field is then obtained by simply dividing the resulting phase from the iterative cycle by two. When separating the $\tilde{C}(\omega)$ part of the Fourier transform, the feature has to be shifted on the frequency axis so that its maximum is at zero. The shift has to be recorded while it is then corresponding to twice the central frequency ω_0 of the recovered pulse.

In this section, a summarized view on the algorithms which are used for the pulse shape and phase determination in this work was sketched. The whole procedure, as used in our calculations, is plotted in Fig. 6.7. However, more subtle approach is needed for

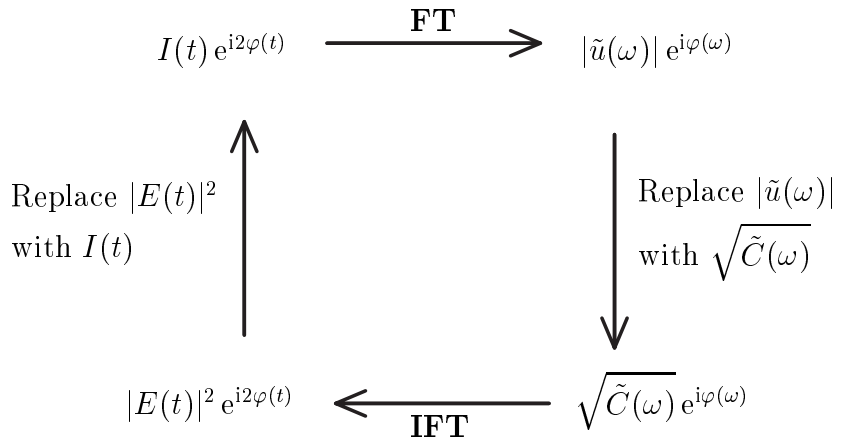

Figure 6.6: Schematic of the modified Gerchberg - Saxton method for the recovering of the phase of the electric field from the IfAC data.

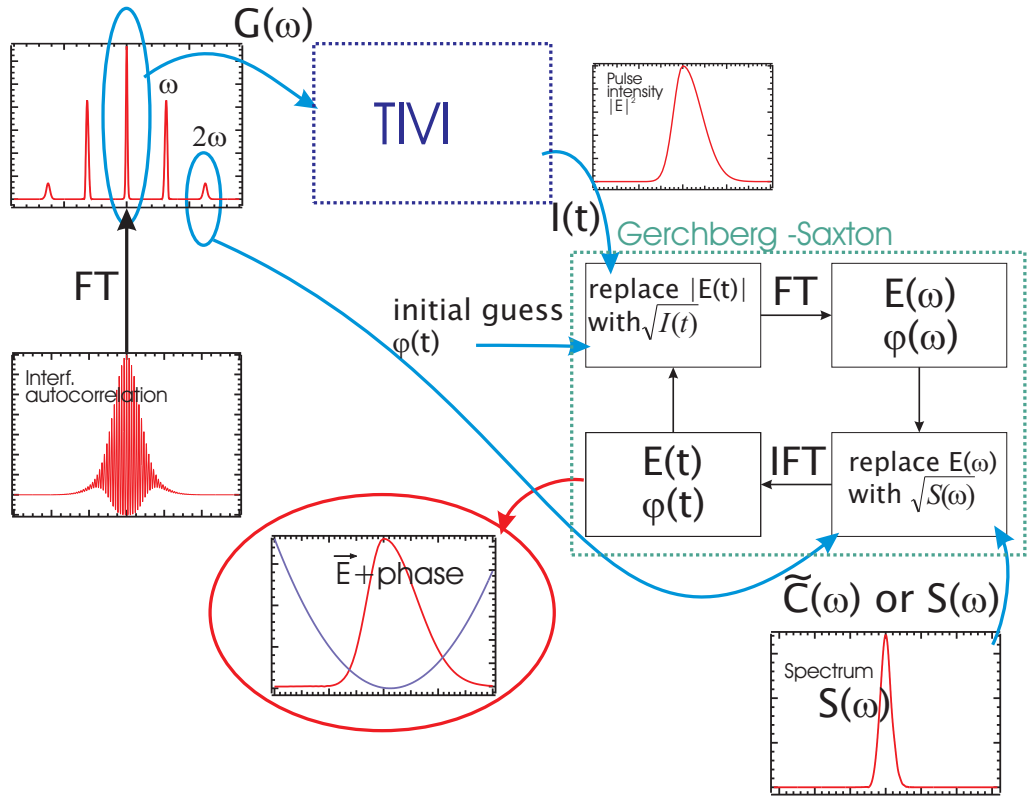

Figure 6.7: The algorithm used for the pulse and phase determination in this work. Both intensity spectrum $S(\omega)$ and the $\tilde{C}(\omega)$ part of the IfAC can be used in the procedure when calculating the phase.

optimization of the convergence of this calculation and methods have to be developed to judge the quality of the resulting pulse. This will be discussed in next sections.

6.3 Starting data selection for the algorithm

As mentioned already in the previous section, the error reduction algorithm in the TIVI method is never increasing the error, in the worst case it can stagnate at a given value. The stagnation of the error is unfortunately quite common case when fitting femtosecond pulses. Several methods have been developed for improvement of the convergence. In the papers by Fienup [111] and Peatross and Rundquist [109] some of the improvements of the algorithm which enhance the convergence are mentioned. They used a so called input-output algorithm consists in replacing the negative portions of $I(t)$ by their differences from their values in the previous iteration. Another option is to overcorrect the $I(\omega)$

value by several tens of % when it is being adjusted to its known value. It is also possible to combine these approaches in a hybrid algorithm.

The above mentioned improvements of the algorithm are influencing mainly the speed of the convergence during the first iterations which is, however, not so important for us. The recent computers (Pentium IV, 1.8 GHz) can handle about 3000 iterations within one second (the pulse is being sampled in 400 points). Therefore, the asymptotic behavior of the algorithm is more interesting than the progress in first few iterations. It turns out that the above mentioned improvements of the algorithm are playing minor role in influencing the result to which the procedure is converging and at which is it stagnating. More important seems to be a choice of the starting trial pulse data used as an input for the algorithm. This issue will be addressed in this section.

6.3.1 Test data description

For testing purposes, a sample data sets were prepared. The intention was to make the test pulses quite complex, similar to the real experiment. Theoretical predictions [115], and also experimental measurements [116–118], show that the output from a Ti:sapphire oscillator is in the general case asymmetric and should posses subpeaks. The electric field amplitude of the test pulse was therefore chosen of the hyperbolic secant shape, 15 fs FWHM (of the intensity) and two subpeaks at ±30 fs having 20% of the maximum amplitude of the main peak and also the 15 fs FWHM (of the intensity). The main peak was asymmetric in addition. This means that for negative values on the time scale the peak was calculated with an intensity-FWHM

$$\frac{2}{1+\mathcal{A}} \cdot 15\,\mathrm{fs} \tag{6.16}$$

for chosen value of asymmetry $\mathcal{A}$. The definition of the asymmetry $\mathcal{A}$ is indicated in the right panel of Fig. 6.8. The values of the electric field amplitude on the positive part of the time scale were calculated with

$$\frac{2\mathcal{A}}{1+\mathcal{A}} \cdot 15\,\mathrm{fs} \tag{6.17}$$

FWHM. Such choice justifies the FWHM value of 15 fs for the test pulse. For the test data set, the asymmetry of 2 was chosen. The subpeaks at ±30 fs were chosen as symmetric. The test pulse is displayed in the left panel of Fig. 6.8. The phase of the electric field was chosen to have a quadratic phase chirp (linear frequency chirp). From Eq. 6.14 the intensity spectrum can be directly calculated, it is displayed in the left panel of Fig. 6.9.

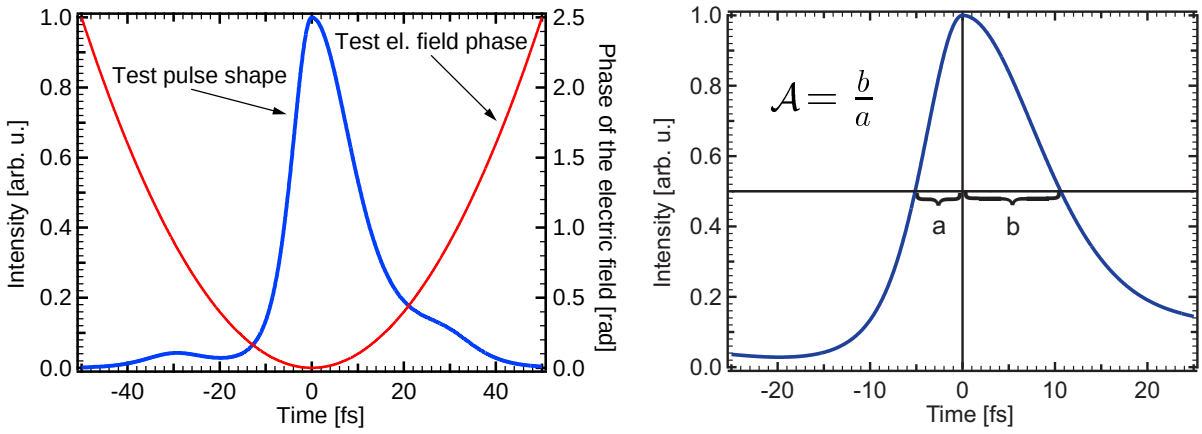

Figure 6.8: Left panel: The test pulse used for the testing of algorithms for the determination of the pulse shape and phase. The intensity shape $|E(t)|^2 = I(t)$ and the phase of the electric field $E(t)$ are displayed. Only a part of the full range (-600 fs to 600 fs) is displayed. Right panel: The definition of the asymmetry $\mathcal{A}$ of the pulse.

The test data have to be supplied to the algorithm in the form of an interferometric autocorrelation which is measured in the experiment. The IfAC calculated from the test pulse is displayed in the right panel of Fig. 6.9.

The IfAC is then used in the fitting algorithm in the way indicated in Fig. 6.4. As we are using an ideal data set without any noise, no background subtraction is needed in the Fourier domain. Care has to be taken when extracting the $G(\omega)$ term from the Fourier transform of the IfAC. This is because there is the $\tilde{B}(\omega)$ peak already appearing at the $1\omega \approx 3.1\,\mathrm{eV}$ frequency, only limited part of the Fourier data can be therefore used. The data in the interval $\pm 1\,\mathrm{eV}$ were safely taken for the calculation. However, this interval is defining the resolution of the reconstructed pulse. It corresponds to $\approx$2 fs resolution in the time space which can be considered to be quite rough. Therefore, the $G(\omega)$ function was extrapolated to the interval $\pm 2\,\mathrm{eV}$ by an exponentially decaying function. Such an expanded function we denote $G_{\mathrm{exp}}(\omega)$. By comparing results obtained with the use of $G_{\mathrm{exp}}(\omega)$ function and with the use of the Fourier transform of the correct pulse shape it was checked that this expansion doesn't influence the resulting pulse shape. Similar expansion of the $G(\omega)$ function has to be performed also in the case of the real experimental data. However, the background in the Fourier image, caused by the noise in the IfAC, has to be subtracted prior to the calculation of $G_{\mathrm{exp}}(\omega)$. The interval in which the $G(\omega)$ remains above the background level is determined by the accuracy of the IfAC measurement. In the case of the experimental setup described in Chapter 5, it was about $\pm 0.2\,\mathrm{eV}$ for a 40 minutes long measurement.

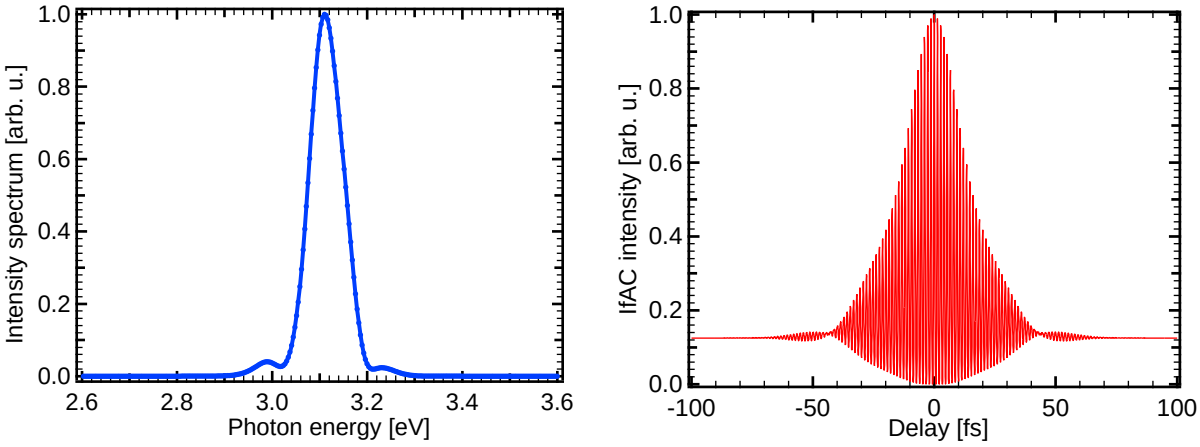

Figure 6.9: Left panel: The intensity spectrum $S(\omega)$ of the test pulse (displayed in Fig. 6.8). Right panel: The interferometric autocorrelation calculated from the test pulse. Only inset is displayed, the full range was -200 fs to 200 fs.

6.3.2 Starting data for the pulse shape recovery

Pulses with various shapes, widths and asymmetries were chosen as the trial input for the evaluation of the best choice of the starting (or trial) pulse for the algorithm. No subpulses were superimposed onto the test starting pulses. Resulting pulse shapes obtained with various starting pulses are displayed in Fig. 6.10. For each data set, 10^4 iterations were carried out. From the figure one can clearly see that the Lorentzian starting pulse is leading generally to the best results. This is probably due to the more pronounced wings of the Lorentzian shape which can improve the convergence in the regions where the pulse intensity is relatively low.

The asymmetry of the starting pulse is essential in the algorithm. As pointed out already by Peatross and Rundquist [109] there is nothing (except for numerical noise) in the algorithm that breaks the symmetry. Therefore, from an even trial pulse only even results can be obtained. To be able to recover both odd (asymmetric) and even (symmetric) pulse shapes an asymmetric starting pulse is needed.

By comparing results in individual panels in Fig. 6.10 the best choice for the asymmetry and width (intensity-FWHM) of the starting Lorentzian pulse were evaluated. The most satisfactory result is displayed in the top left panel — the asymmetry is chosen here to be larger ($\mathcal{A} = 3$) than for the test pulse and the pulse width is chosen smaller than that of the test pulse (13 fs). Similar results were obtained also for another types of the original pulse used for preparation of the test data (for example the asymmetric sech without subpeaks). Also in this case the choice of the Lorentzian starting pulse

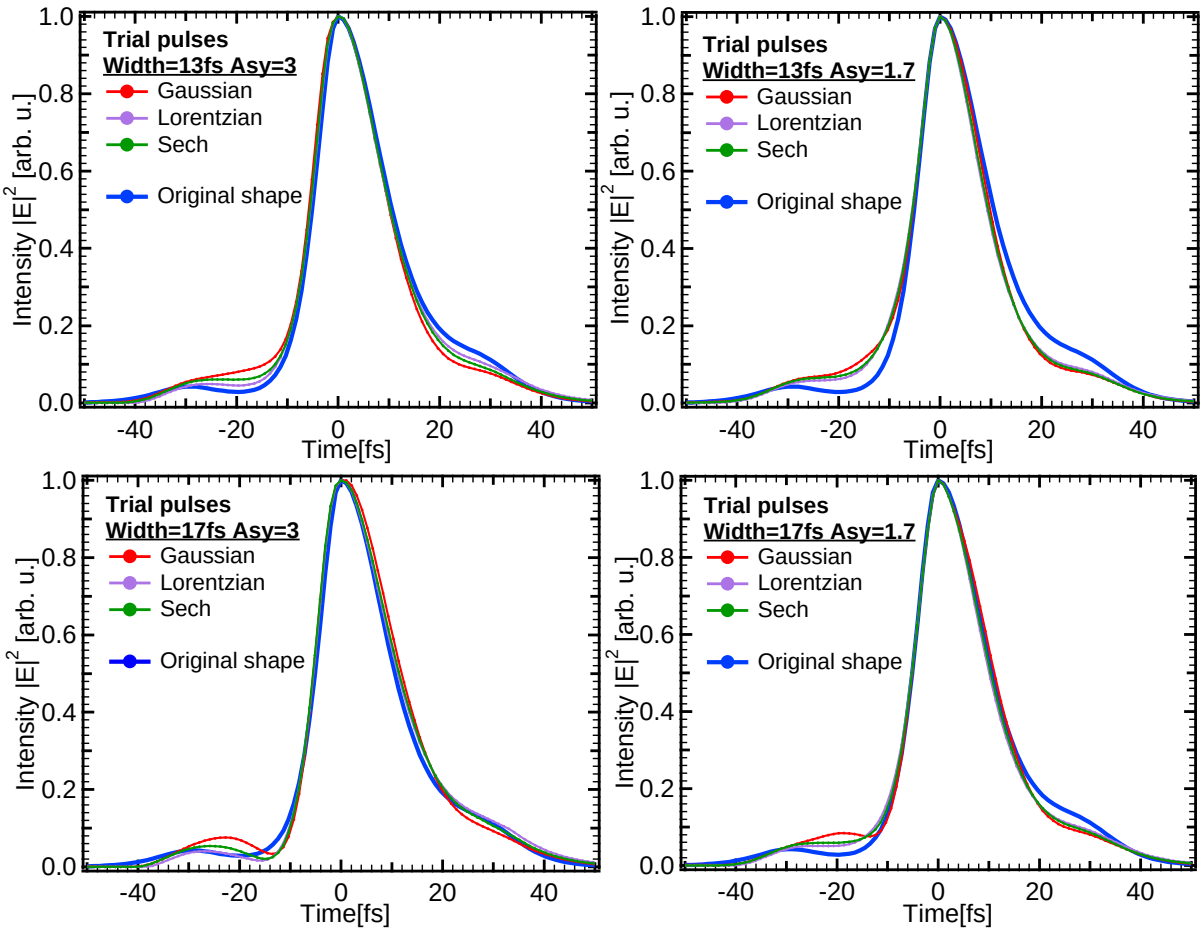

Figure 6.10: Results of the fit of the pulse shape for algorithm starting with various pulse shapes. The parameters of the trial pulses are denoted in the legend of each graph.

possessing a larger asymmetry and a smaller width than the original was a best choice for the starting pulse of the algorithm.

A more detailed view on the dependence of the starting pulse asymmetry on the result of the iterative algorithm is displayed in Fig. 6.11. Starting sech-shaped pulses with a 13 fs width and with a varying asymmetry were used in the algorithm and the resulting error was compared to find the best choice. The error of the resulting pulse was monitored in two ways. First way was to compare the $I(\omega)$ and $\sqrt{G(\omega)}$ in the Fourier domain and to calculate the error as a difference between them. As already mentioned in Section 6.2.1, this error is decreasing in every step of the algorithm. As the input data set used in this calculation is artificially produced, the exact information about the correct pulse shape is available. Comparing directly the pulse shape of the recovered pulse with the correct one is the second way how to monitor the error of the result of

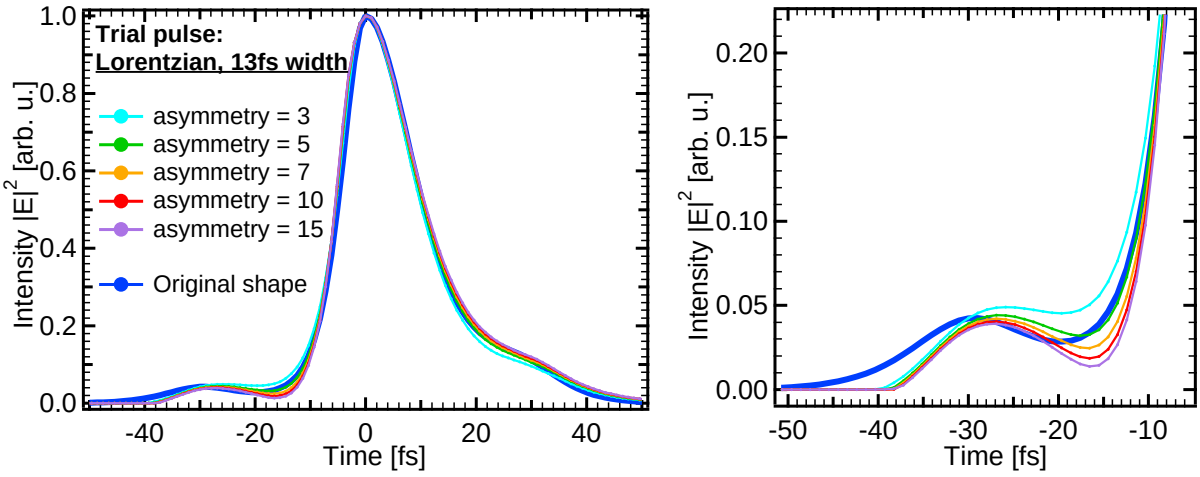

Figure 6.11: Results of the fit of the pulse shape for algorithm starting with Lorentzian pulse shapes having various asymmetries. The parameters of the trial pulses are denoted in the legend. In the right panel particular part of the graph is magnified.

Trial pulse asymmetry	Error in Four. domain	Error in time domain
$\mathcal{A} = 3$	3.4	8.3
$\mathcal{A} = 5$	3.0	5.8
$\mathcal{A} = 7$	2.9	7.5
$\mathcal{A} = 10$	2.8	9.6
$\mathcal{A} = 15$	2.7	11.7

Table 6.2: Errors of the resulting pulse shapes from Fig. 6.11. The error in the Fourier domain is calculated as the difference of $I(\omega)$ and $\sqrt{G(\omega)}$. In the time domain directly the difference from the correct pulse shape is calculated. Relative units.

the iterative algorithm.

In Table 6.2, the results from Fig. 6.11 are summarized. An apparent inconsistency between the two ways of the error evaluation can be seen. While the error in the Fourier domain is showing minimum for the largest asymmetry $\mathcal{A} = 15$, in the time domain is one arriving by comparing the result with the original pulse to the minimum at $\mathcal{A} = 5$. The origin of this discrepancy has to be ascribed to the fact the error reduction algorithm is minimizing in the Fourier domain the error which is described by the difference of $I(\omega)$ and $\sqrt{G(\omega)}$, but in the time domain the amount of negative portions of $I(t)$ is minimized. Unfortunately, this doesn't guarantee that also the difference between $I(t)$ and the correct pulse shape will be minimized. In the calculation with real experimental data, the convergence in the Fourier domain has to be therefore treated as an approximate

indicator only. Therefore, the actual quality of the result of the fit has to be judged by comparing the experimental IfAC with the IfAC calculated from the recovered pulse shape.

However, from Table 6.2 the best choice of the asymmetry of the starting pulse for the iterative procedure can be determined. It is $\mathcal{A} = 5$, for larger asymmetries the result is getting worse. Further checks have shown that the starting pulse with smaller width and larger asymmetry than expected result can be regarded as an optimum choice.

Similar calculations were performed also for another data sets with a symmetric original pulse. The convergence of the pulse shape for wide range of symmetric starting pulses was much better than in the case when the asymmetric pulse shape is fitted. However, in a real experiment with ultrashort laser pulses the assumption of the symmetric pulse cannot be made in general.

6.3.3 Starting data for the phase of the electric field recovery

A next step in the pulse recovering procedure is the determination of the phase of the electric field. Similarly to the pulse shape recovering, several approaches were tested with the test data to find the most favorable method. Normally, one would use the pulse shape resulting from the TIVI algorithm as the magnitude of the electric field, but for the testing purposes the correct pulse shape was chosen, so that the behavior of the phase-fitting algorithm could be monitored independently on the TIVI procedure.

For the starting (trial) phase of the electric field, polynomial functions of the form

$$\varphi(t) = 3.14 \left(A \left(\frac{t}{30\ \mathrm{fs}} \right) + B \left(\frac{t}{30\ \mathrm{fs}} \right)^2 + C \left(\frac{t}{30\ \mathrm{fs}} \right)^3 \right) \tag{6.18}$$

were used with various coefficients A, B and C. This data set serves as one of the inputs of the algorithm. One should mention that in this notation the phase of the test pulse (displayed in Fig. 6.8) would correspond to $A = 0$, $B \approx 0.3$ and $C = 0$.

Both approaches indicated in Fig. 6.5 (i.e. an additional use of the intensity spectrum) and Fig. 6.6 (i.e. a use of the IfAC data only) were tested. Selected resulting phases of the electric field are displayed in Fig. 6.12. One of the results is of high quality, one looks reasonably and one result is quite poor. For the comparison, the correct pulse phase is also plotted. The shift of the minimum of the resulting phase with respect to the zero delay on the time axis is explained by the fact that the the value of the central frequency obtained from the input data (which has to be recorded during the data treatment) is for asymmetric pulses not equal to the frequency used for the test-IfAC calculation.

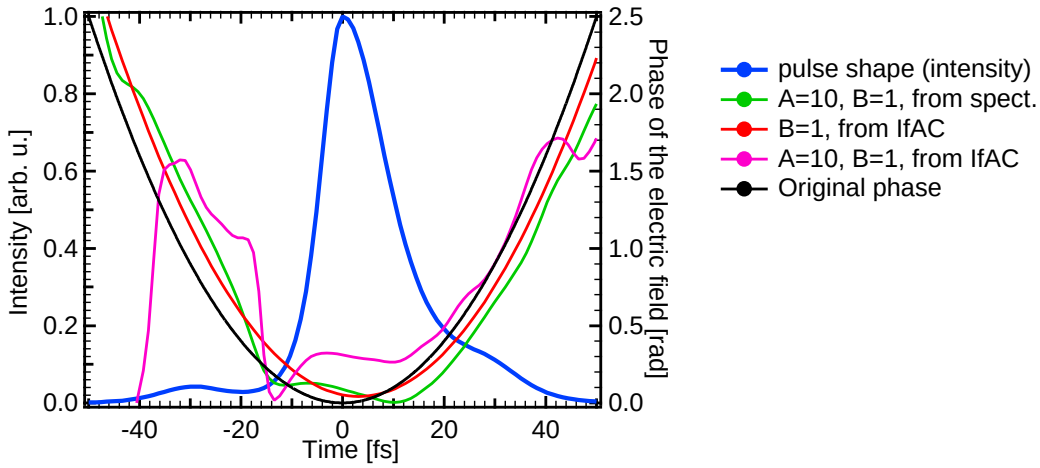

Figure 6.12: Results of the fit of the pulse phase, the pulse intensity shape data were fixed at the correct values. The phase data were obtained by the procedure according to Fig. 6.5 (with a use of the intensity spectrum) and also for the fitting procedure described in Fig. 6.6 (which uses of the IfAC data only). The full range of the recovered data was from -200 fs to 200 fs. Here only part of the interval is shown. Various starting values for the phase were used. For the meaning of the A and B variables, see Eq. 6.18.

A complete set of results of the phase fitting with the correct pulse shape is displayed in Fig. 6.13 and in Table 6.3. From the resulting descriptions of the electric field the IfACs are calculated back to see the difference from the original IfAC. All the results calculated with use of the intensity spectrum (the left panel of Fig. 6.13) are showing very good agreement with the original data. The results obtained from the IfAC only (the right panel of Fig. 6.13) are more sensitive to the choice of the starting phase. However, a very good matching with the correct IfAC is obtained also here for a wide range of stating phase choices. It shows that solely the IfAC can be used as the experimental input, however higher care has to be taken to the starting data selection.

In this section, it was described, how the starting pulse shape and phase for the iterative algorithm should be chosen. The asymmetric pulse shape having shorter width and larger asymmetry than the expected result is a good choice for the starting pulse shape for the algorithm. In the case described here, the optimum choice of the asymmetry was 2.5× larger than original value and the optimal width was by $\approx 15\%$ smaller than original pulse width. However, the optimum setting has to be found for every pulse by comparing the original and recovered interferometric autocorrelation. This procedure of finding optimum starting values will have to be carried out for each femtosecond laser setup only once, until substantial modifications influencing the pulse shape are made.

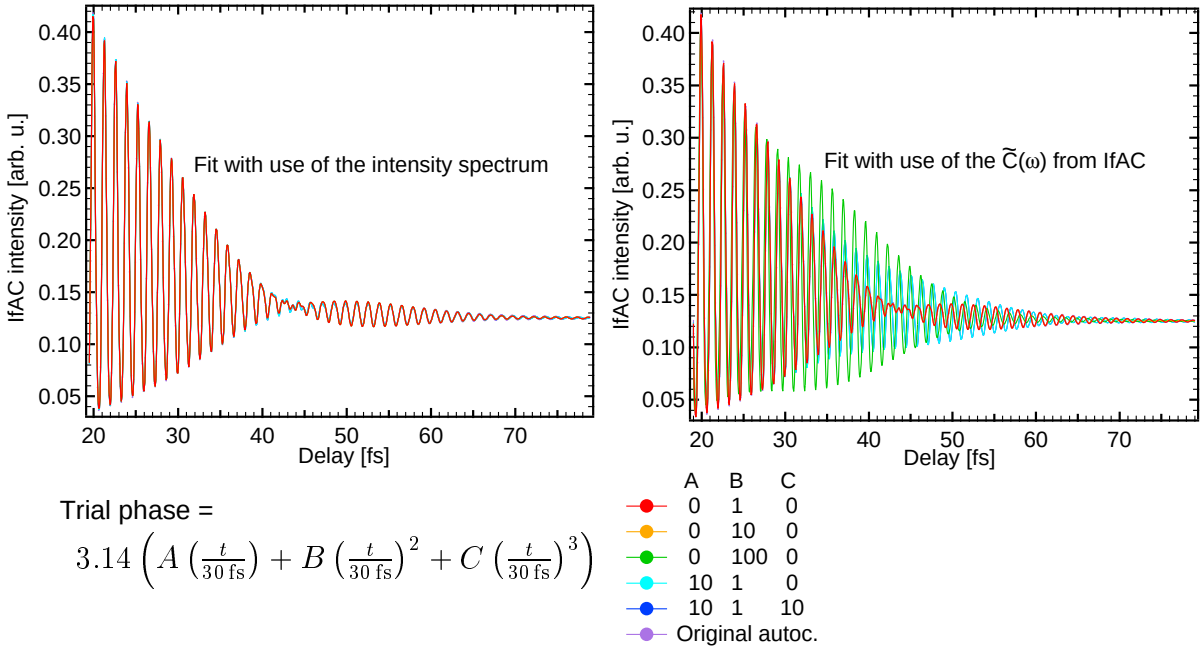

Figure 6.13: The IfAC calculated by using the correct pulse shape and the phase of electric field obtained from the fit with various starting values of the phase (indicated in the legend). Left panel: The fitting procedure as in Fig. 6.5 (use of the intensity spectrum). Right panel: The fitting procedure as in Fig. 6.6 (use of the IfAC data only). Only inset is displayed, the full range of the recovered IfAC was -200 fs to 200 fs.

Trial phase				Error in Four. domain fit with int. spectrum	Error in Four. domain fit with $\tilde{C}(\omega)$ from IfAC
	A	B	C		
●—	0	1	0	0.23	0.016
●—	0	10	0	0.23	0.005
●—	0	100	0	0.23	6.0
●—	10	1	0	4.0	6.9
●—	10	1	10	4.0	6.9

Table 6.3: Errors of the pulses resulting from the fit calculated in the Fourier domain. Corresponding interferometric autocorrelations are displayed in Fig. 6.13. As the functions which are used for the calculation in the Fourier space are different for the two methods used, the errors calculated cannot be directly compared. For the calculation of the starting phase for the iterative algorithm from variables A, B and C, see Eq. 6.18.

The starting phase is not so crucial, however for optimal results it should not principally differ from the assumed phase. Quadratic starting phase was a good choice in a wide range of parameters of the quadratic function.

6.4 Relation to the experimental errors

The aim of this section is to show how the result of the shape and phase retrieval algorithms is influenced by the experimental inaccuracies. The quality of the measured IfAC is directly related to the acquisition time spent for the measurement of the interferogram. The noise in IfAC is resulting in a background in its Fourier transform. Then the spectral range in which the functions $G(\omega)$ and $\tilde{C}(\omega)$ (which are used as the input for the pulse retrieval algorithm) are above the noise level is getting narrower. However, this noise can be easily suppressed by obtaining the IfAC as an average over increased number of acquisitions. As mentioned already in Section 6.3, the interval in which the $G(\omega)$ remains above the background level is in our case corresponding to $\pm 0.2\,\mathrm{eV}$ for a 40 minutes long measurement. This is enough for the basic pulse description.

As the 2ω peak in the Fourier transform of the IfAC is usually smaller than the 0ω peak, the interval in which the $\tilde{C}(\omega)$ function is above the noise level is narrower than in the case of the $G(\omega)$ function. For the available experimental data, the corresponding energy interval was $\pm 0.13\,\mathrm{eV}$, the phase recovery was, however, reproducible also in this case.

For the algorithm which is using the intensity spectrum as the input for the phase fitting procedure (Fig. 6.5), the necessary accuracy of the spectrum data should be checked. For this test, the correct spectrum (calculated from the electric field with use of Eq. 6.14) was intentionally modified to simulate the possible inaccuracy of the spectrometer. One modified spectrum was obtained by multiplying the correct one by a linear function which was causing a 5% increase of the spectrum magnitude at 1 eV distance from the central energy. Another spectra were modified by 10%/1 eV resp. by 20%/1 eV.

Results of this test are displayed in Fig. 6.14. As the correct pulse shape was used, the phase fitting results were influenced by the spectrum inaccuracy only. The phase of the electric field was obtained for the correct spectrum (as a reference data set) and for the three modified spectra by the procedure indicated in Fig. 6.5. Then the IfACs were calculated from the obtained electric field descriptions. As can be seen from the left panel of Fig. 6.14, the reconstructed IfACs are matching the original one so well that the difference cannot be seen by eye. Therefore, the differences are displayed separately

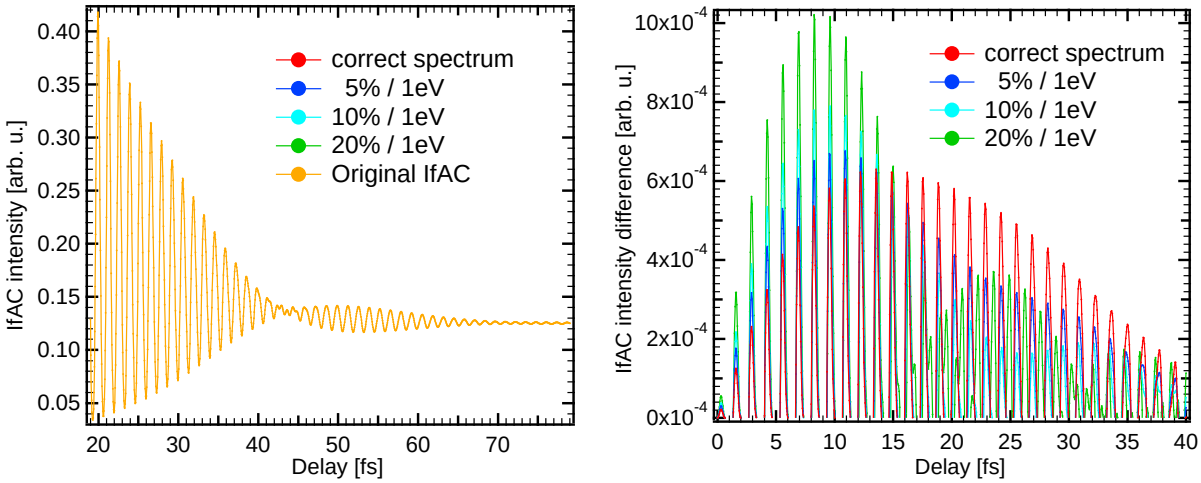

Figure 6.14: Test of necessary accuracy of the intensity spectrum needed for the determination of the phase of electric field. Correct spectrum (red), spectra changed by 5%/1 eV (blue, for further explanation see the text), 10%/1 eV (light blue) and 20%/1 eV were used. Left panel: The IfACs calculated from resulting electric fields, no difference is observable by eye. Right panel: Differences calculated between individual IfACs and the correct IfAC. The IfACs were normalized to 1.

in the right panel. The difference of the 5%/1 eV-curve is at the level of the intrinsic numerical noise defined by the IfAC calculated with the correct spectrum, the difference of the 20%/1 eV-curve is almost twice larger, but still of the 10^{-3} order which is still far enough for good IfAC description.

The tests performed in this section are showing that the accuracy of the spectrum measurements provided by usual laboratory equipment is sufficient for the determination of the phase of the electric field of the femtosecond pulse. However, only linear modifications of the spectrum were tested. The distortions caused by the viewports of the vacuum chamber can be more complex, therefore the replacing of the intensity spectrum in the UHV chamber by the one measured outside of the apparatus is not generally justified. However, the expected differences are very small. The procedure used for the determination of the phase of the electric field in the femtosecond pulse was giving slightly better results when the intensity spectrum of the pulse was used than in the case of the use of the IfAC only. We can therefore conclude that also in the case of spectrum measured outside the chamber the procedure will give reliable results. For particular experimental setup, the best approach would be to conduct both procedures and evaluate the quality of the recovered IfAC and then the method giving better result should be chosen.

6.5 Application of the recovered pulse in the optical Bloch equations

The determination of the amplitude and the phase of the electric field in the femtosecond pulse used in our 2PP experiment is not only necessary for the adjustment of the experimental setup, so that it is producing pulses as short as possible. As mentioned before, the main necessity of a proper laser pulse characterization is in experiments studying the ultrafast electron dynamics. As pointed out already in Section 5.3, the optical Bloch equations are a feasible tool for describing the interaction of optical femtosecond pulses with duration comparable to the phase relaxation time of the excited states [14, 98]. In this section, it will be checked whether the accuracy of the pulse shape and phase retrieval procedures described in the previous sections is sufficient for the determination of the relaxation times in a treatment based on the optical Bloch equations.

The procedure of derivation of the optical Bloch equations for the three-level system was already described in Section 5.3. Of interest are for us the lifetimes of incoherent population decay of the intermediate level T_1^1 and coherent phase decay lifetimes T_2^{01} and T_2^{12} as they are describing the dynamics of the intermediate level which is under investigation. Important is also the coherent phase decay lifetime T_2^{02} as it is influencing the 2PP interferogram shape too. With use of the test pulse displayed in Fig. 6.8 a test 2PP interferogram with parameters $T_1^1 = 25\,\mathrm{fs}$, $T_2^{01} = 12.5\,\mathrm{fs}$, $T_2^{12} = 25\,\mathrm{fs}$ and $T_2^{02} = 25\,\mathrm{fs}$ was calculated.

As in the real experiment, it was tried to recover these relaxation times while the only knowledge available was the pulse shape and the phase obtained by the procedures described in the previous sections. A pulse obtained with use of the Lorentzian starting pulse with width of 10 fs and the asymmetry of 20 was used. For the phase fitting, the staring phase was $A = 0$, $B = 1$ and $C = 0$ (see Eq. 6.18 for explanation) and the procedure using the intensity spectrum was applied.

The nonlinear least-squares procedure was applied to recover the relaxation times. The STARPAC library of the of the National Institute of Standards and Technology [119] was used for this purpose. However, difficulties can be, as usual, expected for fitting of all the four parameters simultaneously. This is because some of the parameters are influencing the 2PP interferogram in a very similar way. Therefore, the procedure was, as a first check, started as a fit of one parameter only, while the other three parameters were fixed at their correct values. However, in the real experiment there will not be the possibility to fix all of the relaxation times to the correct values, because these

are in the most general case unknown. Therefore, the procedure for the 2-, 3- and finally 4-parameters fit was also tested. As the dependence of the 2PP-interferogram on the relaxation times is very complex, also the starting values of the lifetimes will be important. The $T_{1,\,\mathrm{start}}^{1} = 10\,\mathrm{fs}$, $T_{2,\,\mathrm{start}}^{01} = 6\,\mathrm{fs}$, $T_{2,\,\mathrm{start}}^{12} = 10\,\mathrm{fs}$ and $T_{2,\,\mathrm{start}}^{02} = 10\,\mathrm{fs}$ values were used. They are of the correct order, but anyway not very close to the accurate result.

The results of the nonlinear least-squares procedure are displayed in Table 6.4. First, all the parameters were fixed to their correct values and only one of them was numerically fitted. The resulting relaxation times were as follows (differences with respect to the correct values are given in brackets): $T_1^1 = 25.1\,\mathrm{fs}$ (0.5%), $T_2^{01} = 11.9\,\mathrm{fs}$ (5%), $T_2^{12} = 28.6\,\mathrm{fs}$ (14%) and $T_2^{02} = 25.5\,\mathrm{fs}$ (2%). One can say that the correspondence to the correct values is good in the case of fitting just one of the parameters.

The results of the procedure for the 2-, 3- and 4-parameters fit are also displayed in Table 6.4. The 4-free-parameters procedure was giving similarly good results as the one parameter fit for the T_1^1 and T_2^{02} values. The parameters T_2^{01} and T_2^{12} are influencing the

	T_1^1 [fs]	T_2^{01} [fs]	T_2^{12} [fs]	T_2^{02} [fs]
correct values	25	12.5	25	25
1-parameter fit	25.1			
		11.9		
			28.6	
				25.5
2-parameters fit	25.7	11.3		
	23.5		31.3	
	25.1			25.6
		7.3	40.9	
		11.7		26.2
			28.8	24.3
3-parameters fit	24.7	7.5	41.1	
	26.0	10.9		27.0
	23.3		32.4	23.1
		7.2	40.9	26.4
complete fit	25.0	7.2	41.0	26.4

Table 6.4: Recovered values of the relaxation times by least-squares method. Not-fitted parameters were fixed at their correct values.

photoemission signal in a similar way, so that their simultaneous fit was not providing very good results (up to 50% difference from the correct values). This problem has to be solved either by including some additional theoretical considerations for the relations between relaxation times or by improving the fitting algorithm. However, this problem was partly occurring even in situations when the correct pulse shape was supplied to this least-squares procedure.

It can be therefore concluded that the precision of the pulse characterization techniques described in this chapter is sufficient for providing the input for the optical Bloch equations model.

In conclusion, in this chapter, methods for the characterization of the femtosecond pulses in the amplitude and phase of the electric field were developed. The methods which are prospective for application in time-resolved photoemission experiments were stressed and it was justified that these methods are accurate enough for this purpose.

Conclusion

This work was mainly concerned about the problem of the optical excitation of metallic surfaces. The home-built femtosecond pulsed laser system which was setup as the excitation source was offering very high photon flux densities. This was the key to the observation of new physical phenomena.

In the first part of the thesis (Chapter 1), the description of the apparatus for two- and more-photon photoemission was given. This apparatus was setup to perform the study discussed in Chapter 2. It was dealing with the photoemission from the Cu(001) surface. An intense photoemission signal at the energy corresponding to the excitation by three photons was observed. The high exciting photon flux density was allowing to observe photoelectrons even at energies accessible by at least four photons. This excitation process was already in the *above threshold ionization* range. It is one of few observations of the above threshold ionization in the solid material ever. Moreover, the four-photon photoemission energy range with clearly pronounced electronic features was never reached before to our knowledge. The observed spectroscopic features were explained in terms of the electronic structure of the Cu(001) surface.

Another method for studies of the metallic surfaces discussed in the thesis was the Magnetization-Induced Surface Second Harmonic Generation (MSSHG). The theoretical description of obtaining the information about the surface magnetism by means of the Surface Second Harmonic Generation was given in Chapter 3. In Chapter 4, the p(1×1)O/Fe/MgO(001) system was studied, the main result of the work was the justification that the MSSHG method and the Spin Polarized Metastable Deexcitation Spectroscopy are providing compatible information about the surface magnetism. It was the first time that some of the measurements were performed in the p-in/s-out longitudinal geometry which is providing the information about the surface magnetism directly.

A very large potential of optical methods used for the investigations of the surface properties of metals is in the possibility of achieving the time resolution. The complete data treatment has to rely on the exact description of the laser pulse used for the ex-

citation. Theoretical description of the problem was given in Chapter 5. In Chapter 6, the methods for determination of the pulse shape and phase were discussed and further developed. The accuracy of the results was discussed with respect to needs of a time-resolved two-photon photoemission experiment.

Perspectives of further application of the topics developed in this thesis are mainly in the time-resolved two-photon photoemission experiments. It was justified that the performance of the experimental apparatus is allowing to perform experiments in areas not accessible before both in the photoemission and in the second harmonic research field. In the combination with a careful laser pulse characterization, this is a very promising fundament for future time-resolved studies.

List of abbreviations and symbols

Abbreviations and symbols used in the thesis are listed here for convenience.

Abbreviations

1PP	(one-photon) photoemission
2PP	two-photon photoemission
ATI	above-threshold ionization
BBO	β-BaB_2O_4
FROG	Frequency-Resolved Optical Gating
FWHM	full width at half maximum
I2PP	2PP interferometric signal
IAC	intensity autocorrelation
IfAC	interferometric autocorrelation
IP	image potential
MBE	Molecular Beam Epitaxy
ML	monolayer
MEED	Medium-Energy Electron Diffraction
MSSHG	Magnetization-Induced Surface Second Harmonic Generation
OBE	optical Bloch equations
PEEM	Photoemission Electron Microscopy
SHG	Second Harmonic Generation
SPMDS	Spin Polarized Metastable Deexcitation Spectroscopy
STM	scanning tunneling microscope
SR	surface resonance
Ti:S	titanium-sapphire

TIVI	temporal information via intensity
TR-2PP	time-resolved two-photon photoemission
UHV	ultra high vacuum

Symbols and constants

Symbols appearing in the thesis on particular places only are not listed in the table.

$\mathcal{A}$	asymmetry
$\boldsymbol{\chi}$	susceptibility tensor
$\boldsymbol{E}$	electric field intensity vector
$\tilde{\mathcal{E}}$	complex envelope of the electric field intensity
$\mathcal{E}$	real part of $\tilde{\mathcal{E}}$
E_B	binding energy
E_F	Fermi energy (Fermi level)
E_{VAC}	vacuum energy (vacuum level) $E_{\mathrm{VAC}} - E_F = \Phi$
f	frequency
Φ	work function
$\hbar$	Planck's constant, $\hbar = 1.0545587 \cdot 10^{-34}$ Js
I	(optical) intensity
IAC	intensity autocorrelation
IfAC	interferometric autocorrelation
$\boldsymbol{k}$	wavevector
λ	wavelength
m_e	electron mass, $m_e = 9.109534 \cdot 10^{-31}$ kg
m^*	effective mass of an electron
$\boldsymbol{M}$	magnetization vector
$\boldsymbol{p}$	momentum vector
$\boldsymbol{P}$	electric polarization vector
$S(\omega)$	intensity spectrum
T_1^1, T_2^{01}, T_2^{12}, T_2^{02}, T_1^0, T_1^2	relaxation times in the optical Bloch equations formalism
τ	delay (in time-resolved experiments)
ω	(angular) frequency

Bibliography

[1] J. H. Judy, J. Magn. Magn. Mater. 235 (2001) 235.

[2] G. A. Prinz, Science 282 (1998) 1660.

[3] S. A. Wolf, J. Supercond. 13 (2000) 195.

[4] J. A. C. Bland, A. Hirohata, C. M. Guertler, Y. B. Xu, M. Tselepi, J. Appl. Phys. 89 (2001) 6740.

[5] B. C. Choi, M. Belov, W. K. Hiebert, G. E. Ballentine, M. R. Freeman, Phys. Rev. Lett. 86 (2001) 728.

[6] T. Gerrits, H. A. M. van den Berg, J. Hohlfeld, L. Bär, T. Rasing, Nature 418 (2002) 509.

[7] E. Grochowski, Hitachi Global Storage Technologies website, `http://www.hitachigst.com/hdd/technolo/overview/storagetechchart.html`.

[8] H. Petek, S. Ogawa, Prog. Surf. Sci. 56 (1997) 239.

[9] S. Hüfner, Photoelectron Spectroscopy: principles and applications, Springer-Verlag, Berlin Heidelberg, 1995.

[10] T. H. Maiman, Nature 187 (1960) 493.

[11] M. C. Teich, J. M. Schroeer, G. J. Wolga, Phys. Rev. Lett. 13 (1964) 611.

[12] V. Dose, Surf. Sci. Rep. 5 (1985) 337.

[13] N. V. Smith, Rep. Prog. Phys. 51 (1988) 1227.

[14] J.-C. Diels, W. Rudolph, Ultrashort Laser Pulse Phenomena, Academic Press, San Diego, 1996.

[15] A. E. Siegman, Lasers, University Science Books, Sausalito, 1986.

[16] L. Xu, G. Tempea, A. Poppe, M. Lenzner, C. Spielmann, F. Krausz, A. Stingl, K. Ferencz, Appl. Phys. B 65 (1997) 151.

[17] P. F. Moulton, J. Opt. Soc. Am. B 3 (1986) 125.

[18] D. E. Spence, P. N. Kean, W. Sibbett, Opt. Lett. 16 (1991) 42.

[19] R. Szipőcs, A. Kőházi-Kis, Appl. Phys. B 65 (1997) 115.

[20] J. Kirschner, H. Engelhard, D. Hartung, Rev. Sci. Instrum. 73 (2002) 3853.

[21] I. Tamm, Z. Physik 76 (1932) 849.

[22] W. Shockley, Phys. Rev. 56 (1939) 317.

[23] P. M. Echenique, J. B. Pendry, J. Phys. C 11 (1978) 2065.

[24] J. B. Pendry, S. J. Gurman, Surf. Sci. 49 (1975) 87.

[25] M. Weinert, S. L. Hulbert, P. D. Johnson, Phys. Rev. Lett. 55 (1985) 2055.

[26] N. V. Smith, Phys. Rev. B 32 (1985) 3549.

[27] G. Grosso, G. P. Parravicini, Solid State Physics, Academic Press, San Diego, 2000.

[28] P. D. Johnson, N. V. Smith, Phys. Rev. B 27 (1983) 2527.

[29] V. Dose, W. Altmann, A. Goldmann, U. Kolac, J. Rogozik, Phys. Rev. Lett. 52 (1984) 1919.

[30] K. Giesen, F. Hage, F. J. Himpsel, H. J. Riess, W. Steinmann, Phys. Rev. Lett. 55 (1985) 300.

[31] K. Giesen, F. Hage, F. J. Himpsel, H. J. Riess, W. Steinmann, Phys. Rev. B 33 (1986) 5241.

[32] S. Ogawa, H. Petek, Surf. Sci. 363 (1996) 313.

[33] H. Petek, H. Nagano, M. J. Weida, S. Ogawa, J. Phys. Chem. B 105 (2001) 6767.

[34] H. Petek, S. Ogawa, Annu. Rev. Phys. Chem. 53 (2002) 507.

[35] H. Petek, H. Nagano, S. Ogawa, Appl. Phys. B 68 (1999) 369.

[36] H. Petek, H. Nagano, M. J. Weida, S. Ogawa, Chem. Phys. 251 (2000) 71.

[37] H. Petek, H. Nagano, S. Ogawa, Phys. Rev. Lett. 83 (1999) 832.

[38] U. Höfer, I. L. Shumay, C. Reuß, U. Thomann, W. Wallauer, T. Fauster, Science 277 (1997) 1480.

[39] R. Knorren, K. H. Bennemann, R. Burgemeister, M. Aeschlimann, Phys. Rev. B 61 (2000) 9427.

[40] C. A. Schmuttenmaer, M. Aeschlimann, H. E. Elsayed-Ali, R. J. D. Miller, D. A. Mantell, J. Cao, Y. Gao, Phys. Rev. B 50 (1994) 8957.

[41] M. Aeschlimann, M. Bauer, S. Pawlik, Chem. Phys. 205 (1996) 127.

[42] M. Aeschlimann, M. Bauer, S. Pawlik, R. Knorren, G. Bouzerar, K. H. Bennemann, Appl. Phys. A. 71 (2000) 485.

[43] M. Aeschlimann, R. Burgemeister, S. Pawlik, M. Bauer, D. Oberli, W. Weber, J. Elect. Spectrosc. Relat. Phenom. 88-91 (1998) 179.

[44] G. H. Fecher, O. Schmidt, Y. Hwu, G. Schönhense, J. Elect. Spectrosc. Relat. Phenom. 126 (2002) 77.

[45] M. Cinchetti, A. Oelsner, G. H. Fecher, H. J. Elmers, G. Schönhense, Appl. Phys. Lett. 83 (2003) 1503.

[46] G. A. Burdick, Phys. Rev. 129 (1963) 138.

[47] J. Hermanson, Sol. State Comm. 22 (1977) 9.

[48] A. Goldmann, V. Dose, G. Borstel, Phys. Rev. B 32 (1985) 1971.

[49] K. Giesen, F. Hage, F. J. Himpsel, H. J. Riess, W. Steinmann, Phys. Rev. B 35 (1987) 971.

[50] S. L. Hulbert, P. D. Johnson, M. Weinert, R. F. Garrett, Phys. Rev. B 33 (1986) 760.

[51] D. Straub, F. J. Himpsel, Phys. Rev. Lett. 52 (1984) 1922.

[52] F. J. Himpsel, J. E. Ortega, Phys. Rev. B 46 (1992) 9719.

[53] P. Hofmann, R. Unwin, W. Wyrobisch, A. M. Bradshaw, Surf. Sci. 72 (1978) 635.

[54] D. P. Woodruff, S. L. Hulbert, P. D. Johnson, N. V. Smith, Phys. Rev. B 31 (1985) 4046.

[55] V. Dose, Surf. Sci. Rep. 5 (1985) 337.

[56] P. Agostini, F. Fabre, G. Mainfray, G. Petite, N. K. Rahman, Phys. Rev. Lett. 42 (1979) 1127.

[57] M. J. DeWitt, R. J. Levis, Phys. Rev. Lett. 81 (1998) 5101.

[58] S. Luan, R. Hippler, H. Schwier, H. O. Lutz, Europhys. Lett. 9 (1989) 489.

[59] W. S. Fann, R. Storz, J. Bokor, Phys. Rev. B 44 (1991) R10980.

[60] M. Aeschlimann, C. A. Schmuttenmaer, H. E. Elsayed-Ali, R. D. J. Miller, J. Cao, Y. Gao, D. A. Mantell, J. Chem. Phys. 102 (1995) 8606.

[61] F. Banfi, C. Giannetti, G. Ferrini, G. Galimberti, S. Pagliara, D. Fausti, F. Parmigiani, Phys. Rev. Lett. 94 (2005) 037601.

[62] P. A. Franken, A. E. Hill, C. W. Peters, G. Weinreich, Phys. Rev. Lett. 7 (1961) 118.

[63] N. Bloembergen, P. S. Pershan, Phys. Rev. 128 (1962) 606.

[64] R.-P. Pan, H. D. Wei, Y. R. Shen, Phys. Rev. B 39 (1989) 1229.

[65] W. Hübner, K.-H. Bennemann, Phys. Rev. B 40 (1989) 5973.

[66] J. Reif, J. C. Zink, C.-M. Schneider, J. Kirschner, Phys. Rev. Lett. 67 (1991) 2878.

[67] P. N. Argyres, Phys. Rev. 97 (1955) 334.

[68] T. Rasing, J. Magn. Magn. Mater. 175 (1997) 35.

[69] W. Hübner, in: Nonlinear Optics in Metals, ed. K. H. Bennemann, Clarendon Press, Oxford, 1998, p. 301.

[70] C. K. Chen, T. F. Heinz, D. Ricard, Y. R. Shen, Phys. Rev. Lett. 46 (1981) 1010.

[71] Y. R. Shen, J. Vac. Sci. Technol. B 3 (1985) 1464.

[72] J. M. Van Hove, C. S. Lent, P. R. Pukite, P. I. Cohen, J. Vac. Sci. Technol. B 1 (1983) 741.

[73] D. Stoeffler, F. Gautier, J. Magn. Magn. Mater. 147 (1995) 260.

[74] C. M. Fang, R. A. de Groot, M. M. J. Bischoff, H. van Kempen, Surf. Sci. 445 (2000) 123.

[75] B. Nonas, K. Wildberger, R. Zeller, P. H. Dederichs, J. Magn. Magn. Mater. 165 (1997) 137.

[76] Q. Y. Jin, H. Regensburger, R. Vollmer, J. Kirschner, Phys. Rev. Lett. 80 (1998) 4056.

[77] Q. Y. Jin, R. Vollmer, H. Regensburger, J. Kirschner, J. Appl. Phys. 85 (1999) 5288.

[78] F. Bisio, R. Moroni, M. Canepa, L. Mattera, R. Bertacco, F. Ciccacci, Phys. Rev. Lett. 83 (1999) 4868.

[79] S. R. Chubb, W. E. Pickett, Phys. Rev. Lett. 58 (1987) 1248.

[80] P. Bonanno, M. Canepa, P. Cantini, R. Moroni, L. Mattera, S. Terreni, Surf. Sci. 454–456 (2000) 697.

[81] T. Urano, T. Kanaji, J. Phys. Soc. Jpn. 57 (1988) 3403.

[82] C. Li, A. J. Freeman, Phys. Rev. B 43 (1991) 780.

[83] S. R. Chubb, W. E. Pickett, Solid State Commun. 62 (1987) 19.

[84] O. V. Lysenko, V. S. Stepanyuk, W. Hergert, J. Kirschner, Phys. Rev. Lett. 89 (2002) 126102.

[85] P. Drude, Ann. Phys. 1 (1900) 566.

[86] P. B. Johnson, R. W. Christy, Phys. Rev. B 6 (1972) 4370.

[87] P. B. Johnson, R. W. Christy, Phys. Rev. B 11 (1975) 1315.

[88] J. B. Smith, H. Ehrenreich, Phys. Rev. B 25 (1982) 923.

[89] V. A. Gasparov, R. Huguenin, Adv. Phys. 42 (1993) 393.

[90] J. Bass, W. P. Pratt, Jr., P. A. Schroeder, Rev. Mod. Phys. 62 (1990) 645.

[91] C. J. Powell, Surf. Sci. 44 (1974) 29.

[92] S. M. Sze, C. R. Crowell, G. P. Carey, E. E. LaBate, J. Appl. Phys. 37 (1966) 2690.

[93] H. Kanter, Phys. Rev. B 1 (1970) 522.

[94] A. Goldmann, R. Matzdorf, F. Theilmann, Surf. Sci. 414 (1998) L932.

[95] W. Wurth, Appl. Phys. A 65 (1997) 597.

[96] C. Keller, M. Stichler, G. Comelli, F. Esch, S. Lizzit, D. Menzel, W. Wurth, Phys. Rev. B 57 (1998) 11951.

[97] L. Bürgi, O. Jeandupeux, H. Brune, K. Kern, Phys. Rev. Lett. 82 (1999) 4516.

[98] R. Loudon, The Quantum Theory of Light, 2nd Edition, Clarendon Press, Oxford, 1983.

[99] S. Ogawa, J. Elect. Spectrosc. Relat. Phenom. 124 (2002) 245.

[100] M. J. Weida, S. Ogawa, H. Nagano, H. Petek, J. Opt. Soc. Am. B 17 (2000) 1443.

[101] R. Trebino, K. W. DeLong, D. N. Fittinghoff, J. N. Sweetser, M. A. Krumbügel, B. A. Richman, D. J. Kane, Rev. Sci. Instrum. 68 (1997) 3277.

[102] J. Paye, M. Ramaswamy, J. G. Fujimoto, E. P. Ippen, Opt. Lett. 18 (1993) 1946.

[103] K. W. DeLong, D. N. Fittinghoff, R. Trebino, B. Kohler, K. Wilson, Opt. Lett. 19 (1994) 2152.

[104] D. J. Kane, IEEE J. Quantum Elect. 35 (1999) 421.

[105] J. W. Nicholson, F. G. Omenetto, D. J. Funk, A. J. Taylor, Opt. Lett. 24 (1999) 490.

[106] I. Amat-Roldán, I. G. Cormack, P. Loza-Alvarez, E. J. Gualda, D. Artigas, Opt. Express 12 (2004) 1169.

[107] J.-C. Diels, J. J. Fontaine, I. C. McMichael, F. Simoni, Appl. Opt. 24 (1985) 1270.

[108] K. Naganuma, K. Mogi, H. Yamada, IEEE J. Quantum Electron. 25 (1989) 1225.

[109] J. Peatross, A. Rundquist, J. Opt. Soc. Am. B 15 (1998) 216.

[110] M. J. Weida, T. Tomaru, S. Ogawa, H. Nagano, H. Petek, A simple model for in situ characterization of femtosecond pulses using surface second-harmonic generation, unpublished.

[111] J. R. Fienup, Appl. Opt. 21 (1982) 2758.

[112] M. Frigo, S. G. Johnson, FFTW: An adaptive software architecture for the FFT, in: Proc. 1998 IEEE Intl. Conf. Acoustics Speech and Signal Processing, Vol. 3, IEEE, 1998, pp. 1381–1384.

[113] R. W. Gerchberg, W. O. Saxton, Optik 35 (1972) 237.

[114] A. M. J. Huiser, A. J. J. Drenth, H. A. Ferwerda, Optik 45 (1976) 303.

[115] I. P. Christov, M. M. Murnane, H. C. Kapteyn, J. Zhou, C.-P. Huang, Opt. Lett. 19 (1994) 1465.

[116] J. W. Nicholson, J. Jasapara, W. Rudolph, F. G. Omenetto, A. J. Taylor, Opt. Lett. 24 (1999) 1774.

[117] A. Baltuška, Z. Wei, M. S. Pshenichnikov, D. A. Wiersma, R. Szipőcs, Appl. Phys. B 65 (1997) 175.

[118] L. Gallmann, D. H. Sutter, N. Matuschek, U. Keller, Appl. Phys. B 70 (2000) S67.

[119] J. R. Donaldson, P. V. Tryon, User's guide to STARPAC — The standards, time series, and regression package: National Institute of Standards and Technology Internal Report NBSIR 86-3448.

List of publications

Original refereed papers

T. Kawagoe, Y. Suzuki, M. Nývlt, J. Franta and N. Hosoito, *Magnetic domain structure and exchange coupling in epitaxial Fe/FeRh(001) and NiFe/FeRh(001) bilayers*, Surface Science 493 (1.11.2001), 721. (related to Chapter 3)

M. Nývlt, F. Bisio, J. Franta, C.L. Gao, H. Petek and J. Kirschner, *Surface Magnetism During Oxygen-Aided Fe Homoepitaxy*, Phys. Rev. Lett. 95 (14.9.2005) 127201 (related to Chapters 3 and 4)

F. Bisio, M. Nývlt, J. Franta, H. Petek and J. Kirschner, *Mechanisms of high-order perturbative photoemission from metals*, submitted to Phys. Rev. Lett. (related to Chapters 1 and 2)

Conference presentations

J. Franta, M. Nývlt, Y. Suyuki, T. Katayama, *Effect of noble metal spacer on AF-FM exchange coupling in NiFe/FeRh-Ir(001) system*, Nanomag meeting Biarritz 25.10.2001, poster, presenting author. (related to Chapter 3)

M. Nývlt, Y. Suzuki, J. Franta, T. Katayama, *An origin of coercivity enhancement due to exchange coupling between ferromagnet and antiferromagnet in NiFe/FeRh-Ir epitaxial bilayers*, ICMFS 2002 Kyoto 5.3.2002, poster, co-author. (related to Chapter 3)

M. Nývlt, F. Bisio, J. Franta and J. Kirschner, *Periodic oscillations of magnetization-induced optical Second Harmonic Generation during Fe-growth on Fe(1×1)O/Fe(001)*, ICMFS 2003 Madrid, 22.7.-25.7.2003 poster, presenting author. (related to Chapters 3 and 4)

M. Nývlt, F. Bisio, J. Franta and J. Kirschner, *Second Harmonic Generation study of oxygen-aided Fe homoepitaxy*, INFM meeting 2003 , Italy 22.7.-25.7.2003 poster, co-

author. (related to Chapters 3 and 4)

J. Franta, M. Nývlt, F. Bisio, H. Petek and J. Kirschner, *Multiphoton photoemission spectroscopy of Cu(001) surfaces*, ECOSS 2003 Praha, 7.9.-12.9.2003 oral presentation, presenting author. (related to Chapters 1 and 2)

M. Nývlt, F. Bisio, J. Franta and J. Kirschner, *Optical second harmonic generation from ferromagnetic and anti-ferromagnetic surfaces (invited)*, ECOSS 2003 Praha, 7.9.-12.9.2003 invited lecture, co-author. (related to Chapters 3, 4, 5 and 6)

Other presentations

J. Franta, *Kerr vectorial magnetometry and Kerr spectroscopy of thin metal films*, Internal seminar of MPI-Halle, Ringberg 1.5.2002.

J. Franta, *Multiphoton photoemission spectroscopy of Cu(001) surfaces*, Internal seminar of MPI-Halle, 28.11.2003. (related to Chapters 1 and 2)